Cold and controlled ion–radical reactions, relevant to the interstellar medium and outer atmosphere



Chloé Miossec
Linacre College
University of Oxford

A thesis submitted for the degree of
Doctor of Philosophy
May 2023

Abstract

This thesis reports the design, construction, and characterisation of a cryogenic linear Paul ion trap chamber. This cryogenic ion trap chamber will be combined with a magnetic guide as a source of radicals, also described in this thesis, for the study of ion–radical reactions under cold and controlled conditions. Ion–radical reactions are important for the chemistry happening in the interstellar medium and in certain regions of Earth's atmosphere, where both temperature and pressure are low. Despite their importance, there are very few existing methods for studying reactions between ions and radicals at low temperatures.

The new cryogenic linear Paul trap introduced in this thesis is the first such device to incorporate an in-built time-of-flight mass-spectrometer. The design of the apparatus minimizes the temperature at the ion trap region, down to 10 K, and ensures that vibrations induced by the cryogenic system do not adversely affect the resolution of the Coulomb crystal images. The constraints of optical access to the trap center for lasers and imaging of Coulomb crystals have been overcome by the implementation of a new optical system based on off-axis parabolic mirrors. We have successfully trapped and imaged Ca^+ Coulomb crystals, and work is in preparation to form molecular ions.

Alongside the work on the cryogenic ion trap, the thesis also demonstrates how a magnetic guide can act as a stand-alone source of state- and velocity-selected radical species. In this way, a beam of state- and velocity-selected radicals can be filtered from an incoming beam containing a mixture of different species. The magnetic guide therefore provides a source of cold and controlled neutral reactants. Work is underway to combine the two set-ups, facilitating the study of ion–radical reactions.

The cryogenic ion trap apparatus presented here is a truly unique apparatus. It will enable us to study reactions involving a range of state-selected molecular ions, which, through reactions with velocity- and state-selected radicals from the magnetic guide, can lead to new knowledge on fundamental reaction dynamics and kinetics.

Declaration

Parts of Chapter 1, Chapter 3, Chapter 4, 5 and Chapter 7 have been published in the following papers.

Chloé Miossec, Lok Yiu Wu, Paul Bertier, Michal Hejduk, Jutta Toscano, Brianna R. Heazlewood. A stand-alone magnetic guide for producing tuneable radical beams. Journal of Chemical Physics, 153 (10): 104202, 2020.

Chloé Miossec, Michal Hejduk, Rahul Pandey, Neville J. A. Coughlan, and Brianna R. Heazlewood. Design and characterization of a cryogenic linear Paul ion trap for ion–neutral reaction studies. Review of Scientific Instruments, 93 (3): 033201, 2022.

Lok Yiu Wu, Chloé Miossec, Brianna R. Heazlewood. Low-temperature reaction dynamics of paramagnetic species in the gas phase. Chemical Communications, 58(20): 3240, 2022.

Acknowledgements

I would like to thank every person that has contributed to the work presented in this thesis, and everyone that has helped and supported me through my DPhil years. To Brianna Heazlewood, for being the most supportive, caring, optimistic, and patient supervisor a DPhil student could dream of, and for teaching me so much.
To Andriana Tsikritea, for teaching me not only everything there is to know about the lab and the experiments but also for helping me craft my skill of argumentation during our lunch breaks.
To Kathy Wu, for helping me so much in the lab and filling my days with ducklings and enthusiasm.
To Michal Hejduk, for entrusting me with the cryogenic ion trap, and for his humour. To Jake Diprose, for his toaster. To all current and previous member of the Heazlewood group, Rahul, Maks, Vincent, Paul, for making everyday fun and enjoyable. To the facilities teams of both the PTCL at the University of Oxford and the Oliver Lodge at the University of Liverpool. To the mechanical and electrical workshops, for their cheerful assistance throughout the years with our broken equipment.
To my friends, both in Liverpool and in Oxford, for our mutual support in hardship. To my rugby friends from Liverpool, for putting up with me and dealing with my grumpiness or over-enthusiasm.

Je voudrais aussi remercier mes meilleurs amis pour leur soutien depuis 15 ans, Maxime Maheo, Charlotte Parnaut, Marie Carrat, Bastien Dubourg, Adrien Norindr, Hugo Volpi. À Claire Almyre, je veux adresser mon soutien et mes excuses pour l'avoir poussé dans la voie du doctorat. Merci à Jean Deviers, pour ses encouragements tout au long de nos doctorats, dans les bons comme dans les mauvais moments.
Je voudrais remercier mes parents, Yves Miossec et Annick Miossec, pour leur enthousiasme permanent dans tout ce que j'ai fait, pour leur motivation et pour leur soutien incondionel. J'ai énormement d'admiration pour eux et de fierté d'être leur fille. Je voudrais enfin remercier ma soeur et mon frère, Margot et Victor Miossec, d'être des personnes extraordinaires, et de leur soutien sans faille.

Contents

List of Figures **vi**

List of Tables **x**

1 Introduction **1**
1.1 Cold chemistry . . . 1
1.2 Ion–radical reactions . . . 7
1.2.1 Producing a radical beam . . . 7
1.2.2 Producing a source of molecular ions . . . 20
1.3 Aims . . . 31

2 Background **33**
2.1 Ion trapping . . . 33
2.1.1 Linear Paul ion traps . . . 36
2.2 Laser cooling . . . 43
2.3 Coulomb crystals . . . 46
2.3.1 Sympathetic cooling . . . 47
2.4 Reactions studied using Coulomb crystals . . . 48

3 Design of the cryogenic ion trap apparatus **53**
3.1 Design of the cryogenic Paul trap experiment (CryPTEx) apparatus . 53
3.2 Design . . . 56
3.2.1 Requirements of the apparatus . . . 56
3.2.2 Ion trap . . . 58
3.2.3 Cryogenic system . . . 60
3.2.4 Heim column . . . 65
3.2.5 Time-of-flight mass spectrometer . . . 65
3.2.6 Calcium oven . . . 67

4 Parabolic mirror-based optical system **72**
4.1 Requirements for the optical system . . . 72
4.2 Description of the system . . . 74
4.2.1 Off-axis parabolic (OAP) mirrors . . . 74
4.2.2 Design of our optical system . . . 75
4.3 Characterisation studies . . . 79

4.3.1 Tests outside of the chamber . . . 79
4.3.2 Inside the chamber, comparison at room temperature and cryogenic temperatures . . . 83

5 Experimental characterisation of the cryogenic ion trap 87
5.1 Anti-vibration system . . . 87
5.1.1 Description . . . 88
5.1.2 Characterisation measurements . . . 90
5.2 Temperature measurements . . . 95
5.2.1 Recording the temperature at different locations in the apparatus . . . 95
5.2.2 Results . . . 96
5.3 Time-of-flight Mass Spectrometer detection capability . . . 97
5.3.1 Time-of-flight traces . . . 98
5.3.2 Time-of-flight (ToF) signal of Coulomb crystals . . . 101

6 Fluorescence and Coulomb crystals 102
6.1 Parameters to set . . . 102
6.2 Obtaining fluorescing clouds . . . 104
6.3 Obtaining Coulomb crystals . . . 105

7 Magnetic guide to produce a velocity- and state-selected radical beam 113
7.1 Operating principle of the magnetic guide . . . 114
7.2 Description of the magnetic guide . . . 116
7.3 Successful magnetic filtering of the beam . . . 123
7.4 Limits of magnetic guide and perspective . . . 130

8 Conclusion and future work 132

Bibliography 139

List of Figures

1.1 Arrhenius plot of different reaction mechanisms 4
1.2 Zeeman splitting of OH 8
1.3 Schematic illustration of the Zeeman decelerator apparatus in the Liverpool laboratory 10
1.4 Evolution of the velocity of a decelerated packet of H atoms over time, as the radicals travel through the 12 coils of the Zeeman decelerator . . . 12
1.5 ToF traces obtained by applying different pulse sequences to the Zeeman decelerator 14
1.6 Schematic illustration of a travelling-wave Zeeman decelerator set-up . . 15
1.7 Schematic of the ion-atom hybrid trap at the University of Basel 18
1.8 Schematic illustration of a Laval nozzle used in CRESU set-ups 19
1.9 Comparison of the BBR spectrum at a range of temperatures with the simulated excitation spectrum of one of the vibrational modes in $C_2H_2^+$ at 300 K 23
1.10 Evolution as a function of time of the population of $C_2H_2^+$ ions in the rovibrational ground state, at different temperatures 24
1.11 Schematic illustration of a five-wire surface-electrode ion trap 27
1.12 Measured distribution of rotational states of MgH^+ ions within Coulomb crystals of different numbers of Mg^+ and MgH^+ ions, along with images of the corresponding Coulomb crystals 30

2.1 First design of a Paul ion trap 34
2.2 Conventional linear Paul trap design with a quadrupole configuration of rods 36
2.3 Schematic illustration of the linear quadrupole ion trap of the cryogenic ion trap set-up at the University of Liverpool 38
2.4 Stability diagram of Ca^+ ions in our cryogenic linear Paul trap as a function of a and q 41

2.5 Stability diagram as a function of V_{RF} and U_{end} in the cryogenic ion trap 43
2.6 Energy levels of Ca^+ and transitions relevant for the laser cooling scheme 45
2.7 Images of Coulomb crystals taken with a CCD camera at selected times during a reaction from Petralia et al. study of $Xe^+ + NH_3$ 48
2.8 Comparison between charge transfer rate coefficients for $Xe^+ + NH_3$ and $Xe^+ + ND_3$ reactions obtained experimentally and by capture model theory from Petralia et al. study of $Xe^+ + NH_3$ 49
2.9 Reaction progress data and fits for the pseudo-first order reaction of $CCl^+ + CH_3CN$ 51

3.1 Figure of the original CryPTEx 55
3.2 Figure of the CryPTEx-PTB 56
3.3 Figure of the CryPTEx-SC 57
3.4 Schematic illustrations of the cryogenic ion trap and its shielding case, from two viewpoints 60
3.5 Schematic illustration of the cryogenic ion trap chamber and imaging system 62
3.6 Schematic of the two stage cold shield from the cryocooler cold head to the ion trap 63
3.7 Cut views of the Heim column 66
3.8 Cut views of the innermost temperature stages of the chamber 68
3.9 Drawing of the calcium oven and its holding system 70
3.10 Computer-aided drawing (CAD) of the calcium oven in the cryogenic ion trap chamber. 71

4.1 Schematic of a pair of off-axis parabolic (OAP) mirrors used for 1:1 imaging 75
4.2 Top view of the optical setup 76
4.3 Simulation of the thermal deformations of an OAP mirror at 4 K with different techniques of fixing the OAP mirror to its base unit 78
4.4 Drawing of the breadboard on which the optical system is placed 80
4.5 Images of a resolution test target back-lit with a UV-LED, acquired outside of the chamber, with and without the OAP mirror relay system . 81
4.6 Binarized images of a Ronchi ruling back-lit by a UV-LED, acquired outside of the chamber, after the OAP mirror relay 82

4.7 Images of the Ronchi ruling taken at room and cryogenic temperatures, to look at the effects of shifting one OAP mirror with respect to the other 84

4.8 Comparison of Ronchi ruling images at both room and cryogenic temperatures 86

5.1 Cut view of the cryogenic ion trap to show the dual-frame system 89

5.2 Comparison of the frequencies of vibrations recorded on the ion trap, recorded both with and without the cryocooler on 91

5.3 Comparison of the frequencies of vibrations recorded when the cryocooler is off, with the vacuum pumps on and off 93

5.4 Comparison of vibrations recorded both with and without the cryocooler on 94

5.5 Temperatures recorded at the first outer radiation shield and second inner radiation shield stages, as a function of time 97

5.6 Schematic illustration of the time-of-flight mass spectrometer setup . . . 98

5.7 Experimental time-of-flight trace obtained from continuously applying a voltage to the repeller-extractor pair 99

5.8 Experimental time-of-flight trace of Ca^+ ions formed in the ion trap, then ejected to the ToF-MS 100

6.1 Illustration of the different segments of the ion trap, with the six ways that the voltage applied to the various segments can be altered 103

6.2 Images of the Coulomb crystals obtained in our cryogenic ion trap with the electron multiplying charge-coupled device (EM-CCD) camera, that show different stages of the crystallisation process 105

6.3 Image taken by the electron multiplying charge-coupled device (EM-CCD) camera of the first fluorescence of a (non-optimized) Ca^+ Coulomb crystal 106

6.4 Images of the Coulomb crystals obtained in our cryogenic ion trap with the electron multiplying charge-coupled device (EM-CCD) camera, using two different lenses 107

6.5 Images of Coulomb crystals of different sizes obtained in our cryogenic ion trap with the electron multiplying charge-coupled device (EM-CCD) camera 109

6.6 Images of the Coulomb crystals obtained in our cryogenic ion trap with the electron multiplying charge-coupled device (EM-CCD) camera, for different values of V_{RF} . . . 110

6.7 Image of a Coulomb crystal obtained in our cryogenic ion trap with the ToF trace of the ejected Coulomb crystal . . . 111

6.8 Simulation in SIMION of the trajectory of a packet of ions, ejected from the center of the ion trap towards the MCP detector . . . 112

7.1 ToF traces of H atoms detected with and without the magnetic guide in plcae . . . 115

7.2 Schematic illustration of one Halbach array and a map of its magnetic field magnitude . . . 117

7.3 Side views of different relative positions of only one Halbach array . . . 118

7.4 Schematic illustration of the magnetic guide . . . 119

7.5 Zeeman splitting for $1^2\mathrm{S}_{1/2}$ hydrogen atoms . . . 120

7.6 Schematic illustrations of the combined Zeeman decelerator and magnetic guide . . . 122

7.7 Three-dimensional particle trajectory simulations of a beam of state-selected H atoms travelling through the magnetic guide . . . 124

7.8 Experimental and simulated ToF traces for the H atoms that successfully reach the detection region . . . 126

7.9 Experimental and simulated ToF traces for the H atoms that successfully reach the detection region . . . 127

7.10 Simulated distribution of the H atom beam at the detection region, plotted along the vertical axis with and without the magnetic guide in place 129

8.1 Schematic illustration of the second generation magnetic guide being tested in our laboratory . . . 134

List of Tables

2.1 Operating parameters and dimensions of the cryogenic linear Paul trap described in this work 37

7.1 The relative amounts of target, slower and faster H atoms that reach the detection region with and without the magnetic guide in place 128

Acronyms

$2r_0$ diagonal electrode surface separation

$2V_{\mathbf{RF}}$ RF voltage peak-to-peak

$2z_0$ endcap separation

η geometric factor

$\Omega_{\mathbf{RF}}$ RF frequency

$AB-22PT$ Atomic Beam 22-pole ion trap

R electrode radius

$U_{\mathbf{end}}$ endcap voltage

ADO average dipole orientation

BBR blackbody radiation

CAD Computer-aided drawing

CRESU Cinétique de Réaction en Ecoulement Supersonique Uniforme [reaction kinetics in uniform supersonic flow]

CryPTEx cryogenic Paul trap experiment

EM-CCD electron multiplying charge-coupled device

HFS high-field seeking

ISM interstellar medium

KIDA kinetic database for astrochemistry

LFS low-field seeking

MCPs microchannel plates

MOT magneto-optical trap

NA numerical aperture

OAP off-axis parabolic

OFHC oxygen-free high-conductivity

REMPD resonance-enhanced multiphoton dissociation

REMPI resonance-enhanced multiphoton ionisation

RF radiofrequency

ToF time-of-flight

ToF-MS time-of-flight mass spectrometer

UDfA UMIST database for astrochemistry

UHV ultra high vacuum

UV-LED ultraviolet light emitting diode

Chapter 1

Introduction

Parts of this chapter are based on work that has previously been published in a *Chemistry communications* article: Wu et al. (2020) [1].

1.1 Cold chemistry

At room temperature, the kinetics (rate coefficients) and dynamics (reaction mechanisms, product branching ratios, product state distributions) of a reaction are typically considered based on the average behaviour of the reactants. Multiple internal (rotational and vibrational) quantum states of the reactants are populated, as set out by the Boltzmann distribution. This averaging over many different energy states makes interpreting the individual contributions of different parameters—such as the role of selected quantum states or the collision energy—very difficult to ascertain. At low temperatures, only low-lying internal energy levels are accessible, giving rise to more individual contributions and, at the very lowest temperatures, typically under 10 K, only a single quantum state might be populated.

As very low temperatures are reached, quantum effects start to come to the fore. This shift from a classical regime to a quantum regime makes it possible to witness quantum effects including tunneling and resonances that can subsequently be

studied, that would otherwise be hidden [2, 3]. Resonance states are typically not fully-bound states, but rather correspond to quasi-bound states of the collision complex. Different types of resonances can be present in a given system, depending on the precise location of the resonance [1]. For example, recent work has examined non-Arrhenius behaviour observed at low temperature in the $OH + HCl \rightarrow H_2O + Cl$ reaction. The OH + HCl reaction rate coefficients were found to be independent of temperatures below 250 K. This preservation of reactivity at low temperatures has been attributed to the tunnelling of a H atom through the reaction barrier, enhanced by the presence of multiple Feshbach resonances arising from excited vibrational states trapped in the potential well in the entrance channel due to hydrogen bond interactions [4].

From the Arrhenius equation, $k = Ae^{-E_a/RT}$ (where k is the rate coefficient, A is the pre-exponential factor, E_a is the activation energy, R is the gas constant and T is the temperature) [5], it can be seen that, in the case of exothermic reactions, the rate coefficient of a reaction typically depends on the ability of reactants to overcome an activation barrier. It therefore follows that, based on the Arrhenius equation, we would expect bimolecular reactions to exhibit lower rate coefficients (and, at some point, becoming negligible ~~to stop altogether~~) at low temperatures. It has been shown, however, that some reactions display the opposite behaviour, and have increased reactivity at low temperatures. Figure 1.1 illustrates various types of reactions and their temperature-dependent reaction rate coefficients. In the case of a reaction with a significant energy barrier, as shown in a), it predominantly follows Arrhenius behaviour. At lower temperatures, however, a slight curvature is visible,

that can arise from quantum mechanical tunnelling allowing the system to cross to products, as well as the pre-exponential factor A that has a slight temperature dependence. The panel b) shows a reaction displaying a non-Arrhenius behaviour by exhibiting higher reaction rate coefficients at lower temperatures, characteristic of a barrierless reaction, such as a radical-radical reaction [6]. Finally, the panel c) showcases a reaction passing through a weakly bound complex before crossing a energy barrier to products, radical-polar molecule reactions. One reaction that displays this behaviour is the one between methanol and the hydroxyl radical, where the reaction rate coefficient decreases with decreasing temperature in what looks like Arrhenius behaviour above 200 K; however, simulations and experimental evidence by Shannon et al. [7] revealed that after passing through a minimum, the reaction rate coefficient increases again at temperatures below 200 K. Another reaction that shows a different type of non-Arrhenius behaviour is the reaction between fluorine and para-hydrogen, which displays a lowering of the reaction rate coefficient at lower temperatures until around 20 K, where the reaction rate seems to plateau, and even slightly increase. By changing collision energies between the reactants, it was possible to observe resonance effects, not observed at higher temperatures [8].

It is these classes of reactions displaying non-Arrhenius behaviour, often involving radicals and ions and typically featuring barrierless (or low-barrier) reaction pathways, that offer interesting insights into the chemistry occurring in naturally cold environments. As other competing processes cease, these non-Arrhenius reaction systems show increasing rates and dominate the gas-phase chemistry that takes place in, for example, astrochemical environments.

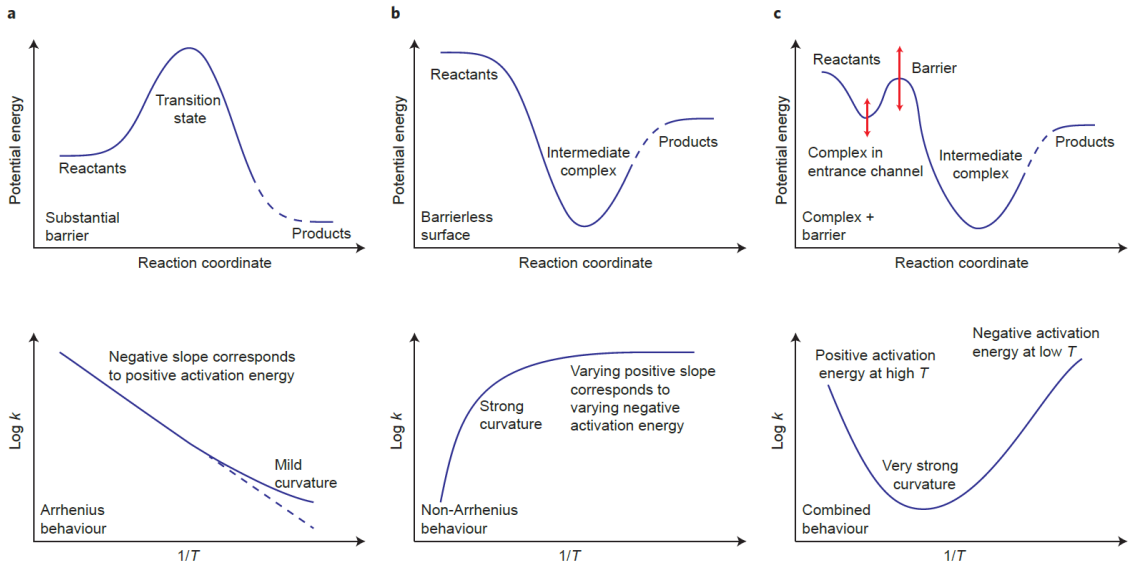

Figure 1.1: The upper panels display the potential energy over the course of a reaction and the lower panels display the Arrhenius plot for these reations. Reproduced from Sims, I. Tunnelling in space. Nature Chem 5, 734–736 (2013) [6]

There are many benefits to studying gas-phase reactions under low-temperature and low-pressure environments. First and foremost, low-temperature conditions enable us to control the reaction parameters. By controlling, and then varying, the reaction conditions, we can start to understand the role of individual variables on the outcome of a collision, such as the contribution from individual reactant quantum states or different distribution of energy. As the types of reactions we are interested in studying often take place in naturally occurring cold and low-pressure environments, such studies are also directly relevant to gas-phase chemistry in the interstellar medium (ISM) and in certain regions of Earth's (and other planetary) atmosphere(s). Fundamentally, precise studies of reaction kinetics and dynamics will also help us to challenge and benchmark existing models—as there

is a known lack of experimental measurements recorded under low-temperature conditions [3, 9, 10].

As briefly noted in the preceding paragraph, low-pressure and low-temperature environments are also directly relevant to the conditions found in the outer layers of Earth's atmosphere (150 K recorded between the mesosphere and the thermosphere [11]) and in regions of the interstellar medium. In diffuse interstellar clouds, temperatures typically range from 50–100 K, with a density of around 1×10^2–1×10^3 molecules cm^{-3}; in dense interstellar clouds, temperature are lower, sometimes down to 10 K, with higher densities around 1×10^4 molecules cm^{-3} [12,13].

As of September 2023, many of the 302 molecular species unambiguously identified in interstellar regions are radicals or ions [14,15], with the CH radical (first detected in 1937) and the CH^+ ion (detected in 1941) being the first and third species unambiguously identified in the interstellar medium [16, 17]. Both radicals and ions are abundant in many gas-phase environments. This makes it important to understand how these species react, as they are relevant for a vast array of multi-disciplinary fields, including atmospheric chemistry, interstellar modelling, industrial processes, and the healthcare industry [3]. In particular, radical species are involved in reactions occurring in the atmosphere, in plasmas, in combustion systems, in flames, and in the ISM. Radical species (such as OH, HO_2, C(^{3}P) and CH) are frequently formed as combustion by-products. A vast array of ionic species are formed through the intense short-wavelength radiation fields in astrochemical and atmospheric environments, and in chemi-ionisation processes within flames and

combustion engines.

The prevalence of radicals and ions in models of the chemistry that happens in the interstellar medium is unsurprising, given their high reactivity under low-temperature conditions [3, 18]. But their importance has not been followed by extensive gas-phase experimental studies. One of the main reasons for this lack of experimental data is the significant challenges associated with preparing a pure and controllable source of radical reactants; although some radicals like NO or O_2 can be purchased in pure form, they are often seeded in beams with carrier gases. As such, there are no straightforward methods for generating a pure beam of state-selected atomic or molecular gas-phase radicals with tuneable properties [1, 19]. When considering the reactions of radicals with ions—two inherently highly reactive species—there are very few methods that can be utilised to study the reaction(s) of interest in isolation, without needing to simultaneously measure and account for competing reaction processes with contaminant or background species that are present.

Several astronomical databases have been developed, including the Kinetic Database for Astrochemistry (KIDA https://kida.astrochem-tools.org/ [20]) and the UMIST Database for Astrochemistry (UDfA http://udfa.ajmarkwick.net/ [21]). These databases include rate coefficients and branching ratios for many reaction processes of astronomical relevance. However, much of the data included in these databases and models of interstellar chemistry rely upon untested theoretical predictions. In particular, there are very few experimental measurements on the branching ratios

between different product channels in systems where more than one set of reaction products can be formed [3, 22, 23].

This thesis addresses the need for new experimental methods to study important ion–radical reaction processes at low temperatures in the laboratory. To draw meaningful conclusion from these studies, it is essential to develop methods that enables us to control the reactants' properties as much as possible. To this end, we will first introduce a new cryogenic linear Paul trap as the source of cold, quantum state-selected molecular ions. We will also introduce a magnetic guide that can provide a source of state- and velocity-selected radical species. Our ultimate goal is to bring these two sources of reactants together to study ion–radical reactions under cold and controlled conditions.

1.2 Ion–radical reactions

1.2.1 Producing a radical beam

Radicals are usually prepared through photolysis, electron beam irradiation, or electric discharge methods [24, 25, 26]. However, producing the target radicals in this way results in a beam that also includes seed gases, other radical fragments, and precursor molecules. Furthermore, the velocity spread of the beam can be significant. It has been a long-standing challenge for the field to produce a pure, state-selected and velocity-selected radical beam.

One efficient way to manipulate radicals is to use magnetic fields. As radical species

are paramagnetic, they possess one or more unpaired electrons, and therefore have a magnetic dipole moment. In the presence of an external magnetic field, the Zeeman effect splits the energy levels of paramagnetic species. States that see an increase in their potential energy are called low-field seeking (LFS) states and those that see a decrease in their energy are called high-field seeking (HFS) states, as illustrated in Figure 1.2 with the Zeeman splitting of ground state OH radicals [27].

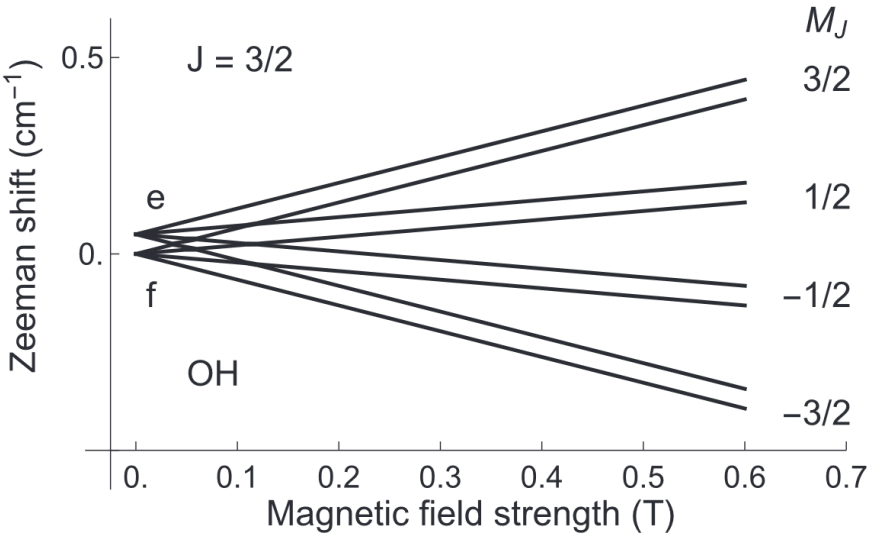

Figure 1.2: The Zeeman splitting of OH in its ground rovibronic state, $X^2\Pi_{3/2}$, $v = 0$, $J = 3/2$ with respect to the magnetic field strength B, reported in Tesla. J is the total angular momentum and m_J is the projection of J onto the external magnetic field axis. The parity components of the Λ-doublet are denoted by e and f. Reproduced from T. Damjanović et al New J. Phys. 23 105006 (2021) [27].

Zeeman decelerator

The first experimental demonstration of a Zeeman decelerator was made in 2007 on atomic radical species, H and metastable Ne [28, 29], and used to decelerate a first

molecular species, O_2, the following year [30, 31]. In the same principle as the one presented above, solenoid electromagnet coils are switched on and off to decelerate radical species in selected LFS states.

Our laboratory already has a source of radical beams: a Zeeman decelerator. Using the Zeeman effect described above, a Zeeman decelerator can lower the velocity of the targeted radicals in LFS states. The Zeeman decelerator in our laboratory is composed of 12 solenoid coils that are switched on sequentially to focus, both spatially and temporarily, and decelerate a subset of the target radical species in the incoming beam. Radicals are formed by photodissociation of a closed-shell precursor molecule (see Figure 1.3). By applying a current of 243 A through carefully timed pulses, a maximum magnetic field of 1.8 T is created at the center of each coil [32].

As explained above, the energy levels of the radicals—H atoms are targeted by our Zeeman decelerator—split as they pass through the magnetic fields within the decelerator coils. Particles in LFS states will see their potential energy increase at the expense of their kinetic energy. By turning the current off before particles reach the center of the coil, a small amount of kinetic energy can be permanently removed from the beam, causing the target species to slow down. By applying a precisely timed switching sequence to the 12 coils, a packet of quantum state-selected H-atoms can be slowed down to an arbitrary final velocity (within the limits of the decelerator coil durations; our current decelerator has successfully decelerated H-atoms to a final velocity of 75 $\mathrm{m\,s^{-1}}$) [33]. A schematic illustration of the Zeeman

decelerator is shown Figure 1.3.

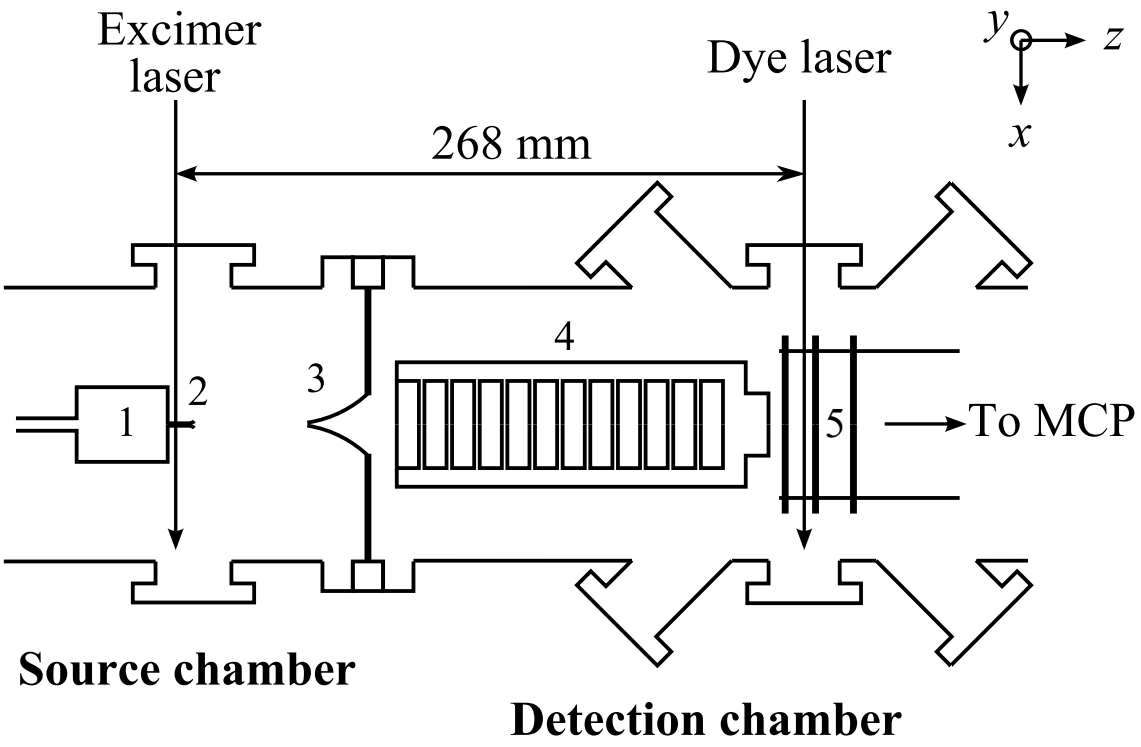

Figure 1.3: Schematic illustration of the Zeeman decelerator apparatus in the Liverpool laboratory: (1) pulsed valve, (2) capillary, (3) skimmer (4), Zeeman decelerator, (5) extraction plates. The length of the 12-stage Zeeman decelerator (labelled (4) in the figure) is 127.7 mm. Adapted from K. Dulitz et al. New J. Phys. 17 035005 (2015) [34].

After the Zeeman decelerator, the H atoms are ionised by a (2+1) resonance-enhanced multiphoton ionisation (REMPI) scheme. The ions are then detected by a microchannel plates (MCPs) detector and time-of-flight (ToF) profiles are obtained. The modal velocity of hydrogen atoms in the beam when the Zeeman decelerator is not used is 520 ± 70 m s^{-1}.

Three-dimensional numerical particle trajectory simulations can be used to determine the standard experimental switching sequences and to aid interpretation of the experimental ToF profiles. By considering the passage of a 'synchronous' particle travelling at the modal velocity along the central axis of the decelerator, the maximum kinetic energy that can be removed (set by the length of time that the final coil can be on) yields a final velocity of $v = 205\,\mathrm{m\,s^{-1}}$ after 12 coils. In this intuitive approach, each subsequent coil is switched 'on' for an increasing length of time, to account for the target particles slowing down as they move through the decelerator.

Alternatively, a former PhD student in the group implemented evolutionary algorithms to optimise the pulse sequences. The evolutionary algorithm seeks to optimise a set of parameters—here, the duration of the pulse of current applied to each coil—with respect to a fitness function. The fitness is determined by obtaining the maximum number of decelerated particles at the laser detection region. Figure 1.4 shows the velocity of simulated particles that are successfully decelerated to the target velocity, as a function of their position along the decelerator, with different switching sequences. The left hand side plot uses a standard switching sequence, and the incremental deceleration of the bunch of particles as they move through each decelerator stage can be seen. The right hand side plot employed an evolutionary algorithm switching sequence. Using the evolutionary algorithm, the lowest target final velocity that has been achieved is $v = 75\,\mathrm{m\,s^{-1}}$ [33].

Reaching lower velocities was possible because the evolutionary strategy optimisa-

tion (right) considered the passage of all H atoms in the incoming beam, not just a single synchronous particle. As such, particles that already had a lower velocity in the initial distribution were targeted to be decelerated, as can be seen from the increased spread of initial velocities and the different timings of the current pulses applied to the decelerator coils (Figure 1.4).

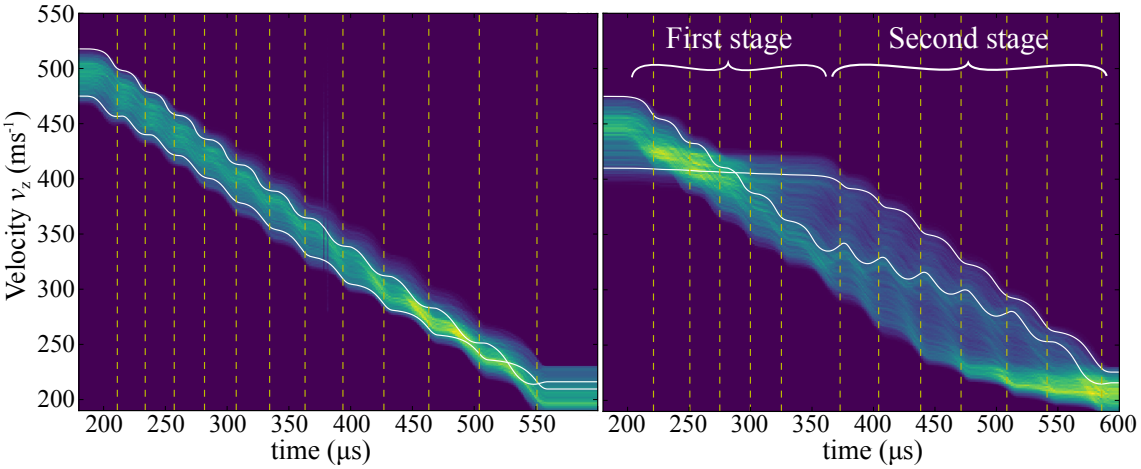

Figure 1.4: Evolution of the velocity of a decelerated packet of H atoms over time, as the radicals travel through the 12 coils of the Zeeman decelerator. The yellow vertical lines represent the time each coil was switched off. Left: standard pulse sequence, with $v_z^{final} = 205\,\mathrm{m\,s^{-1}}$; right: evolutionary algorithm pulse sequence, with $v_z^{final} = 200\,\mathrm{m\,s^{-1}}$. The labels 'first stage' and 'second stage' on the right plot refer to the different behaviour observed as the target radicals traverse the decelerator. Only the H atoms with higher velocities are targeted in the first stage, with all successfully decelerated species addressed in the second stage. Only the particles that reach the target velocity are shown. Reproduced from J. Toscano et al. New J.Phys. 19 083016 (2017) [33].

It should be noted that the beam emerging from the exit of the Zeeman decelerator contains a combination of the decelerated target species, undecelerated target species, and non-target species (such as seed gases, precursor molecules, and other

dissociation products). This is seen Figure 1.5, where the blue traces, representing decelerated profiles, where a packet of undecelerated particles reach the detector earlier (between 500 and 600 µs). The fully decelerated particles arrive to the detector later, corresponding to the peak furthest to the right (in all panels).

As such, the beam needs to be filtered—to remove the non-target species—in order to study controlled ion–radical reactions with trapped ions. Using an ion trap for reaction studies (i.e., a static target rather than a second beam) means that we need a pure beam of reactants to enter the trap, as otherwise unwanted species could react with the reactant ions. The magnetic guide presented in this thesis was built to that purpose: to filter out the unwanted species from the beam exiting the Zeeman decelerator. It is fully detailed in Chapter 7.

Alternative methods to produce and control a radical beam

Other methods have been developed to produce and control a radical beam over the years. Some of these techniques are briefly mentioned here; for a more comprehensive discussion, please see several recent review articles that touch on the topic [1, 30, 35, 36]. To date, only a handful of molecular radicals have been successfully Zeeman decelerated—including O_2 [31], OH [27] CH_3 [37], metastable He_2 [38], NH [39] and NO [40].

The Zeeman decelerator described in the previous sub-section employs a series of solenoid coils to achieve deceleration. An alternative design has also been

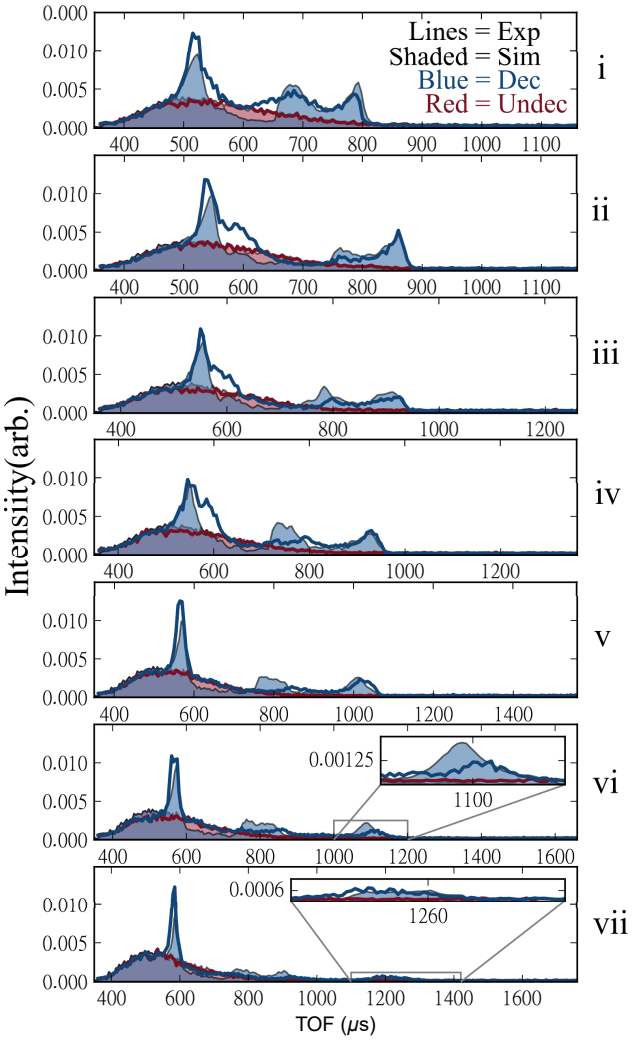

Figure 1.5: ToF traces obtained by applying the following pulse sequences: i) derived from a standard sequence for a final velocity of $205\,\mathrm{m\,s^{-1}}$; ii-vii) derived from evolutionary strategy optimisation, for a range of final velocities (stated below). The solid lines indicate the experimental traces, with the undecelerated profile (magnetic fields off) shown in red, and the decelerated profile (magnetic fields on) shown in dark blue. The shaded areas indicate the simulated traces, for both the decelerated (blue) and undecelerated (red) ToF profiles. For all traces, the initial velocity of the beam is a distribution centred at a velocity of approximately $500\,\mathrm{m\,s^{-1}}$. The final velocities for which the pulse sequences are optimised are the following: i) $205\,\mathrm{m\,s^{-1}}$, ii) $200\,\mathrm{m\,s^{-1}}$, iii) $175\,\mathrm{m\,s^{-1}}$, iv) $150\,\mathrm{m\,s^{-1}}$, v) $125\,\mathrm{m\,s^{-1}}$, vi) $100\,\mathrm{m\,s^{-1}}$, vii) $75\,\mathrm{m\,s^{-1}}$. Adapted from J. Toscano et al. New J. Phys. 19 083016 (2017) [33].

successfully developed, termed a travelling-wave (or moving magnetic trap) Zeeman decelerator (an example is shown in Figure 1.6). Its double-helix coil geometry forms a traveling magnetic wave along the coil axis that confines the targeted radicals in three dimensions and progressively decelerates them [27, 41]. Travelling wave decelerators are particularly suited to being combined with traps, where the goal is to spatially confine the decelerated species at the end of the decelerator (due to their improved transverse stability compared to conventional Zeeman decelerators) [1].

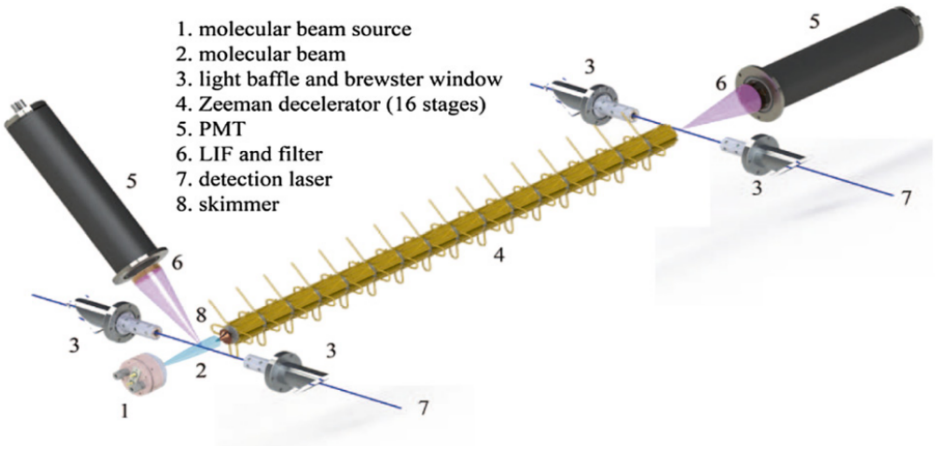

Figure 1.6: Schematic illustration of a travelling-wave Zeeman decelerator set-up, with the different parts labelled 1 to 8 with a legend provided in the figure. The beam is produced on the left-hand side, passing through a skimmer and then through the travelling-wave decelerator (yellow), before being detected by a photon-multiplier tube, depicted on the right-hand side. Reproduced from T. Damjanović et al. New J. Phys. 23 105007 (2021) [41].

Other recent developments in the manipulation of radical species include the Zeeman-Sisyphus deceleration of a molecular species, CaOH, to velocities below $15\,\mathrm{m\,s^{-1}}$ [42]. This method involves passing radical species through a spatially-

varying magnetic field produced by a series of permanent magnets, and optically pumping the species between LFS and HFS states as they traverse the different magnetic field regions. The radicals can then be confined in a magnetic or magneto-optical trap (MOT). A recent study examined the elastic and inelastic collisions of co-decelerated O_2 and Li that were combined in a superconducting trap [43]. This follows a study on collisions between molecular oxygen and atomic carbon using the same apparatus, where the reactants were co-Zeeman decelerated before being loaded into the trap. Significant enhancement in the decay rate of trapped $C(^3P_1)$ was observed when O_2 was co-trapped, and the reaction $C(^3P_1) + O_2(^3\Sigma_g^-) \rightarrow CO(^1\Sigma^+) + O(^1D)$ was identified as a likely loss mechanism (in addition to elastic and inelastic collision-induced trap loss) [1, 44].

Although these studies do not look at ion–radical reactions but radical–radical reactions, they pave the way to new techniques to control and study radicals.

The MOT technique mentioned above is a good way to obtain a stationary sample of radicals. A pair of coils in anti-Helmholtz configuration generates a quadrupolar magnetic field. Using six laser-cooling beams, propagating in each direction along the three axes, transitions between Zeeman levels in the inhomogeneous magnetic field generate optical forces that trap the neutral species at its center [35]. By superposing an ion trap with a MOT, one can co-trap ions and radicals and subsequently study their reactions. Interactions between species such as Li, Na and Rb have already been studied with ions in these hybrid traps [12, 32, 45, 46, 47]. Hall et al. have combined a linear Paul trap with a MOT, as shown Figure

1.7. Using this apparatus, they have studied the reaction between Ca^+ and Rb, and have observed non-radiative and radiative charge transfer, in addition to radiative association leading to the formation of $CaRb^+$ molecular ions [32,47,48].

While MOTs combined with ion traps have proven effective in studying a small number of ion–radical reactions, its broad applicability is limited since not all radicals—and, in particular, very few molecular radicals—can be efficiently laser-cooled.

A well-established method for the study of radical reactions is a flow-based technique known as CRESU (which stands for Cinétique de Réaction en Ecoulement Supersonique Uniforme [reaction kinetics in uniform supersonic flow]), developed in the 1980s to undertake rate coefficient measurements for ion–molecule, and subsequently also radical–neutral reactions, at low temperatures [49, 50]. At the heart of the CRESU technique is the Laval nozzle, an convergent-divergent nozzle consisting of convergent and divergent components, through which a gas expands isentropically and adiabatically from a reservoir (see Figure 1.8) [1]. The produced beam has a region with a well-defined and uniform pressure, temperature (that can be as low as 5.8 K), and density for several tens of centimetres (in most systems) [49]. By switching Laval nozzles and buffer gases, a series of beams with different properties can be produced, allowing reactions to be investigated under different temperature and pressure regimes.

Many reactions involving radicals have been investigated by CRESU at low

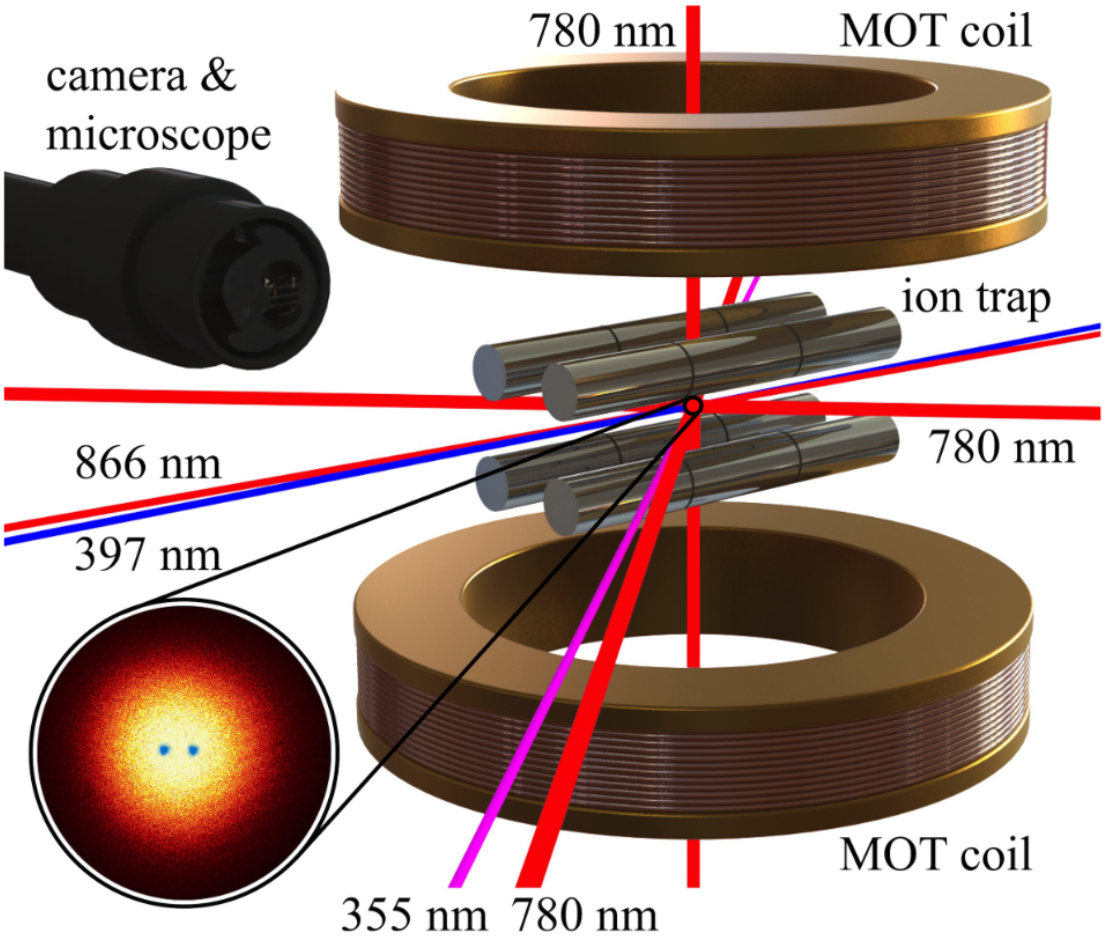

Figure 1.7: Schematic of the ion-atom hybrid trap at the University of Basel. The linear radiofrequency quadrupole ion trap is shown in silver at the center of the image, with the bronze MOT coils above and below. Both static and oscillating voltages are applied to the ion trap rods to confine Ca^+ at the trap center. The Ca^+ ions are subsequently laser-cooled by continuous wave diode lasers operating at 397 nm and 866 nm, with these laser cooling beams aligned along the ion trap center as indicated by the red and blue lines. Six other continuous wave diode laser beams intersect at the center of the trap, with a wavelength of 780 nm to cool Rb atoms and, as part of the MOT, to confine the atoms to the trap center. The inset image shows a cloud of laser-cooled Rb atoms in yellow/red, with two laser-cooled Ca^+ ions represented in blue. Reproduced from F. Hall et al. Molecular Physics, 111:14-15, 2020-2032, (2013) [47].

temperatures — such as the reaction of CN radicals with benzene that has been found to have no temperature dependence of the rate coefficient from 15 K to 295 K [51]. The main drawback of the CRESU method (and common with many flow methods) is that it is typically limited to measuring reactions that occur quickly due to the finite length of the flow tube and the fast movement of the flow [1, 32].

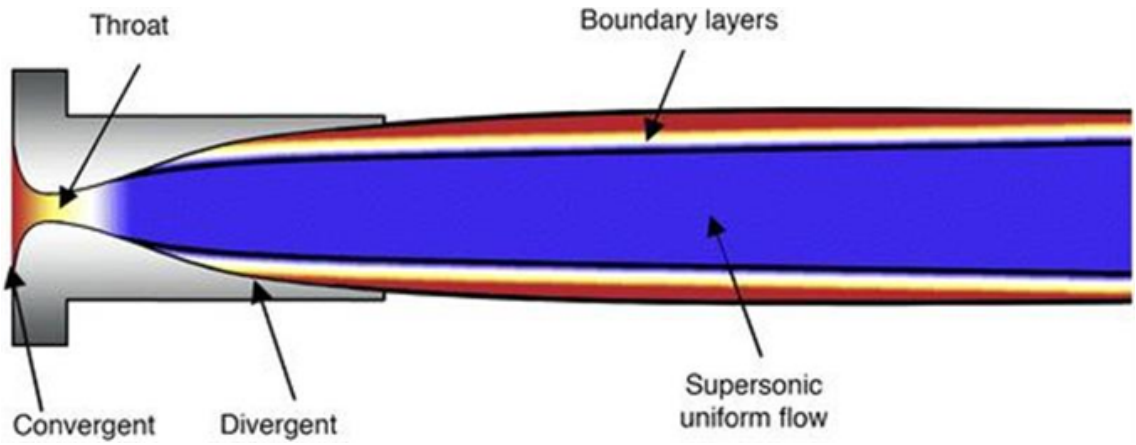

Figure 1.8: Schematic illustration of a Laval nozzle used in CRESU set-ups, with the different colours providing a temperature map. The red and yellow region represents the reservoir temperature, 298 K, and the blue region, representing the supersonic uniform flow, representing temperatures spanning from 20–200 K. Reproduced from M. Fournier et al. "Low-temperature Chemistry in Uniform Supersonic Flows", Cold Chemistry: Molecular Scattering and Reactivity Near Absolute Zero, Royal Society of Chemistry (2017) [5].

Each of the methods described above, in addition to many other techniques that have been adopted over the years, exhibit certain advantages and drawbacks. Our selected way to produce a controlled beam of radicals is to use a magnetic guide, with or without a Zeeman decelerator. The magnetic guide, as detailed in Chapter

7, was originally designed for filtering the beam from the Zeeman decelerator. Here, we show that it can also be employed as a stand-alone filter to obtain a state- and velocity-selected beam of a wider range of radicals, making it applicable to a range of radical species (including molecular radicals). In this way, we seek to maintain control over the properties of the beam whilst also employing a method that can be applied to a range of reaction systems.

1.2.2 Producing a source of molecular ions

State selectivity of molecular ions

A central and ongoing theme in this thesis is the importance of controlling as many reaction parameters as possible. One key parameter that experimentalists want to have control over is the quantum state of the reactants. There have been numerous reaction studies involving state-selected ions confined within ion traps. For example, the study of NH_3 and ND_3 with state-selected rare gas ions Xe^+, Kr^+ and Ar^+ has been undertaken by members of our group. This study has revealed a inverse kinetic isotope effect, where the deuterated ammonia unexpectedly reacted faster with the rare gas ions than the hydrogenated species [52]. Similarly, Tong et al. have studied collisions between $N_2{}^+$ ions in well-defined rovibrational states and neutral N_2 molecules. This has led to new information on the translation-to-rotation energy transfer that happens during this charge transfer reaction [53].

REMPI techniques can allow ionic reactants to be formed in a selected quantum state. The work in this thesis is focused on developing a new instrument for the study of ion–radical reactions within a Coulomb crystal environment. The many

advantages of this approach, along with the principles of ion trapping, are set out in Chapter 2. What is important to note at this stage is that it is challenging to maintain state selectivity in the quantum state population of most trapped molecular ions. This is primarily due to the timescale of the measurements; reactions in traps can be studied for many minutes. Such long timescales offer exceptional sensitivity, but also mean that the reaction conditions (including the properties of the ionic reactants) need to be controlled over an extended period of time. As there are only elastic collisions between co-trapped ions (see Chapter 2 for further detail on this), and atomic ions have no rotational or vibrational degrees of freedom, the atomic ions typically remain in the state that they are prepared in for extended periods of time. However, keeping molecular ions (except homonuclear diatomic species) in a selected quantum state is difficult due to interactions with ambient blackbody radiation (BBR) driving rotational and vibrational transitions. [54]

Molecular ions are deeply important for chemistry in the ISM. For example, the reaction of $C_2H_2^+$ with H_2 shows the reopening of the bimolecular $C_2H_3^+$ channel at low energy [18, 55], a temperature dependence that was unexpected. In ion traps, laser-cooled species can sympathetically cool ions that are trapped alongside them (a process explained in details in Chapter 2), but this only cools their translational degrees of freedom. Most molecular ions interact with ambient BBR and subsequently loose their state selectivity. The impact of BBR on state-selected molecular ions held within a room-temperature ion trap has been studied by previous group members, as published in Deb et al. [18]. Looking at $C_2H_2^+$ ions, it was demonstrated that the spectrum of black body radiation at 300 K, shown in

Figure 1.9, is coincident with the peak of the IR-active vibrational mode—resulting in rapid BBR-mediated population redistribution at 300 K.

The BBR spectra were obtained by the numerical solution to the coupled rate equation

$$-\frac{dn_i}{dt} = \sum_j B_{ij}\rho_T(\omega_{ij})n_i - \sum_j [B_{ji}\rho_T(\omega_{ij}) + A_{ij}]n_j \tag{1.1}$$

where ρ_T is the spectral density, that includes both the absorption and the emission from BBR and the laser pumping, and B_{ij} and A_{ij} are the Einstein coefficients for stimulated emission/absorption and spontaneous emission, respectively. The dependence of BBR-induced population redistribution in $C_2H_2^+$ can be attributed to several factors, including the line strength of the rovibrational transition, the vibrational transition dipole moment, the energy difference between the states, and the blackbody temperature [18].

Looking at the impact of BBR on the population of the rovibrational ground state, simulations have been run to look at the fraction of population in this state as a function of time, shown Figure 1.10. With all ions population initially state-selected in the ground rovibrational state, it can be seen that at 300 K, in a matter of seconds, the ground state is depopulated. Clearly, it is not possible to study reactions with state-selected $C_2H_2^+$ ions on the intended timescale of several minutes in a 300 K ion trap.

Another interesting finding from this study is the importance of temperature; at temperatures below 77 K, the state-selected population could be kept in the rovibra-

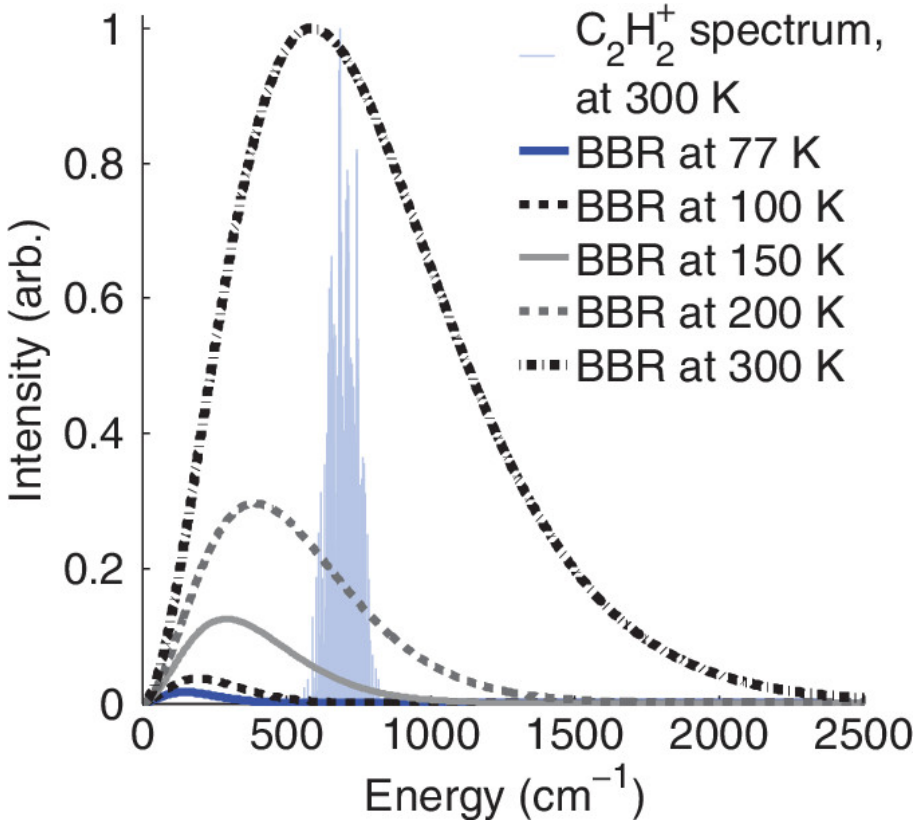

Figure 1.9: The light blue solid spectrum corresponds to the simulated excitation spectrum of the ν_5 vibrational mode in $C_2H_2^+$ at 300 K. The solid lines represent the BBR spectrum at a range of temperatures, 300 K, 200 K, 150 K, 100 K, and 77 K. Reprinted from N. Deb et al., J. Chem. Phys. 140, 164314 (2014) [18], with the permission of AIP Publishing.

tional ground state for an extended period of time, with no BBR-driven population redistribution observed on the timescale of the simulations (10 min). This lowest temperature for which thermalisation does not occur depends on the properties of the molecular ion of interest; while 77 K was sufficient for $C_2H_2^+$, lower temperatures would be required to maintain state selectivity for some other molecular ions.

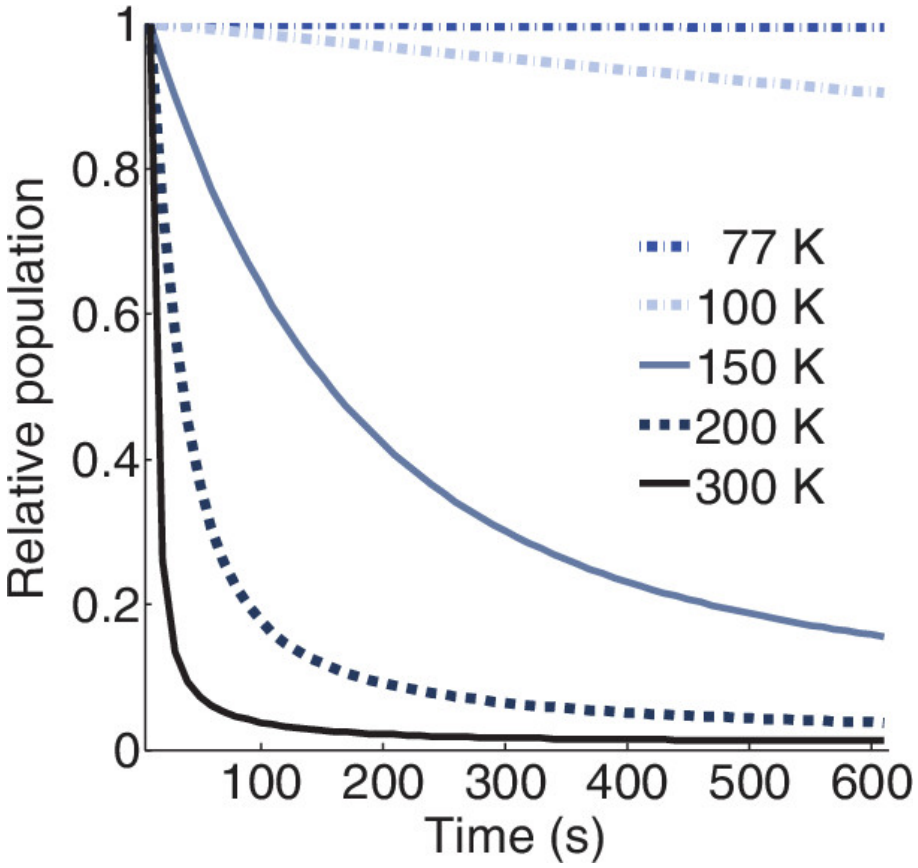

Figure 1.10: Evolution of the population of $C_2H_2^+$ ions in the $^2\Pi_{3/2}$, $v_5 = 0$, $J = 3/2$ state (the rovibrational ground state), at different temperatures, from 77 to 300 K. Reprinted from N. Deb et al., J. Chem. Phys. 140, 164314 (2014) [18], with the permission of AIP Publishing.

Techniques to study molecular ions

Multiple techniques have been explored to maintain state-selectivity of trapped molecular ions. One way to avoid issues with BBR-mediated population redistribution is to study homonuclear diatomic ions. As this class of molecular ions do not have a transition dipole moment, they have no interaction with the BBR field, and so the initial state selectivity is maintained. Both Tong et al. [56, 57] and Gardner

et al. [58] have looked at N_2^+, produced in selected rovibronic quantum states through threshold photoionization. While this approach has very successfully led to interesting studies of homonuclear diatomic ions, it is not applicable to most other molecular ionic species [57].

One other way to obtain some degree of state-selectivity in trapped molecular ions is to combine an ion trap with a MOT, as discussed above (Figure 1.7). Rellegert et al. have demonstrated this approach by trapping $BaCl^+$ molecular ions that are sympathetically cooled by inelastic collisions with ultra-cold calcium atoms (confined in the MOT). The atoms can undergo inelastic collisions with $BaCl^+$ as they can get closer than is possible with cation–cation collisions, cooling down the internal degrees of freedom in the molecular ions. Although this study has demonstrated vibrational cooling of the $BaCl^+$, they have not been able to verify the extent of rotational cooling, and it may be challenging to achieve full state selectivity through inelastic collisions alone [59].

Several research groups have looked at optical pumping techniques to cool the rotational degrees of freedom of heteronuclear diatomic molecules. Schneider et al. have looked at HD^+ and have been able to obtain 78% of the population in the rovibrational ground-state [60], while Højbjerre et al. have studied MgH^+ ions, where they were able to maintain 36.7% of population in the rotational ground state [61, 62]. While successful, this BBR-mediated laser-driven redistribution of rotational population is limited to certain classes of molecular ions, where there are appropriate laser cooling schemes. Furthermore, each molecular ion will need a

different laser cooling scheme, limiting the range of species that can be studied in this way.

Finally, the most generally applicable approach—and the method that we have adopted—to maintaining state selectivity in trapped molecular ions is to cryogenically cool the ion trap environment, thereby suppressing BBR-induced population transfer. The existing designs of cryogenic ion traps are briefly described in the next section.

Cryogenic ion traps

Most of the cryogenic ion traps that have been developed to date are surface-electrode ion traps. These surface traps are typically designed for quantum information processors and quantum simulators [63, 64, 65, 66]. One such design, described by Dubielzig et al. [67], also possess nested temperature stages and optical access to the trap centre. Surface traps allow for miniaturization of trap designs. They have all electrodes arranged in a plane, as shown Figure 1.11. The trap depth is on the order of a few hundred meV, whereas the trap depth of a linear Paul trap is up to several eV [35]. The limited trap depth is one of the main drawbacks of the surface trap, along with their limited optical access [68]. As such, they are not suitable for the study of a range of reaction processes.

A number of cryogenic multipole (typically 22-pole) traps have been developed for spectroscopic measurements and cold ion–neutral reaction studies. Reactions have been studied in 22-pole traps over a large temperature range, spanning 10–300 K.

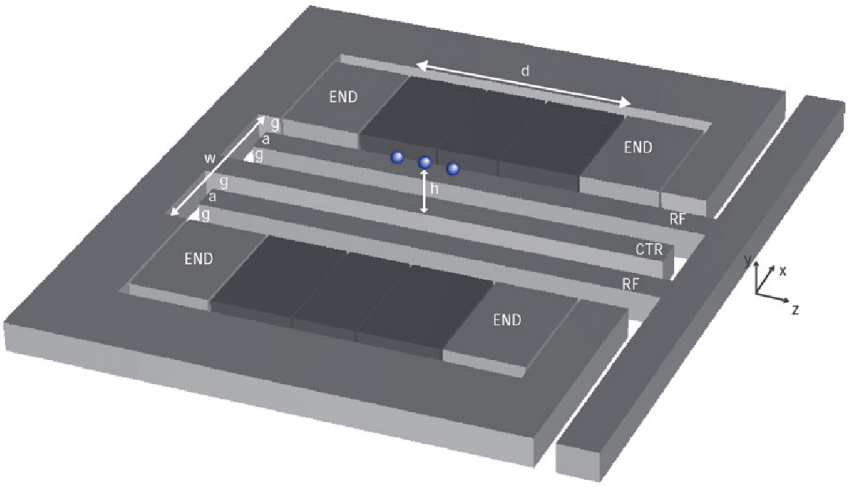

Figure 1.11: Schematic illustration of a five-wire surface-electrode ion trap. RF: radio-frequency electrodes; CTR: center electrode; END: endcap electrodes. The distances represented in white arrows are h, w and d and are the distance of the trapped ions to the electrode surface, the distance between the endcaps in the x direction and the distance between the endcaps in the z direction respectively. Finally, a and g are the widths of the electrodes of the inter-electrode gaps respectively. Reproduced from I. M. Georgescu, Phys. Chem. Chem. Phys., 13, 18852-18858 (2011) [69].

While it is challenging to reach temperatures below 10-20 K, buffer gas cooling can allow reactions to be studied at such low temperatures. Buffer gas cooling is more efficient in multipole traps than in a quadrupole ion trap because of the shape of the trapping potential [54]. The high number of electrodes increases the flatness of the potential at the trap center [2]. This also means that the effective trap volume is larger than a quadrupole ion trap. Gerlich et al. have used cryogenic 22-pole traps with helium buffer gas cooling to look at the radiative association of CH_3^+ and $C_2H_2^+$ with H_2 at a nominal temperature of 10 K [70].

A new design of the 22-pole trap has been made for the Atomic Beam 22-pole ion trap ($AB-22PT$) apparatus. This design includes a copper case around the ion trap, that is directly connected to a closed cycle helium refrigerator, and the temperature at the ion trap can be set between 10 and 100 K [71, 72]. This design has partially inspired the design of our cryogenic ion trap. Using the $AB-22PT$ apparatus, the reactions of doubly charged carbon ions, C_2^+, have been studied with O_2, N_2, CO, and HD at low temperatures [73].

While 22-pole trap environments offer many advantages, they are not suited for laser cooling the trapped ions or imaging fluorescence (owing to the limited optical access and the flat shape of the trapping potential) [74].

Cryogenic macroscopic quadrupole traps are much less prevalent. One such example involves a linear Paul trap placed in a liquid He vacuum Dewar, to reduce the BBR radiation the trapped ions are subjected to [75]. A more recent cryogenic ion trap apparatus design including a macroscopic linear Paul quadrupole ion trap was introduced by Schwartz et al. and termed cryogenic Paul trap experiment (CryPTEx) [76]. This apparatus was developed by a collaboration involving research groups at Max-Planck-Institut für Kernphysik (MPIK) in Heidelberg and the Ion Trap Group at the University of Åarhus. With nested temperature stages maintaining optical access to the trap centre for lasers and imaging purposes, the original CryPTEx trap has been the main inspiration for the design of our own cryogenic ion trap. Comparisons between the CryPTEx design and our own cryogenic ion trap are developed further in Chapter 3. The CryPTEx appara-

tus was designed for the study of highly charged ions, although the properties of molecular MgH^+ ions have been well studied within the trap environment [77,78,79].

Using the CryPTEx set-up, the decay rate of the first excited vibrational state to the ground state has been studied in MgH^+ ions [78]. Buffer gas cooling has been introduced to alter the population distribution of the internal degrees of freedom of sympathetically cooled MgH^+ ions [79]. In this way, a minimum rotational temperature of 7.5 K has been reached following this approach. By using resonance-enhanced multiphoton dissociation (REMPD) with rotational-state resolution, the population in the individual rotational states was able to be directly measured. The impact of the Coulomb crystal size on the internal population distribution has also been explored, with the results shown Figure 1.12. It can be seen how the bigger the crystal, the higher the temperature (that is, the more population that can be found in excited rotational states). This is induced by the radio-frequency-field-induced micromotion that depends on the position of the ions in the trap.

Since the first CryPTEx apparatus was introduced in 2014, the different members of the collaboration have built new CryPTEx apparatus for other applications. The CryPTEx–PTB, built at the Physikalisch-Technische Bundesanstalt in Braunschweig by Leopold et al., is designed for studying quantum logic spectroscopy of highly charged ions [80]. Another recent version of the CryPTEx, developed at (MPIK) in Heidelberg and named CryPTEx-SC, is designed for studying optical frequency metrology with ionic species [81]. All of these apparatus will be described

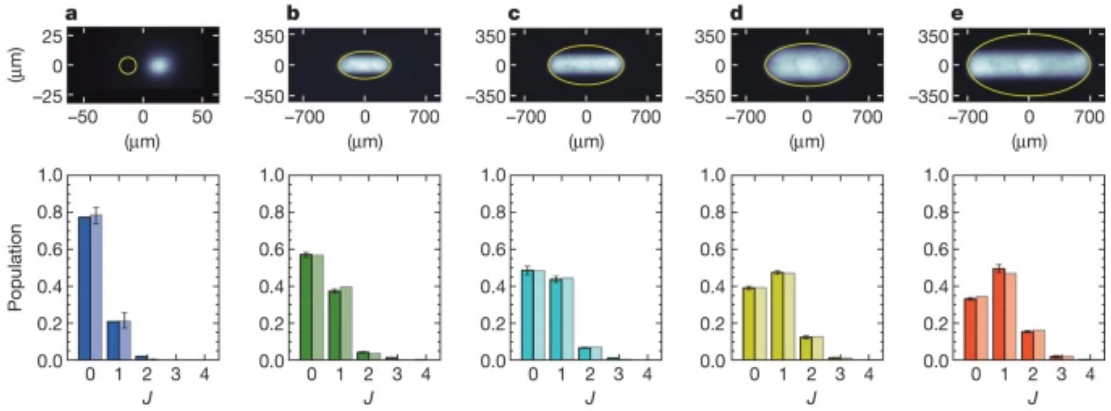

Figure 1.12: The upper panel presents images of Coulomb crystals of different numbers of Mg^+ (fluorescing and visible in white) and MgH^+ ions (non-fluorescing, indicated by the yellow circle in a, and by the dark regions inside the yellow ellipse that indicates the outer boundary of the Coulomb crystals in b–e). The number of Mg^+ and MgH^+ ions (respectively) within each of the crystals are estimated to be: a) (1, 1) , b) (950, 600), c) (1,750, 2,750), d) (4,900, 1,250), e) (5,500, 13,200). The bottom panels show the measured distribution of rotational states in dark-coloured bars, along with the best fits to thermal distributions in light-coloured bars for each crystal size. J is the rotational quantum number. Based on these fits, the authors have established the rotational temperatures of the MgH^+ ions within each crystal as: a) 7.6 K, b) 12 K, c) 15 K, d) 20 K, e) 23 K. Adapted from A. Hansen et al., Nature 508, 76–79 (2014) [79].

and compared with our own cryogenic linear Paul trap in Chapter 3.

While there have been some excellent cryogenic ion trap set-ups previously introduced, none of these were designed for the study of reactions within Coulomb crystals. The cryogenic ion trap described in this thesis represents the first cryogenic quadrupole ion trap with optical access for lasers and in-built imaging and time-of-flight detection capabilities. It is the inclusion of time-of-flight detection capabilities that will enable us to study not only the reaction kinetics, but also the

dynamics of chemical reactions involving state-selected molecular ions.

1.3 Aims

The overall aim of this thesis is to devise a novel instrument for the study of reaction systems involving molecular ions and radicals at low temperatures with control over as many reaction parameters as possible. To achieve this goal, we have designed and constructed a cryogenic ion trap chamber (for confining state-selected molecular ions) and a Zeeman decelerator with a magnetic guide (for producing a slow-moving beam of radicals).

Chapter 2 sets out the operating principles of the linear Paul ion trap adopted in our work. The design of the cryogenic ion trap apparatus is detailed in Chapter 3, with an emphasis on the choices behind the design and the multiple challenges that arose from the introduction of a cryocooler system. A new optical system has also been developed specifically for this apparatus. The design, characterisation and testing of the optical system is explained in Chapter 4. We report the results of the characterisation of the main components of the cryogenic ion trap and compare these experimental measurements with our predictions in Chapter 5. Following the characterisation of the apparatus, the first observation of Coulomb crystals and of ToF traces recorded with the cryogenic ion trap are presented in Chapter 6.

The characterisation of the magnetic guide as a source of state- and velocity-selected

hydrogen radicals is explained in Chapter 7. Finally, the conclusion chapter summarises the key findings of the thesis—the successful design, construction, characterisation and measurements undertaken with the cryogenic ion trap apparatus—and sets out the next steps that will be taken for the study of ion–radical reaction processes in the very near future.

Chapter 2

Background

2.1 Ion trapping

The possibility of trapping particles for extended periods of time has given rise to major advancements in many fields, from cold chemistry to quantum computing. This has been made possible thanks to the development of ion trapping techniques, for which Wolfgang Paul and Hans Dehmelt were awarded the Nobel Prize for Physics in 1989. To successfully trap an ion, we need a quadrupole potential with a three-dimensional minimum, satisfying the equation $\phi(x, y, z) = Ax^2 + By^2 + Cz^2$, where A, B, and C are all > 0. However, as Laplace's equation requires the confining force from the potential to have no divergence ($\nabla^2\phi = 0$), the sum of the coefficients must equal zero ($A + B + C = 0$). The implications of this are summarised by Earnshaw's theorem: that it is not possible to trap a charged particle in all three dimensions using static electric fields.

The Paul ion trap, invented by Wolfgang Paul, uses a combination of rapidly oscillating radiofrequency voltages that dynamically confine the particles in the $x - y$ plane, and static voltages to provide confinement along the z axis. Penning traps, on the other hand, use a combination of static electric and magnetic fields

to confine ions [2]. While Penning traps have been previously used for studying Coulomb crystals [35, 82, 83], the presence of magnetic fields complicates the laser cooling and will also make studying reactions involving radicals more complex, as the radicals will be affected by the magnetic fields.

Following the example of several research groups studying reactions in Coulomb crystals, including our own group, we have chosen to use a radiofrequency trap to confine ions. A combination of radiofrequency and static voltages are applied to electrodes to confine particles at the trap center. The first design of a Paul ion trap [84] was composed of a ring and two endcaps, forming 'hyperboloids' of revolution (see Figure 2.1). Since this first design, a range of different ion trap geometries have been introduced to accommodate different applications.

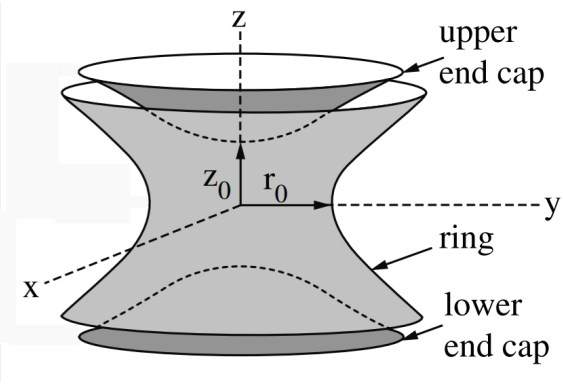

Figure 2.1: Basic arrangement of electrodes for Paul traps. The inner electrode surfaces are hyperboloids. Reproduced from G. Werth et al. Charged Particle Traps II. Springer Series on Atomic, Optical, and Plasma Physics, vol 54. Springer (2009) [85].

One of the more recent trap designs involves a surface or chip-based ion trap,

devised for quantum information processing applications [86, 87]. While these surface traps can offer more flexibility in the manipulation of the ions (and are comparatively straightforward to cool), they exhibit smaller trap depths than other radiofrequency traps and therefore make it difficult to trap bigger ion clouds [35]. The most commonly used trap for producing Coulomb crystals is the linear quadrupole Paul trap. Constituted of 4 parallel rods, with each rod separated into three segments, this type of ion trap is ideal for trapping bigger ion clouds as there is a zero-line potential along the central trap axis (parallel to the trap rods) instead of just a point in the case of the hyperbolic structure of the classic Paul trap [84,87].

A significant number of ion–molecule reactions have been studied within multipole (especially 22-pole) traps, including under cryogenic environments [70, 88, 89, 90]. While it is possible to confine large ion clouds within 22-pole traps, the number of rods imposes physical challenges, limiting optical access to the trap in the plane perpendicular to the trap axis (i.e., making the collection of fluorescence emitted by laser-cooled ions very challenging). Also, given the flatter nature of the trapping potential, even forming Coulomb crystals in 22-pole traps would be very challenging. Deiglmayr et al. [91], and more recently Gestlinger et al. [92] have developed an octupole and 16-pole wire ion trap (respectively), improving optical access to the trap center, but to date there have not been reports of Coulomb crystals being successfully formed in these multipole wire traps.

Finally, and perhaps more importantly, there is already a working quadrupole Paul trap experiment in our laboratory that has successfully been used to conduct

reaction studies over the past several years. The advantages of replicating design elements from our existing trap, facilitating the sharing of information and instruments in our laboratory, made adopting a linear Paul quadrupole radiofrequency (RF) ion trap the obvious choice for this project.

This chapter is thus going to focus on the linear (quadrupole) Paul trap geometry that is used in the later chapters of this thesis.

2.1.1 Linear Paul ion traps

As briefly mentioned previously, the conventional quadrupole linear Paul trap design is composed of four parallel cylindrical electrodes, each separated into three segments (see Figure 2.2). Each segment is electrically isolated from one another in order to allow for the application of independent voltages to individual segments.

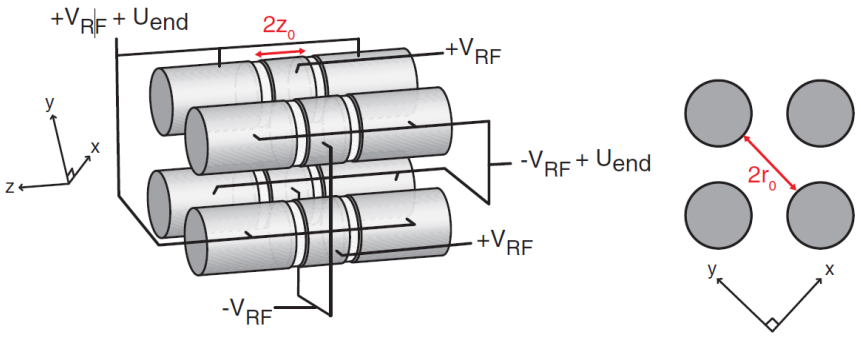

Figure 2.2: Conventional linear Paul trap design with a quadrupole configuration of rods. The voltages applied to each segment of the rods are shown, along with the z_0 and r_0 measurements. Reproduced from Alexander Gingell's thesis [23].

We started with a conventional linear Paul trap design, and then adapted it to fit our needs. To reach temperatures $< 10\,\mathrm{K}$ in the innermost part of the apparatus, i.e. the ion trap, it was important to encase the trap in copper shielding, which itself is nested in a second temperature stage (this is further detailed in Chapter 3). In order to achieve good thermal contact between the trap rods and the copper shielding, to keep the volume of the innermost stage small, and to minimise the size of openings in the shielding, it was decided to cut the rods in half along their long (trap) axis. The resulting trapping rods are fitted onto a copper case, as illustrated Figure 2.3, with further details of the design provided in Chapter 3.

The parameters of the new cryogenic linear Paul trap are defined in Table 2.1.

Parameter	Definition	Typical experimental values
$2V_{\mathrm{RF}}$	RF voltage, peak-to-peak	70 – 300 V
Ω_{RF}	RF frequency	$2.55 \times 2\pi$ MHz
U_{end}	endcap voltage	2 – 40 V
$2z_0$	endcap separation	5.8 mm
$2r_0$	diagonal electrode surface separation	7.00 mm
η	geometric factor	≈ 0.27
R	electrode radius	4 mm

Table 2.1: Operating parameters and dimensions of the cryogenic linear Paul trap described in this work. When applying the voltages to the rods, we are working with a peak-to-peak amplitude, here referred to as $2V_{\mathrm{RF}}$.

The radial confinement (in the x and y dimensions) of the ions is obtained by applying oscillating radiofrequency voltages to the four rods, of equal amplitude but with a 180° phase shift between two neighbouring electrodes, as illustrated in Figure 2.2. This creates an oscillating potential saddle point, which traps the ions

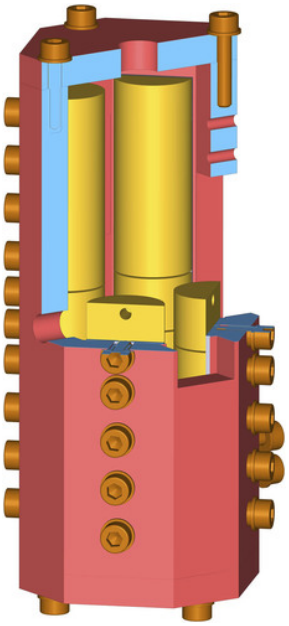

Figure 2.3: Schematic illustration of the linear quadrupole ion trap of the cryogenic ion trap set-up at the University of Liverpool. The cut view shows the interior region, with the trap rods depicted in yellow, with the surrounding ion trap holder in red (with a blue cross section). The small orange screws fix the rod segments to the trap holder, and serve as electrical connections. One of the ceramic insulators (between the rod and the ion trap holder) can be seen in grey on the right hand side. Reproduced from C. Miossec et al., Rev Sci Instrum, 93 (3): 033201 (2022) [74].

dynamically in the $(x,\ y)$ plane. This time-dependant RF voltage is defined as $V_{\mathrm{RF}}(t) = V_{\mathrm{RF}} \cos(\Omega_{\mathrm{RF}} t)$, where V_{RF} is the amplitude of the RF voltage, and Ω_{RF} is the angular radiofrequency. This gives rise to an electric potential ϕ_{RF} given by:

$$\phi_{\mathrm{RF}}(x, y, t) = V_{\mathrm{RF}} \cos(\Omega_{\mathrm{RF}} t) \left(\frac{x^2 - y^2}{r_0^2} \right) \tag{2.1}$$

where r_0 is the distance from the center of the ion trap to the rods (illustrated in Figure 2.2).

The axial confinement (in the z-dimension) is obtained by applying a static DC

voltage, U_{end}, to the end segment of each rod, called endcaps. The potential arising from the static voltages is therefore:

$$\phi_{\text{end}}(x, y, z) = \frac{\eta U_{\text{end}}}{z_0^2}\left(z^2 - \frac{x^2 + y^2}{2}\right) \tag{2.2}$$

where $2z_0$ is the distance between the endcaps (illustrated in Figure 2.3) and η is a geometrical factor to account for the fact that the rods are circular and not hyperbolic (and can also account for other minor imperfections in the machining of the rods).

The total electric potential is thus:

$$\phi(x, y, z, t) = \phi_{\text{RF}} + \phi_{\text{end}} = \frac{\eta U_{\text{end}}}{z_0^2}\left(z^2 - \frac{x^2 + y^2}{2}\right) + V_{\text{RF}} \cos\left(\Omega_{\text{RF}} t\right)\left(\frac{x^2 - y^2}{r_0^2}\right) \tag{2.3}$$

The motion of trapped ions in a linear Paul trap can be described as containing two components: a fast "micromotion" induced by the oscillating RF potential, and a slower thermal "secular" motion. The micromotion is minimised along the trap centre (the RF null line); the secular motion corresponds to the thermal motion of the ions, and can be addressed by laser cooling methods (developed further in this Chapter) [2, 35, 87].

The Newtonian equations of motion for an ion of mass m and charge Q in an electric field given by Equation 2.3 can be derived from $F = ma = -Q\nabla\phi(x, y, z, t)$ as:

$$\ddot{x} + \left(-\frac{\eta Q U_{\text{end}}}{m z_0^2} + \frac{2 Q V_{\text{RF}}}{m r_0^2} \cos\left(\Omega_{\text{RF}} t\right)\right) x = 0 \tag{2.4}$$

$$\ddot{y} + \left(-\frac{\eta Q U_{\text{end}}}{m z_0^2} - \frac{2 Q V_{\text{RF}}}{m r_0^2} \cos\left(\Omega_{\text{RF}} t\right)\right) y = 0 \tag{2.5}$$

$$\ddot{z} + \left(\frac{2\eta Q U_{\text{end}}}{m z_0^2}\right) z = 0 \tag{2.6}$$

By replacing $\tau = \frac{1}{2}\Omega_{\text{RF}}$, the equations of motion are written in the form of the Mathieu equations, that follow:

$$\frac{d^2u}{d\tau^2} + [a_u - 2q_u \cos(2\tau)]u = 0, u \in x, y, z \tag{2.7}$$

where a_u and q_u are two dimensionless parameters known as Mathieu parameters [35, 84, 87, 93, 94, 95].

We obtain the following equations of motion:

$$\frac{d^2x}{d\tau^2} + \left(-\frac{4\eta Q U_{\text{end}}}{m z_0^2 \Omega_{\text{RF}}^2} + \frac{8 Q V_{\text{RF}}}{m r_0^2 \Omega_{\text{RF}}^2} \cos(2\tau)\right) x = 0 \tag{2.8}$$

$$\frac{d^2y}{d\tau^2} + \left(-\frac{4\eta Q U_{\text{end}}}{m z_0^2 \Omega_{\text{RF}}^2} - \frac{8 Q V_{\text{RF}}}{m r_0^2 \Omega_{\text{RF}}^2} \cos(2\tau)\right) y = 0 \tag{2.9}$$

$$\frac{d^2z}{d\tau^2} + \left(\frac{8\eta Q U_{\text{end}}}{m z_0^2 \Omega_{\text{RF}}^2}\right) z = 0 \tag{2.10}$$

From these equations we can express the Mathieu parameters as the following:

$$a_x = a_y = -\frac{1}{2} a_z = -\frac{4\eta Q U_{\text{end}}}{m z_0^2 \Omega_{\text{RF}}^2} \tag{2.11}$$

$$q_x = -q_y = -\frac{4 Q V_{\text{RF}}}{m r_0^2 \Omega_{\text{RF}}^2}, q_z = 0 \tag{2.12}$$

The solutions to the Mathieu equation are very well known [84, 93, 94, 96], and depend only on the parameters a_u and q_u defined in Equations 2.11 and 2.12 and not on the initial conditions of the ion. The Mathieu equations define regions where the trajectories of ions are stable, resulting in these ions being able to be confined by the trap. In the case of an unstable region, the resulting ion trajectory

will tend to infinity with time. A stability diagram can be drawn from this by mapping the stability region as a function of the parameters a_u and q_u, for a given trap frequency, ion, and trap geometry. An example of a stability diagram is shown Figure 2.4 for Ca^+ ions in the cryogenic ion trap operating at $2.55 \times 2\pi$ MHz. The region in black indicates the stable trapping region, where ions can be successfully confined for extended periods of time.

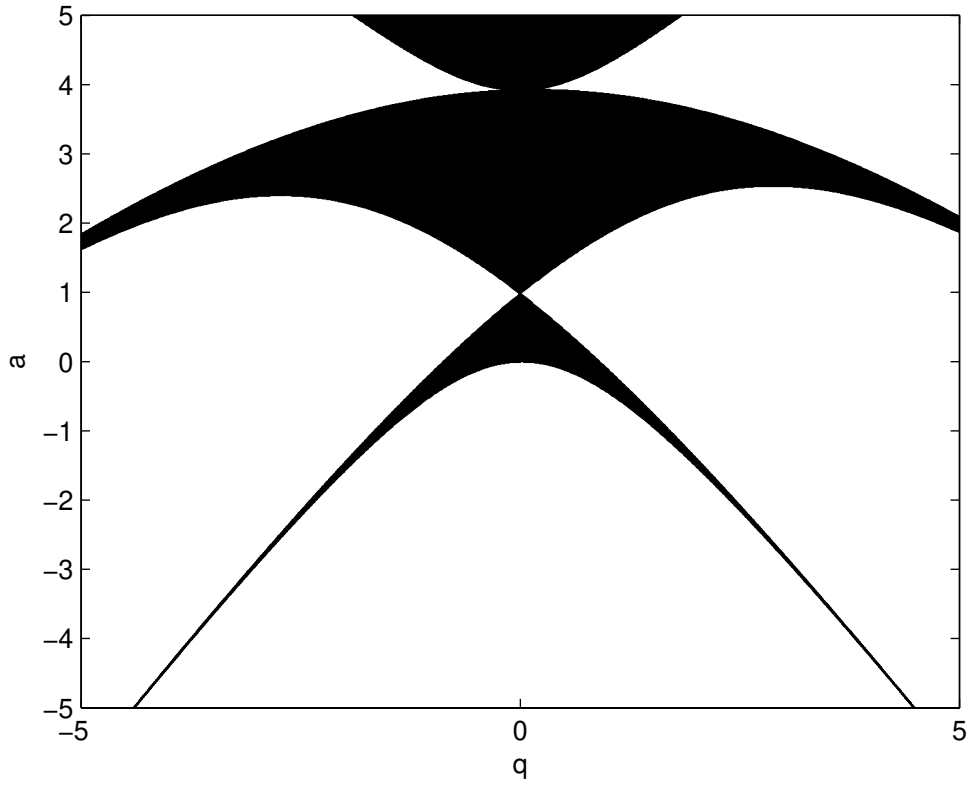

Figure 2.4: Stability diagram of Ca^+ ions in our cryogenic linear Paul trap operating at $\Omega_{RF} = 2\pi \times 2.55$ MHz. The stability region is the filled region (in black), i.e where the requirements for the stability are satisfied.

Most regions of the stability diagram shown in Figure 2.4 are not accessible experimentally. The experimentally accessible region of the stability diagram is shown in Figure 2.5, as a function of V_{RF} and U_{end}. Indeed, for a given value of Ω_{RF}, the stability diagram can be plotted in terms of V_{RF} and U_{end} by expressing these values as a function of the a and q parameters:

$$U_{\mathrm{end}} = -a_x \frac{m z_0^2 \Omega_{\mathrm{RF}}^2}{4\eta Q} = -a_y \frac{m z_0^2 \Omega_{\mathrm{RF}}^2}{4\eta Q} \tag{2.13}$$

$$V_{\mathrm{RF}} = -q_x \frac{m r_0^2 \Omega_{\mathrm{RF}}^2}{4Q} = q_y \frac{m r_0^2 \Omega_{\mathrm{RF}}^2}{4Q} \tag{2.14}$$

Figure 2.5 shows the stability diagram for both Ca^+ and $NH_3{}^+$ ions in the cryogenic ion trap operating at a frequency of $2.55 \times 2\pi$ MHz.

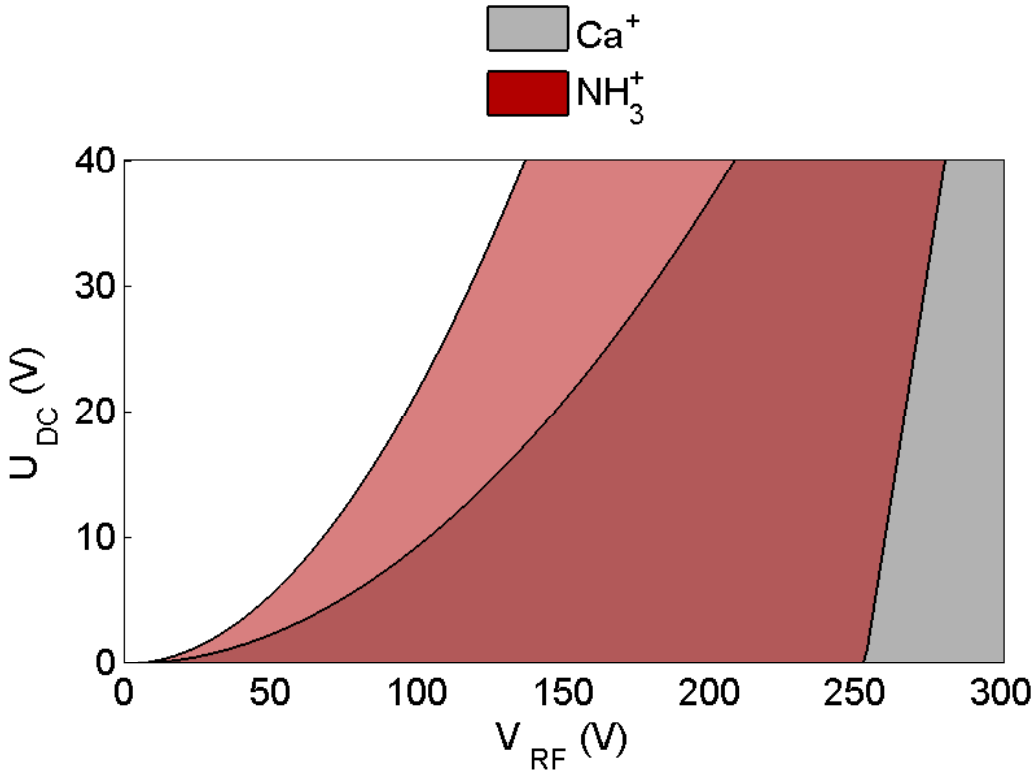

Figure 2.5: Stability diagram as a function of V_{RF} and U_{end} in the cryogenic ion trap at $\Omega_{\mathrm{RF}} = 2\pi \times 2.55$ MHz. The stability zone, i.e. where the requirements for stability are satisfied, is in grey for Ca^+ and in red for $NH_3{}^+$. Regions where both ions can be trapped are indicated by the darker red overlap area. Only the experimentally accessible region is shown here.

2.2 Laser cooling

The confined atomic Ca^+ are initially translationally hot, with kinetic energy arising from both their micromotion and their secular motion. The secular motion (as noted in section 2.1.1) can be by slowed down using lasers. This technique is called "laser-cooling" or Doppler cooling—as it uses the principle of the Doppler

effect [2].

The absorption (or emission) of a photon is associated with a change in the ion's momentum, according to the laws of conservation of momentum. Laser cooling methods employ a laser at an operating wavelength close to resonance with an electronic transition in the target ion as the source of photons. By slightly detuning the laser to a higher wavelength than the resonant wavelength (red-shifting), due to the Doppler effect, only ions travelling towards the laser propagation direction will encounter it with the right absorption frequency. The transfer of momentum subsequently induces a slight decreases in the particle's velocity. The excited ion will subsequently spontaneously emit a photon, with this photon emitted in a random direction. This cycle of absorption and emission is repeated many times, leading to an overall decrease in the particle's velocity, and therefore a lower translational temperature. One cooling laser is sufficient to cool the motion in all directions for large ensembles of ions; the Coulombic coupling between the ions helps to thermalize all translational degrees of freedom [10,35,97]. The lowest translational temperature that can be reached by laser cooling alone, the Doppler limit T_D, is determined by the expression

$$T_D = \frac{\hbar\Gamma}{2k_B} \tag{2.15}$$

where Γ is the natural linewidth of the cooling transition.

The cooling scheme for Ca^+ was first described by Ritter et al. [98] and is illustrated in Figure 2.6. The primary cooling transition used is the (4s) $^2S_{1/2}$ to (4p) $^2P_{1/2}$ transition, at 397 nm, that corresponds to a Doppler limit of $T_D = 0.5\,\mathrm{mK}$. The

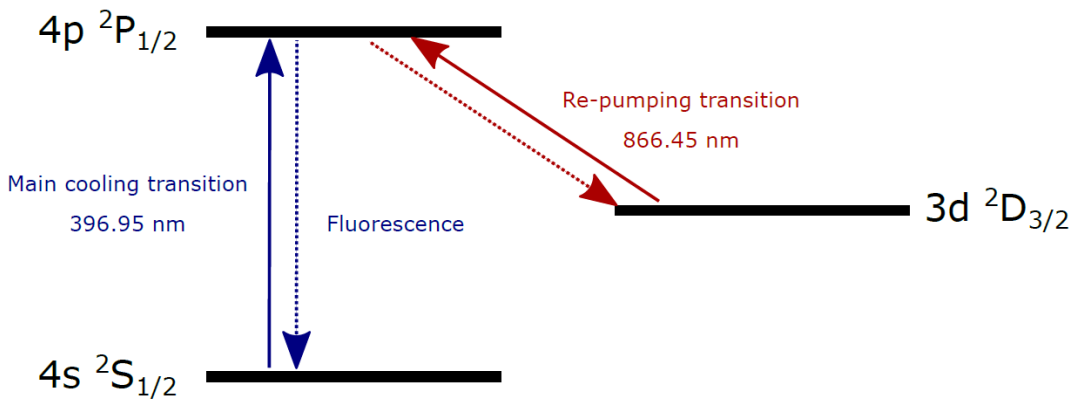

Figure 2.6: Energy levels of Ca^+ relevant for the laser cooling scheme. The laser induced electronic transitions are shown, at 397 nm and 866 nm, respectively. The transition from the ground (4s) $^2S_{1/2}$ to the (3d) $^2D_{3/2}$ state is an electric-dipole forbidden transition. Reproduced from Andriana Tsikritea's thesis [97].

ions in this excited state then either decay to the ground state (4s) $^2S_{1/2}$, or to the metastable state (3d) $^2D_{3/2}$ with a 12:1 ratio [99]. The lifetime of the ions in the excited 4p state is approximately 7 ns; ions in the metastable state decay to the ground state very slowly because the electric-dipole transition is forbidden. This means that over a few cooling cycles, population will build up in the metastable state, preventing an efficient laser cooling process. By introducing a second diode laser at 866 nm, it is possible to re-pump the particles in the 3d metastable state back to the 4p excited state, where they can decay to the 4s ground state, effectively closing the cooling cycle and ensuring that the laser cooling process is efficient.

As noted in the preceding paragraph, an efficient laser cooling scheme needs to have a closed cycle. This can more easily be achieved using particles with a simple energy-level structure. For that reason, singly charged alkaline earth ions (such as

Ca^+, used in this work) have been widely used. It is also for this reason that laser cooling of molecular species is very challenging—with many more internal energy levels needing to be considered and addressed to achieve a "closed" cycle than with atomic species.

2.3 Coulomb crystals

Trapped ions that have sufficiently low kinetic energies can undergo a phase transition to adopt a regular structure, known as a Coulomb crystal [2,10,35,100]. When the Coulombic repulsion between adjacent ions is greater than their kinetic energy, it balances with the forces of the trapping fields. Coulomb crystals can be considered as strongly coupled non-neutral plasmas, adopting a crystal-like structure when the plasma coupling parameter $\gamma > 150$, with γ defined as

$$\gamma = \frac{E_{\text{pot}}}{E_{\text{kin}}} = \frac{Q^2}{4\pi\epsilon_0\alpha_{\text{WS}}k_{\text{B}}T} \tag{2.16}$$

where α_{WS} is the Wigner-Seitz radius, a measure of the distance between ions, obtained from their density; ϵ_0 is the vacuum permittivity; k_{B} is the Boltzmann constant; T is the temperature. In a Coulomb crystal with a density of around $1 \times 10^8\,\text{ions/cm}^3$, the distance between neighbouring ions is around $10 - 20$ µm [2,101]. Because the ions are tightly localized and emit laser-induced fluorescence, the average position of individual ions, corresponding to the potential minima where the ions are likely to be found, can be observed with a camera (see Figure 2.7). This allow us to monitor the fluorescence over time to study reactions.

2.3.1 Sympathetic cooling

Laser cooling schemes are only applicable to specific ions, and therefore (as there are not many ionic species that are amenable to laser cooling) there are a limited number of reactions of interest that could be studied with laser-cooled ions. In order to obtain a larger range of cold atomic and molecular ions, we can take advantage of what is called "sympathetic" cooling.

While most ions cannot be laser cooled, it is often possible to adopt trapping parameters that will allow these ions to be co-trapped alongside the laser-cooled species. Thanks to elastic scattering with the laser-cooled species, the non-laser-cooled species can transfer kinetic energy to the laser-cooled ions, and that energy is then dissipated through the laser-cooling process. This allows for co-trapped species to be effectively cooled down and incorporated into the Coulomb crystal. This process of sympathetic cooling is most efficient for ions with a mass-to-charge ratio that is similar to the laser-cooled species, ideally with a ratio between 0.4 and 2.5 [2]. By taking advantage of sympathetic cooling, it is possible to obtain a range of bi- and multi-component Coulomb crystals, and to therefore study a wide range of ion–neutral reaction processes.

In multi-component Coulomb crystals, species with the lowest mass-to-charge ratio will reside in the centre of the trap, with heavier species positioned outside of these lighter ions, as the pseudopotential equation depends on the the $1/m$ term. The sympathetically cooled species do not fluorescence and appear dark on camera images of the Coulomb crystal. The change that they induce in the fluorescence pat-

tern of the laser-cooled ions is how we are monitoring reactions in the first instance, as set out below.

2.4 Reactions studied using Coulomb crystals

Coulomb crystals have been successfully used in different ways to obtain information on reactions. I will give here two examples of reactions studied using Coulomb crystals, where reaction rate coefficients (in the first example) and branching ratios (in the second) were ascertained.

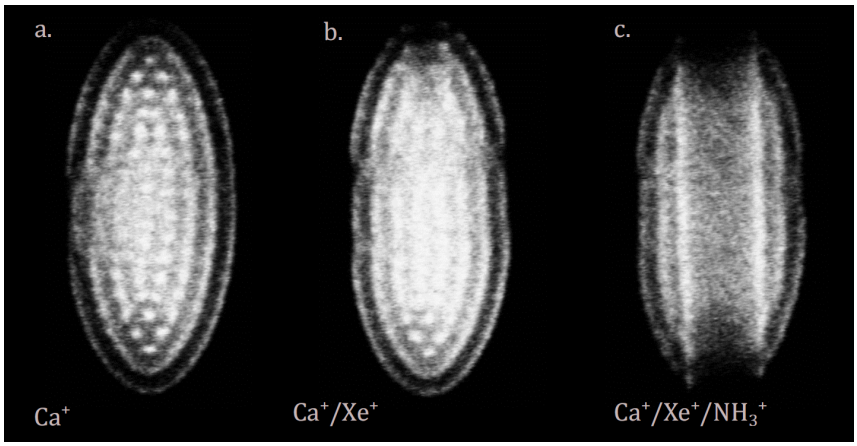

Figure 2.7: Images of Coulomb crystals taken with a CCD camera, of the central plane of the crystals, at selected times during a reaction. a) Lattice-like structure of a Ca^+ Coulomb crystal with the average position of individual ions evident. The Coulomb crystal in b) is bi-component, with sympathetically cooled heavier Xe^+ located on the outside of the fluorescent Ca^+, as can be seen by the flattened vertical sides of the Ca^+ framework. In c), the lighter $NH_3{}^+$ product ions are located in the centre of the crystal image, forming a dark core. Reproduced from Petralia, L.S. et al. Nat. Commun. 11, 173 (2020) [102].

Petralia et al. [102] compared the charge transfer reactions of Xe^+ with NH_3

and ND_3. They unexpectedly observed that the reaction between Xe^+ and NH_3 proceeded slower than the reaction between Xe^+ and ND_3, reporting a strong inverse kinetic isotope effect (see Figure 2.8). The progress of the charge transfer reaction was monitored by looking at the impact of the non-fluorescing reactants and products on the locations of the fluorescent Ca^+ ions within the Coulomb crystal over the reaction time (see Figure 2.7).

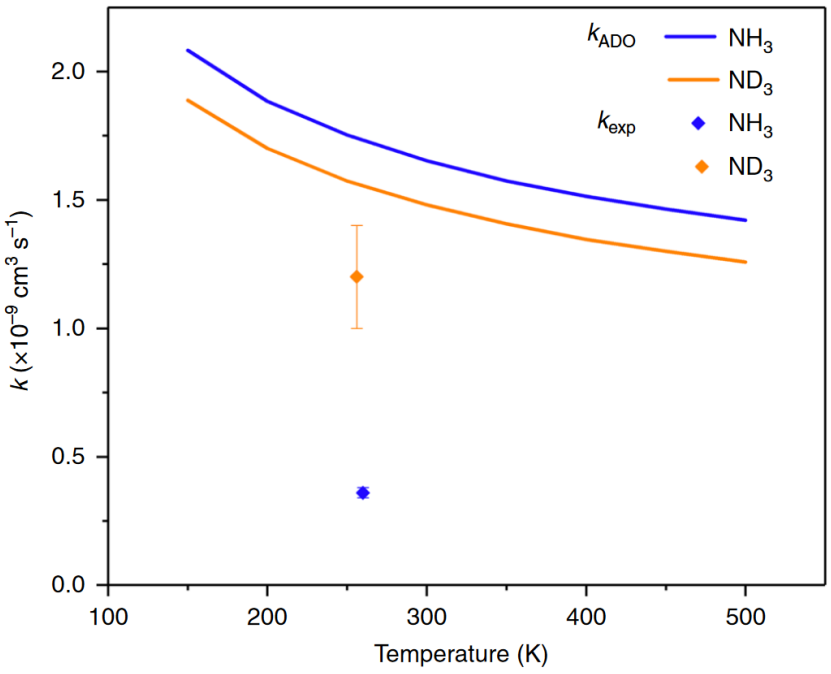

Figure 2.8: Comparison between charge transfer rate coefficients for $Xe^+ + NH_3$ (blue) and $Xe^+ + ND_3$ (orange) reactions obtained experimentally (points) and by ADO capture model theory (lines). Reproduced from Petralia, L.S. et al., Nat. Commun. 11, 173 (2020) [102].

After forming a Ca^+ Coulomb crystal in the reaction chamber, Xe was leaked and ionised at the trap centre using a 2+1 REMPI scheme. Because Xe^+ ions are

heavier than Ca^+, they form an outer shell of the Coulomb crystal, and are cooled through sympathetic cooling. The Xe^+ ions do not fluoresce, but their impact on the shape of the crystal is visible, with an elongation and "flattening" of the sides of the fluorescing Ca^+ lattice positions in Figure 2.7 (comparing the first two experimental images).

When a beam of ammonia is admitted to the trap, the charge transfer reaction takes place, producing $NH_3{}^+$ product ions. The $NH_3{}^+$ ions are subsequently trapped and, because they are lighter than Ca^+, are located at the center of the ion trap, that is also the center of the Coulomb crystal. Doing so, they push the Ca^+ ions further out and induce a rearrangement of the ions in the Coulomb crystal. The absence of fluorescence (arising from the relocation of Ca^+ away from the trap centre) appears as a "dark core" in the crystal. The dark core, composed of product ions, expands as the reaction proceeds. By recording this change over time, one can then extract the reaction rate coefficient by matching experimental images with simulated images—establishing the number of each type of ion (reactant/product/Ca^+) in the crystal as a function of time. The combination of time-of-flight mass spectrometer (ToF-MS) detection capabilities with the fluorescence images is essential to ensure that $NH_3{}^+$ ions are the only ionic product from that reaction and are the only contributor to the dark core observed.

Other groups are using ToF mass spectrometry directly to obtain information about a reaction. This is because, in more complex reaction systems where there might be multiple reaction channels, the fluorescence images do not contain

sufficient information by themselves; multiple species could be giving rise to a dark core observed in the images, and these species cannot be distinguished by images of the fluorescing ions. Krohn et al. [103] studied the reaction of CH_3CN with CCl^+ within a Coulomb crystal. The CCl^+ ions were sympathetically cooled by the Coulomb crystal of Ca^+ formed in their linear Paul trap. Although they do monitor the reaction through the fluorescence changes using a CCD camera, they obtain reaction rate coefficients and branching ratios using their time-of-flight mass spectrometry data.

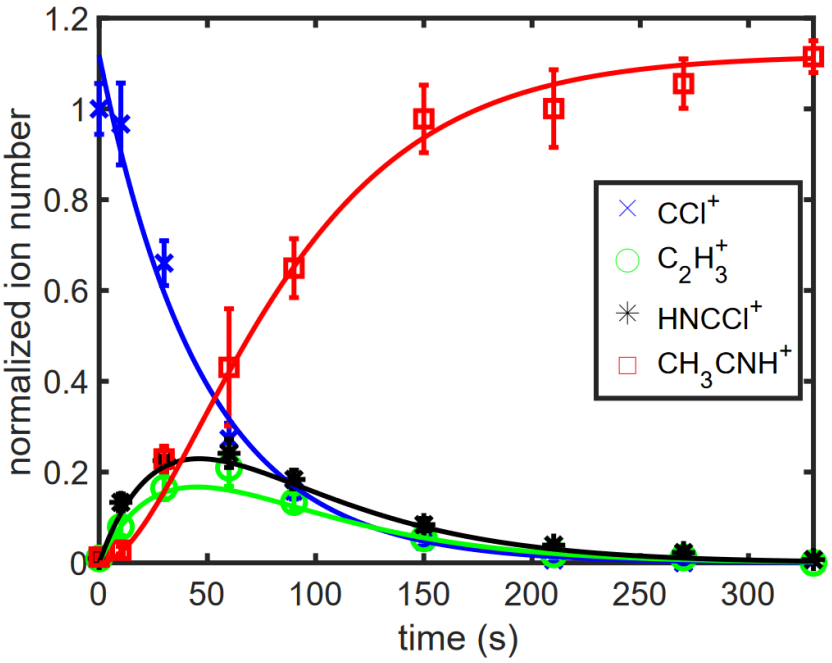

Figure 2.9: Reaction progress data (points) and fits (curves) for the pseudo-first order reaction of $CCl^+ + CH_3CN$. CCl^+ (blue) reacts with excess CH_3CN resulting in first order products $C_2H_3{}^+$ (green) and $HNCCl^+$ (black). Each of these primary products then reacts with excess CH_3CN to form CH_3CNH^+ (red). Reprinted from J. Chem. Phys. 154, 074305 (2021) [103], with the permission of AIP Publishing.

After the CCl^+ ions are sympathetically cooled by the Ca^+ ions, neutral CH_3CN is leaked into the chamber. The content of the trap is then ejected towards the detector at a selected reaction time. By repeating the process at different times from the moment the CH_3CN is leaked into the chamber, they obtained the average number of reactants and product ions as a function of the reaction time (Figure 2.9). From this, they were able to obtain the rate coefficients for the different reaction processes. They additionally obtained the branching ratios between the primary ionic products $C_2H_3^+$ and $HNCCl^+$ experimentally, and were able to obtain the same results through calculations.

The cryogenic ion trap depicted in this work combines the Coulomb crystal imaging approach with ToF mass spectrometry detection capabilities in a low-temperature environment. This approach will allow us to have a full picture of a reaction, and the flexibility to study a range of reaction processes—with multiple product channels and internally cold molecular ions as reactants.

Chapter 3

Design of the cryogenic ion trap apparatus

Parts of this chapter are based on work that has previously been published in a Review of Scientific Instruments article by Miossec et al. (2022) [74].

3.1 Design of the CryPTEx apparatus

As set out in section 1.2.2, the cryogenic Paul trap presented in this thesis has been influenced by the design of the CryPTEx apparatus developed at the Max Planck institute für Kernphysik (MPIK) in Heidelberg [76]. Since we started working on the cryogenic ion trap design, two more set-ups based on the first CryPTEx have also been developed: the CryPTEx-PTB in 2019 [80] and CryPTEx-SC in 2021 [81].

All of these cryogenic ion trap apparatus have as their primary objective to minimize BBR and therefore reach low temperatures at the ion trap region. All of the apparatus have been built with the ion trap nested inside multiple shielding stages, as can be observed in Figures 3.1, 3.2, 3.3. Each stage is progressively colder, reaching temperatures $< 5\,\mathrm{K}$ at the innermost region in all three CryPTEx apparatus. To reach such temperatures, the openings in the shielding of each stage are all very small, to limit the solid angle of BBR coming from room temperature

surfaces. As can be seen in Figures 3.1, 3.2, 3.3, the access apertures to the center of the ion traps incorporate a narrow tunnel with a small solid angle [76].

While all CryPTEx apparatus use stainless-steel spokes to connect each stage, suspending the shielding for each stage within one another to minimise heat conductivity between stages (see Figure 3.1, 3.2, 3.3), we chose a different approach. As will be detailed later in this chapter, we are using a Heim column (composed of three nested tubes) to support each stage independently and limit heat conductivity. This reduces the complexity of the nested stages and also provides more flexibility in how we use the ion trap.

The original CryPTEx experiment was designed primarily for the study of highly charged ions. Our goals are somewhat different: we set out to design a cryogenic ion trap for the study of cold and controlled ion–neutral reactions. While our design choices were, in some instances, influenced by the CryPTEx design—and by useful discussions with the research groups involved in the various CryPTEx projects—we also chose to approach some elements differently, to better suit our intended applications. In the following subsections, the design choices for our cryogenic ion trap are explained and discussed.

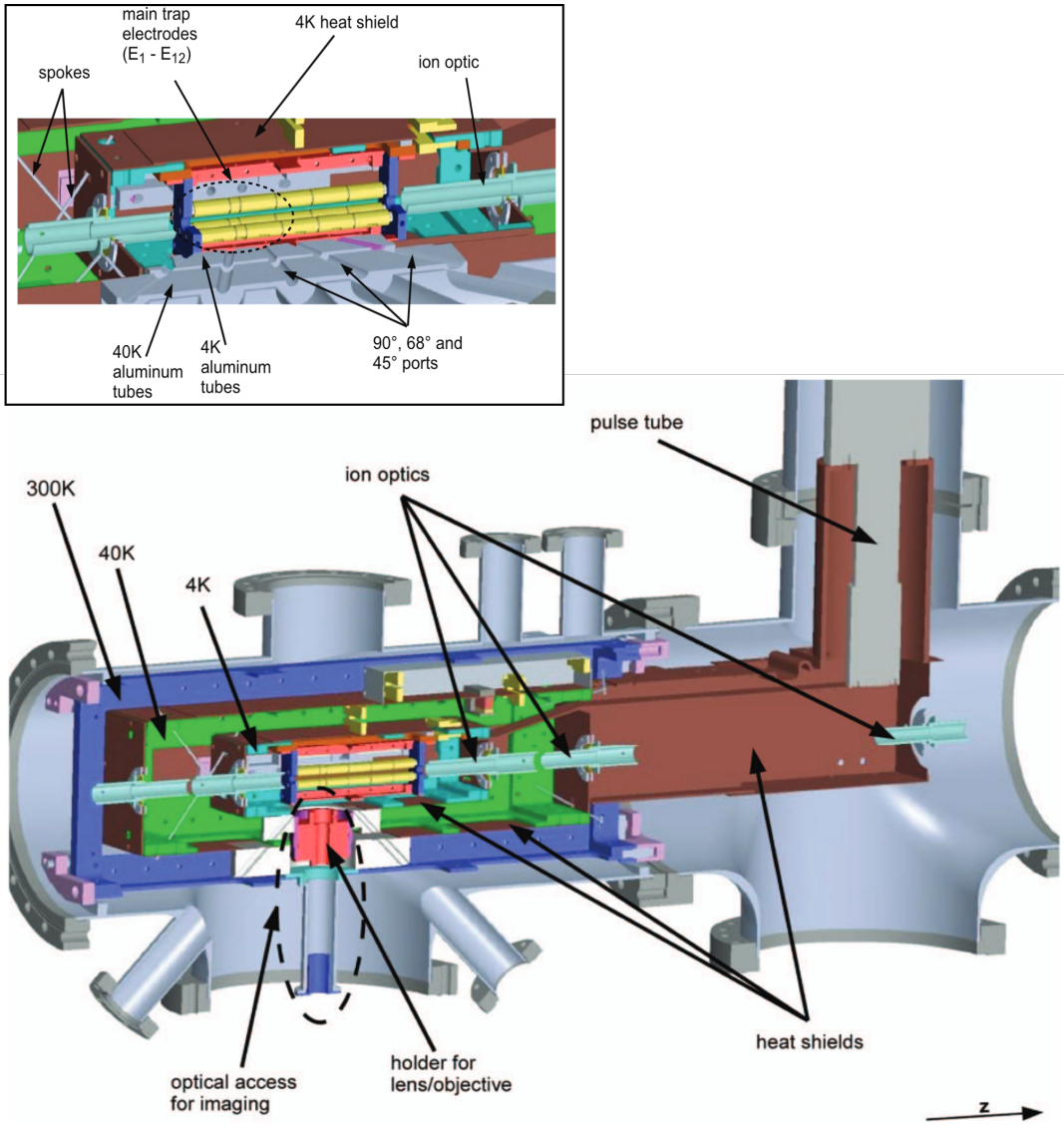

Figure 3.1: Cross section view of the original CryPTEx apparatus, with the different temperature stages identified in different colours and labelled. The inset shows a close up view of the innermost stages and of the ion trap. The spokes that connect each temperature stages to each other are also visible on the left-hand side of the inset. Reproduced from Rev. Sci. Instrum. 83, 083115 (2012) [76].

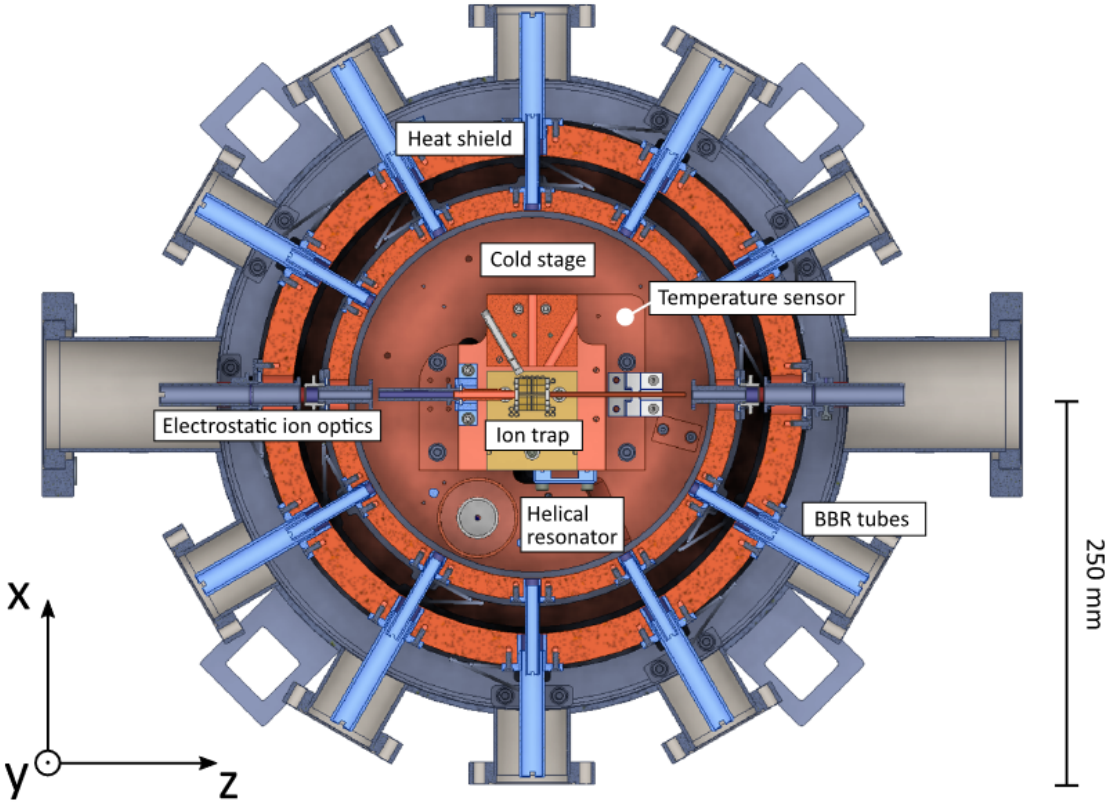

Figure 3.2: Top view cross section of the CryPTEx-PTB apparatus, with the different temperature stages identified in different colours and labelled. Reproduced from Rev. Sci. Instrum. 90, 073201 (2019) [80].

3.2 Design

3.2.1 Requirements of the apparatus

Optical access to the trap center is required in order to form Coulomb crystals and to monitor reactions. Lasers need to pass along the trap axis, and a camera needs to monitor the fluorescence of the laser-cooled ions in the trap center. Line-of-sight access to the trap centre is also required for the calcium beam, for the neutral

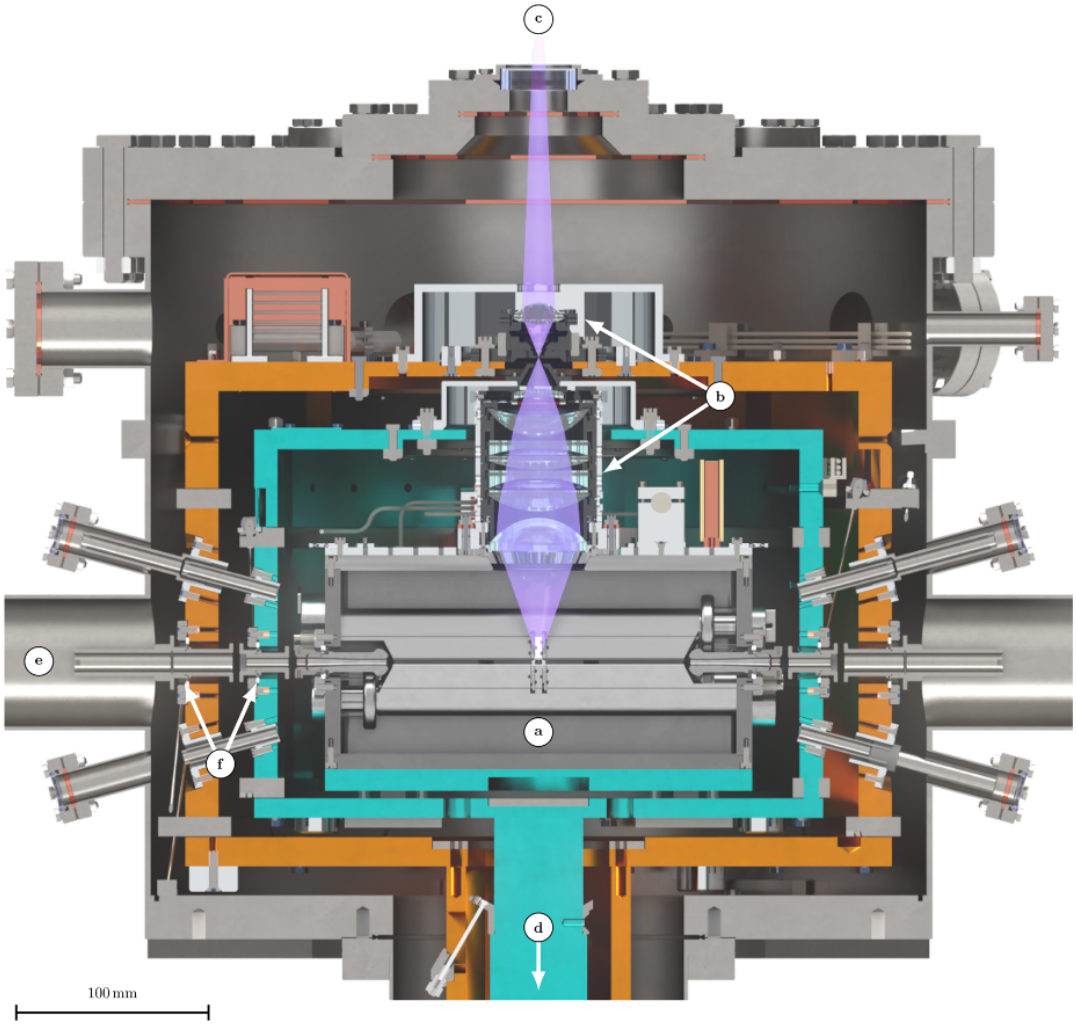

Figure 3.3: Cross section view of the CryPTEx-SC apparatus, with the different temperature stages identified in different colours. The first temperature stage is depicted in orange and reaches 69 K, and the second temperature stage is depicted in cyan and reaches 4 K. a) Superconducting cavity, b) imaging system, c) detection system, d) connection to the cryogenic supply, e) port to the HCI transfer beamline, and f) electrostatic lenses. Reproduced from Rev. Sci. Instrum. 92, 083203 (2021) [81].

beam, and for the time-of-fight detection of the ions. Finally, as explained earlier, we are aiming to reach temperatures below 10 K at the ion trap. For that, the ion trap is connected to a cryocooler, and surrounded by shielding to limit the effect of BBR on trapped ions. The design of the apparatus is centered on this capacity to reach cryogenic temperatures at the ion trap, and is achieved by minimising the thermal contact between the components exposed to the ion trap and parts of the apparatus closer to room temperature conditions. The design selected—where exposure to BBR is minimised whilst maintaining the necessary optical access to the trap centre—is described in the following sections of this chapter.

3.2.2 Ion trap

The ion trap is based on a conventional linear Paul trap design (detailed in section 2.1.1), comprising of four parallel cylindrical electrodes, each separated into three segments (see Figure 3.4). The rods have a diameter of 8 mm; the central segment of the rods is 5.4 mm long and separated by 0.2 mm from the end segments that are 20 mm long. Given the need to reach temperatures below 10 K, the ion trap is surrounded by cryogenic shielding.

To ensure the shielding encloses the trap region as tightly possible, and to achieve good contact between the trap rods and the second stage of the cryocooler, the rods are cut in half along the trapping axis and mounted on the shielding. Both the rods and the shielding are machined from oxygen-free, high-conductivity (OFHC, 99.99% purity) copper to ensure maximum thermal conductivity between the cold head and the trapping region. Each rod segment is electrically isolated from the

shielding case by thin layers of Shapal ceramic (0.6 mm); the screws holding them in place are also electrically insulated by ceramic washers with a favourable thermal expansion coefficient, good thermal conductivity, and with a sufficiently large dielectric constant. They are also isolated from one another, to allow independent voltages to be applied to each electrode.

The shielding surrounding the trap is octagonal and near-symmetric in shape. Finite-element method simulations have been carried out by a previous postdoctoral in the group to establish if any major distortion of trapping fields might be introduced by the design of the trap and shielding (see Figure 3.4). These simulations confirmed that no significant distortions are expected to arise from the shielding around the ion trap region.

As can be seen in Figure 3.4, there are openings on six faces of the shielding surrounding the ion trap. The openings on the trap shielding between the rods (i.e., perpendicular to the trap axis) serve several purposes: they allow for the admission of neutral Ca atoms (for the formation of Ca^+ ions), for the introduction of a 250 µm diameter optical fiber tip for alignment purposes, for the introduction of reactant species, for Coulomb crystal imaging, and for the extraction of ions into a time-of-flight tube for the recording of mass spectra (all detailed in Figure 3.5). The two openings in the shielding along the trap axis provide laser access to the trap centre. The shielding is thus designed to minimise the admission of 300 K BBR to the central trap region whilst still providing the necessary access to the trap for reaction studies to occur.

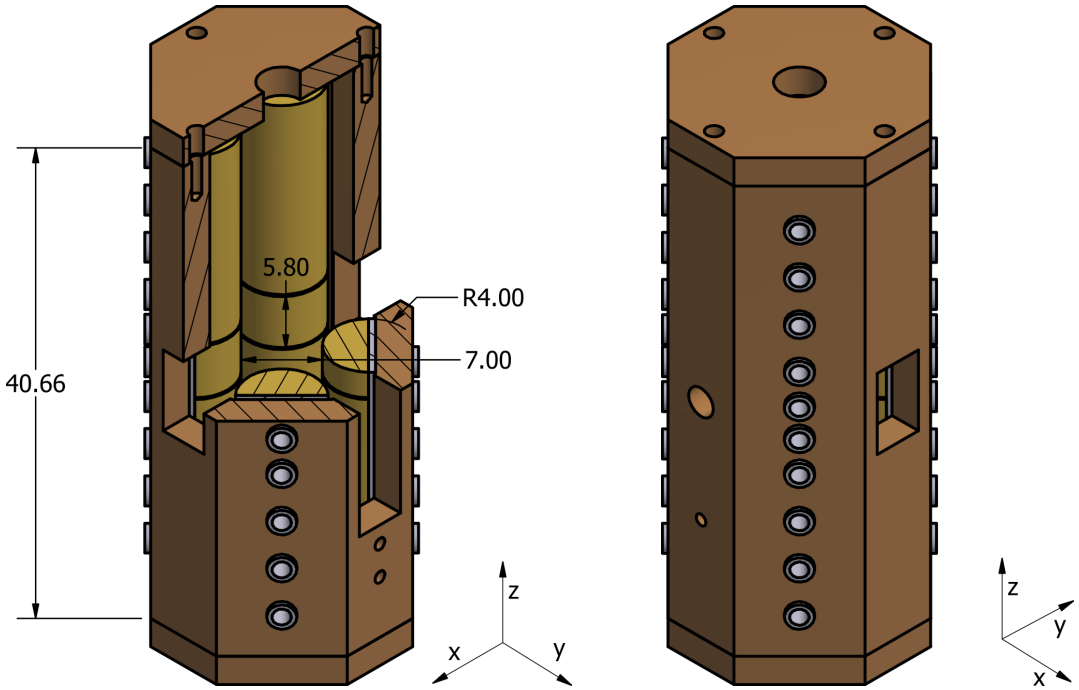

Figure 3.4: Schematic illustrations of the cryogenic ion trap and its shielding case, from two viewpoints. The cut view (left) shows the cut circular rods (yellow) and their radius. The distance between two opposing rods, i.e. $2r_0$, and the distance between the endcaps, i.e. $2z_0$, are also shown. The view of the casing (right) shows three of the openings in the case (brown) to the center of the ion trap: the circular opening on the z axis, for the lasers (the same is at the bottom of the case), the circular opening in the $-y$ axis where the radical beam will enter the trap, and the rectangular opening on the x axis where the calcium beam is entering the trap.

3.2.3 Cryogenic system

The innermost region of the chamber—housing the ion trap and off-axis parabolic (OAP) mirror—is designed to reach temperatures $\leq 10\,\mathrm{K}$. To reach such low temperatures, we used a two-stage pulse tube cryocooler (4 K Pulse Tube Cryocooler from Sumitomo Heavy Industries, Ltd). This cryocooler consists of a compressor

connected to a pulse tube that feeds helium to a two-stage cold head. The cryocooler specifications indicate that temperatures as low as 4.2 K (at the second stage) and 45 K (at the first stage) can be reached, under suitable conditions. As noted in section 3.2.2, the ion trap is connected to the second (coldest) stage of the cryocooler, with shielding in place to minimise exposure to higher temperature environments. All of the ion trap wires and sensor wires are anchored to the shielding or the cold head, to avoid placing additional heat load on the ion trap region.

The thermal contact between the second stage of the cold head and the shielding is achieved through the use of a custom-made copper braid (schematised in Figure 3.6). The flat surface of the copper braid at one end is fixed under the second stage of the cold head, and the other end is fixed at the back of the shielding of the mirror. As far as possible, all components in this coldest second stage are made of high-purity copper. Using copper ensures that there is high thermal conductivity whilst also ensuring that the components behave in the same way as the temperature is reduced, to ensure mechanical contact is maintained.

Surrounding the coldest (second) stage, additional shielding is connected to the first stage of the cryocooler. The first-stage shielding has been designed in two parts, such that the front can be removed to provide access to the innermost region. Openings in the outer shielding are present for the same reasons as in the second-stage shielding: to provide direct access to the center of the trap. The first stage of the cryocooler is attached to a stainless steel structure that surrounds

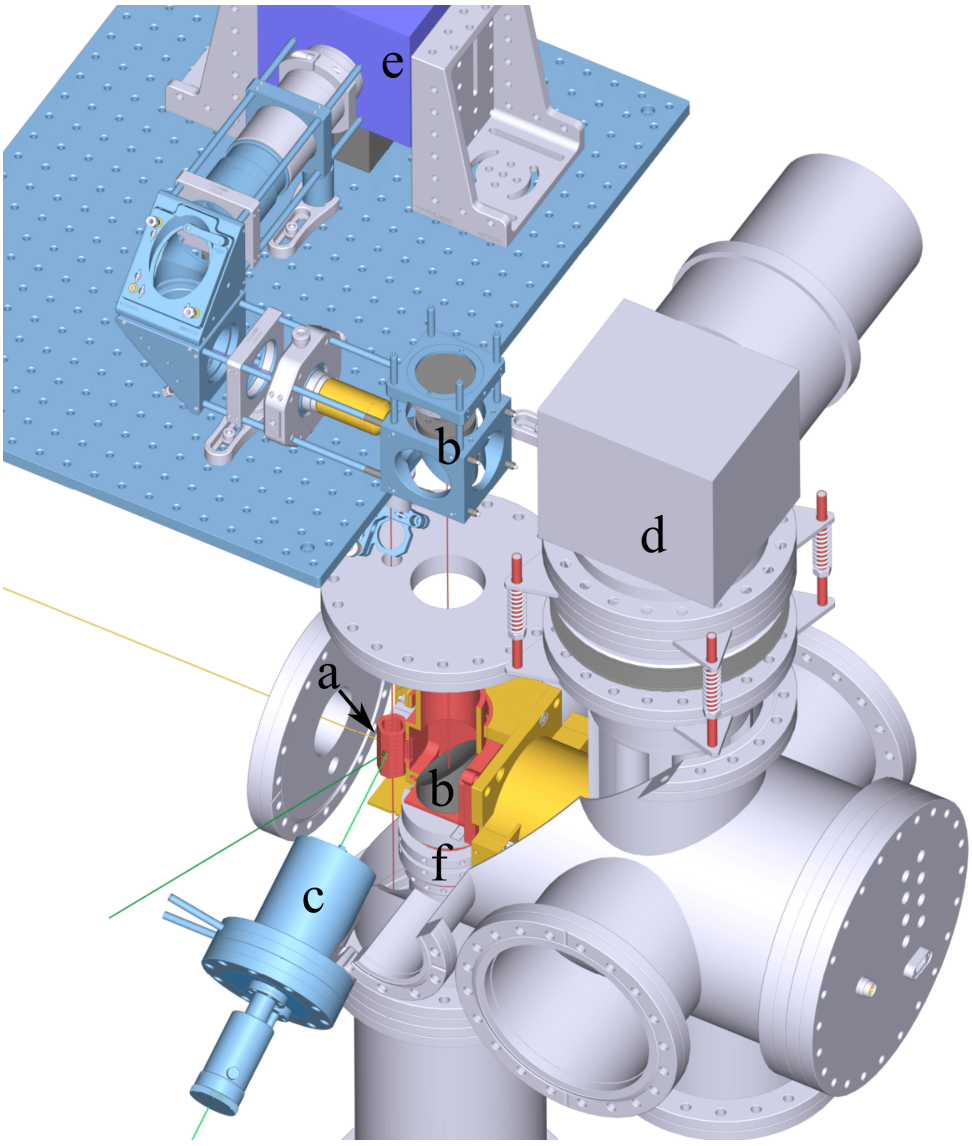

Figure 3.5: Schematic illustration of the cryogenic ion trap chamber and imaging system. The first temperature stage is depicted in yellow, and the second temperature stage in red. a) Ion trap, b) both OAP mirrors, c) calcium oven, d) cold head, e) electron multiplying charge-coupled device (EM-CCD) camera after the imaging relay system, f) the Heim column. Reproduced from C. Miossec et al., Rev. Sci. Instrum., 93 (3): 033201 (2022) [74].

the second stage of the cold head (see Figure 3.6). In the same way as has been described above for the second stage, the shielding connected to the first stage of the cold head is thermally connected to the first stage shielding surrounding the second stage by copper braids fitted on the side of both parts of the shielding (see Figure 3.6).

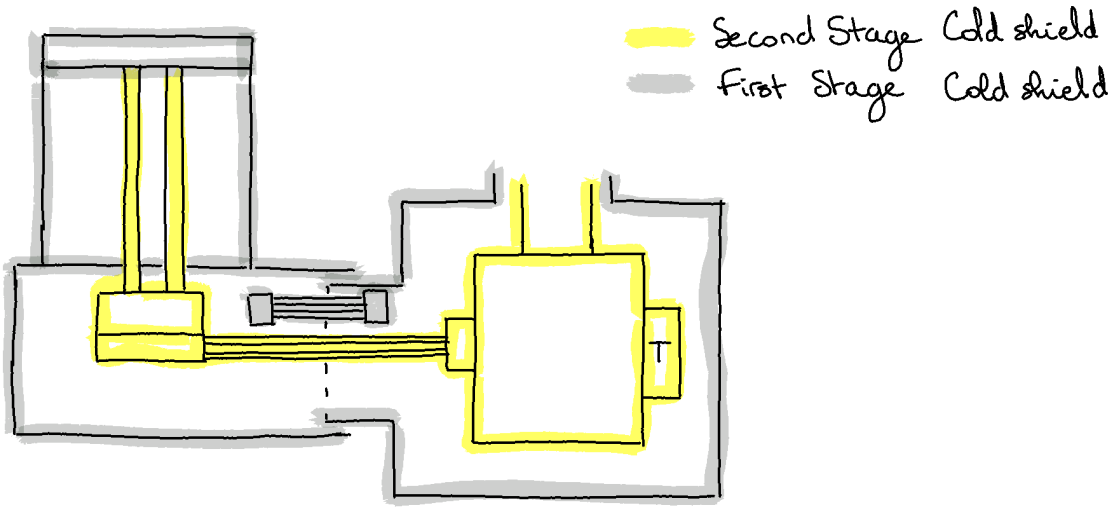

Figure 3.6: Schematic of the two stages cold shield from the cryocooler cold head to the ion trap. The cold head is schematised on the left; the ion trap is schematised on the right by the T. The first stage of the cold head is connected to the first stage shielding surrounding the ion trap through copper braids, and depicted in grey. The second stage of the cold head, the coldest, depicted in yellow, is connected to the second stage shielding, to which the ion trap is connected.

Figure 3.5 shows several details of the apparatus. The ion trap (shown in red) is nested inside several layers of shielding. Both the ion trap (within the ion trap holder) and an OAP mirror are encased within the second cold shield, also shown in red. This second cold shield is connected to the second stage of the cryocooler.

The first cold shield, in yellow, is built around the second cold shield and connects to the first stage of the cryocooler. Calcium atoms are generated by the calcium oven, shown in blue on the lower left hand side of the figure. Fluorescence from the laser cooled ions, and images of the back-lit Ronchi ruling (discussed further in Chapter 4), are directed by the first OAP mirror (shown in dark grey and to the immediate right of the ion trap, within the red shielding region) to the second OAP mirror, situated outside the vacuum chamber (held in place by a blue mount), and through the rest of the imaging relay system on the upper (blue) breadboard.

The pathway followed by the ionisation and laser cooling beams is illustrated by the thin (left) red line passing through the centre of the ion trap. The imaging pathway is illustrated by the parallel (right) thin red line, with the images relayed out of the chamber by an OAP mirror. The passage of Ca atoms from the oven to the trap centre is illustrated in green. At the trap centre, Ca atoms are non-resonantly ionised by a laser (at 355 nm), forming Ca^+. Additional reactants can be introduced along the second (off-axis) green pathway illustrated. Slow-moving neutral reactants will be introduced along the yellow pathway, where a Zeeman decelerator and magnetic guide will be connected. All other chamber components, including the cold head (on the top right hand side of the figure) and the Heim column (bottom central region), are depicted in grey. Note that the ToF detection pathway cannot be seen in this schematic drawing, as it is directed into the page.

3.2.4 Heim column

The ion trap and its shielding rest on a low-heat-leakage temperature-stabilised support, known as a Heim column. Theorised by Heim in 1973 [104], it is composed of two titanium tubes and an aluminium tube, nested inside one another. Each of the tubes is only connected to another tube at one end (see Figure 3.7), with a vacuum gap between the walls. They are constructed in such a way that any thermal shrinkage (when the chamber is cooled down) is compensated for. This limits the need for extensive optical realignment whenever the chamber is cooled down or warmed up. If a small alignment adjustment is needed, the Heim column (and the trap) can be moved with respect to the main vacuum chamber by adjusting the hexapod below the column. The outermost section of the Heim column is mounted onto the hexapod—kept at room temperature—via a cylindrical holder, shown in Figure 3.7. The second tube is made of aluminium and supports the first stage shielding that reaches temperatures around 60 K, depicted in purple in Figure 3.7. The innermost tube of the Heim column supports the second stage cold shield, and therefore the ion trap connected to it, reaching temperatures close to 10 K when the cryocooler is on (shown in blue in Figure 3.7). The hexapod is attached to a counterweight of 213.6 kg, to provide stability to the column and to anchor it to the ground.

3.2.5 Time-of-flight mass spectrometer

One of the objectives of this apparatus is to analyse products using ToF mass spectrometry. As stated in section 2.1.1, the oscillating voltages of the ion trap can be turned off and static ejection voltages applied to the rods, forming a

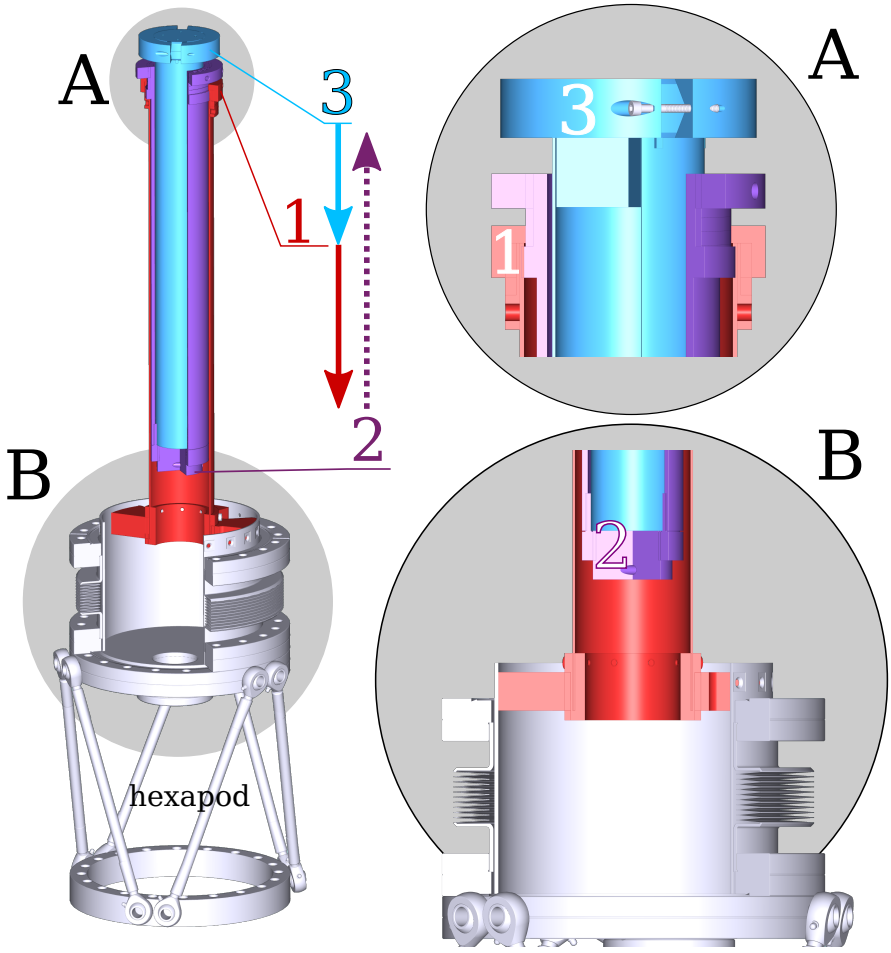

Figure 3.7: Cut views of the Heim column, with contraction directions indicated by arrows. The entire column, with the hexapod, are depicted on the left hand side of the figure, with two inset sections provided on the right hand side to show details of the connections within the Heim column. The three tubes are coloured red (outer, labelled 1), purple (middle, labelled 2), and blue (inner, labelled 3). Reproduced from C. Miossec et al., Rev. Sci. Instrum., 93 (3): 033201 (2022) [74].

repeller-extractor pair. The ions are ejected from the trap, accelerated (either by the repeller and extractor fields alone, or by the inclusion of additional ion optics), and ultimately pass into a free-flight tube. At the end of the flight tube is a microchannel plate (MCP) detector, where the ion signal can be recorded [105].

Initial designs include three ion optics attached to the second-stage shielding, with additional lenses outside the low-temperature region and attached to the first-stage shielding (see Figure 3.8). All ion optics are electrically isolated, enabling different voltages to be applied to each element to direct and accelerate the ions. ToF mass spectrometry is very useful for not only quantitative product detection, but also measurements of branching ratios and rate coefficients. Therefore, it is important to find the optimal set of voltages and parameters to maximise the detection efficiency and mass resolution of the detector. This work is currently being further developed by a new PhD student and a postdoctoral research associate in our group.

3.2.6 Calcium oven

The objective of the cryogenic ion trap is to study reactions within Coulomb crystals, with low ambient temperatures so that as much control as possible can be exerted over the reaction parameters. We choose to use Ca^+ for forming Coulomb crystals.

As such, we need a source of calcium. This source is provided by a commercial calcium oven. It is a small stainless steel tube filled with pure calcium. At both

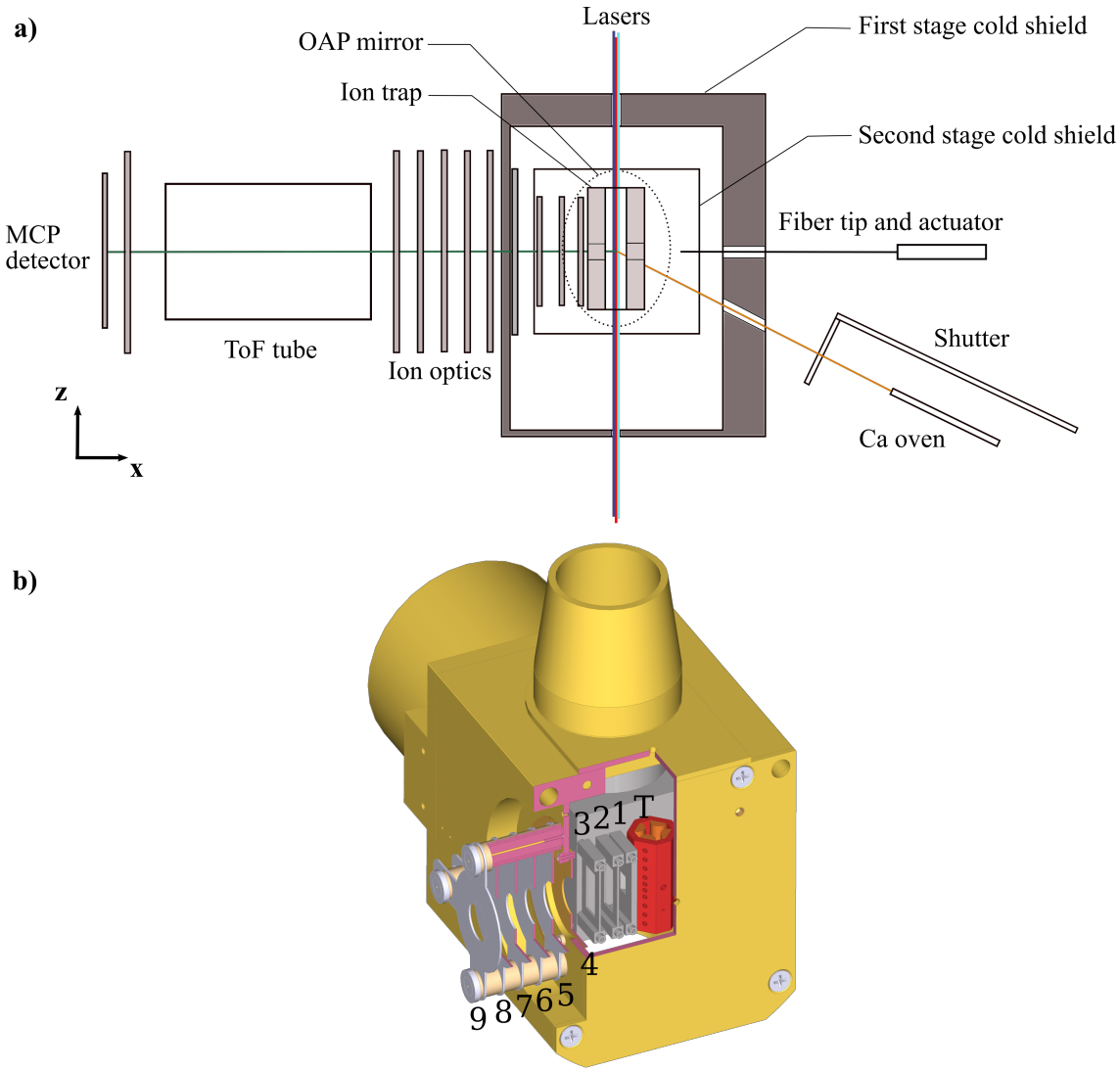

Figure 3.8: a) Schematic illustration of the cryogenic ion trap apparatus. The Ca atoms are coming from the Ca oven to the center of the ion trap (orange line), before being ionised by the Nd:YAG laser (cyan line) that goes through the ion trap. The red and blue diode lasers (red and blue lines) induce fluorescence of the Ca^+. The Ca^+ ions are then ejected from the ion trap towards the MCP detector (green line) through ion optics and a ToF tube. The outline of the OAP mirror placed inside the chamber is shown, but it is situated behind the ion trap. The radical beam is coming perpendicular to the image plane. b) Cut view of the innermost temperature stages of the chamber. The ion trap, labelled T, is visible at the center, with several ion optics on its left-hand side. Ions ejected from the trap are focused and accelerated by lenses 1–9 before entering the flight tube (not depicted) and reaching a MCP detector. The aperture of lens 1 is minimised to block BBR from entering the ion trap. Reproduced from C. Miossec et al., Rev. Sci. Instrum., 93 (3): 033201 (2022) [74].

ends of the tube are contact flaps used to connect the tube to electrical feedthrough wires and a power supply. By passing a current through the stainless steel tube, it is resistively heated, and the calcium inside reaches its sublimation temperature $\approx$ 551 K at 1×10^{-6} Pa [106]. The tube needs to be held perpendicular to the flange it is mounted on, and with the flaps electrically connected to the feedthroughs on the flange. However, as it is relatively close to the cryogenically cooled shielding, it is important to minimise the heat load emanating from the oven region.

To avoid placing too high a load on the cryocooler, and to minimise the deposition of calcium around the chamber, the calcium oven is surrounded by a water-cooled stainless steel enclosure. In the center of the oven enclosure, a hole allows the calcium beam to exit the oven region and enter the ion trap. Additional holes are present in the enclosure to allow for efficient pumping of the oven region.

To limit the amount of calcium sent to the center of the ion trap and unintentionally coating the rods, a shutter has been included in the design. The oven shutter is made from a simple rectangular piece of stainless steel held by a rod connected to an actuator situated outside of the chamber, on the calcium oven flange. By rotating the actuator (outside the vacuum), the shutter covers or uncovers the hole in the oven enclosure through which calcium is transmitted. During experiments, the actuator is closed when we warm up the calcium oven. Only when the pressure has stabilised will we open the shutter to allow calcium to the center of the trap, where it can be non-resonantly ionised.

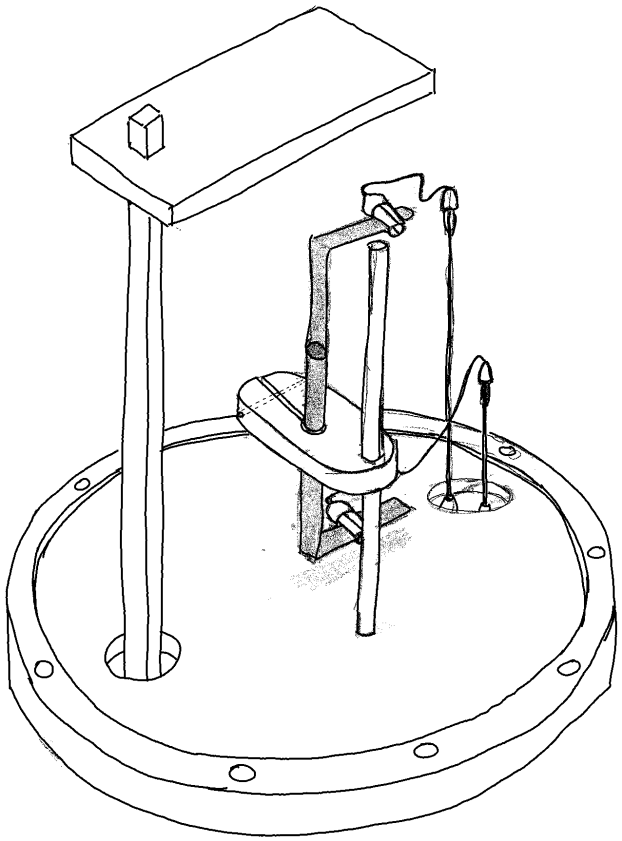

Figure 3.9: Drawing of the calcium oven (shaded) and its holding system. It is held in place by a clamp, with insulators electrically isolating the oven from the clamp and flange. The flaps at the two extremities of the calcium oven are connected to the two feedthrough pins, on the right. The rod on the left holds the shutter that allows the calcium beam to reach the ion trap, and is connected to a linear actuator. The OPEN or CLOSED position of the shutter is altered from the outside of the chamber by an actuator (not shown).

After the initial design was found to have some flaws (with the electrical connections and challenges in optimising the alignment of the oven two particular weak points), we opted to take inspiration from how the calcium oven is held in the other ion trap of our lab. The tube of the calcium oven is surrounded by an insulated ceramic tube and clamped to an additional rod on the flange (see Figure 3.9). The flaps are connected electrically with a pin at each end that is wired to the feedthrough on the flange. This design achieves the desired electrical contact between the feedthrough pins and the contact points on the oven. The optimised design also allows for the oven to be positioned such that the center of the beam is aligned with the hole in the oven enclosure and the acceptance region of the ion trap shielding (see Figure 3.10).

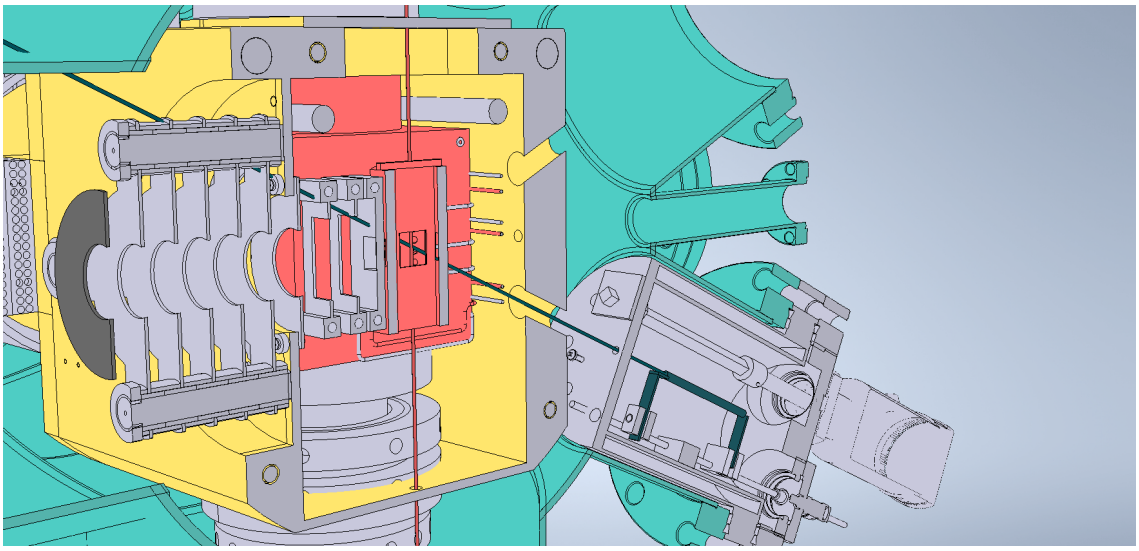

Figure 3.10: Computer-aided drawing CAD of the calcium oven in the cryogenic ion trap chamber. The calcium oven is depicted in dark green, and the ion trap in red. The path of calcium from the calcium oven to the ion trap is shown in dark green, passing through the first stage cold shield (yellow).

Chapter 4

Parabolic mirror-based optical system

Parts of this chapter are based on work that has previously been published in two *Review of Scientific Instruments* articles: Hedjuk et al. (2019) [107] and Miossec et al. (2020) [74].

4.1 Requirements for the optical system

In a Coulomb crystal, the laser-cooled ions are constantly fluorescing, and one can distinguish individual lattice positions within the crystal, with neighbouring ions typically separated by a distance of 10–20 µm [23]. This sets the mark for the resolution we want to achieve with the imaging system—to discern neighbouring ions, so that reactions occurring within crystals can be monitored over time.

In addition to resolution constraints are physical constraints. Other ion traps that use imaging of Coulomb crystals typically position a viewport close to the ion trap, so that a microscope objective can be placed outside the vacuum system achieving high-resolution images of crystals without the need to include any optical components inside the vacuum chamber [52]. Because of the cryogenic conditions required in our apparatus (described in Chapter 3), it is surrounded by a lot of

shielding. This drastically limits the amount of space around the ion trap and makes it physically challenging to position a viewport close to the trap centre. Another group directly introduced the first optical component, i.e. the objective, inside the chamber [67]. Because the chamber needs to be held under ultra high vacuum (UHV) to obtain stable Coulomb crystals, this approach is complicated. Most commercially available low-outgasing objectives compatible for UHV conditions are limited to working distances below 1 cm. To address the multiple issues of needing to have the first optical element located close to the trap centre for high-resolution imaging, whilst also adequately shielding the trap region and incorporating a number of other components that require optical access to the trap, we require: "a high numerical aperture, a long working distance, UHV and cryogenic compatibility, micrometer-range optical resolution, and cost-effectivity" [107].

To capture the maximum amount of fluorescence from the laser-cooled ions as possible, one needs to focus on maximizing the numerical aperture (NA) in order to optimise the signal-to-noise ratio. The components of the optical system have been carefully chosen to fit the requirements of the apparatus. For that reason, we made the choice of using a pair of OAP mirrors to achieve the best possible resolution whilst satisfying the practical requirements around the need for shielding and positioning the component inside the vacuum chamber.

4.2 Description of the system

4.2.1 Off-axis parabolic (OAP) mirrors

The optical system is based on a pair of OAP mirrors relaying the image of the fluorescing ions from the trap to a camera located outside the vacuum chamber. OAP mirrors have previously been successfully employed by Malone et al. for thermal imaging of shockwave experiments [108]. They compared the use of a pair of OAP mirrors with a standard lens imaging system (in the IR range in their case). In this earlier study, Malone and co-workers found that the OAP mirror-based imaging system outperformed a 'standard' optical system—collecting 29 times more light whilst maintaining the dimensions of the relayed image in the desired 1:1 ratio; the standard lens system produced a demagnified image.

They also demonstrated that, while using one OAP mirror and one lens is technically possible, the resulting image would be tilted and therefore would not be appropriate for our imaging purposes. Using two OAP mirrors as a pair offers an excellent solution to the practical limitations imposed by the cryogenic ion trap set-up, provided the pair of mirrors are properly aligned. Figure 4.1 illustrates how the image is decomposed by the first OAP mirror and recomposed by the second. Malone and co-workers noted the sensitivity of the resolution to the alignment of the pair of OAP mirrors: the rotation alignment tolerance of two 150-mm focal length and 90-degree off-axis parabolic mirrors is ± 2 degrees.

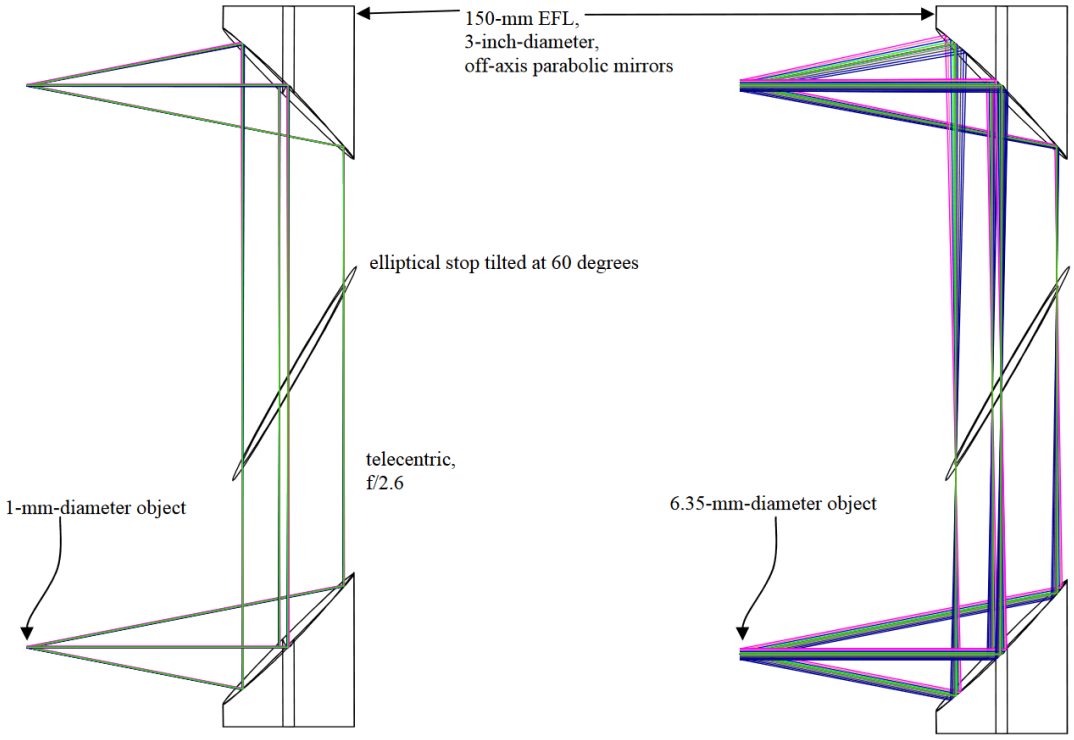

Figure 4.1: Schematic of a pair of off-axis parabolic mirrors used for 1:1 imaging. All mirrors are identical. Reproduced from R. M. Malone et al., Proc. SPIE 6288, Current Developments in Lens Design and Optical Engineering VII, 62880Z (2006) [108].

4.2.2 Design of our optical system

We selected commercial OAP mirrors from Edmunds optics, of 50.8 mm diameter, 50.8 mm effective focal length, a 90° angle offset and a roughness of 50 Å. The mirrors are coated by a UV Enhanced Aluminum protective layer with a reflectance wavelength range of 250–700 nm and a reflectance close to 90% at 397 nm—the wavelength of the fluorescing Ca^+. As explained in Hedjuk et al. [107], the large diameter of the mirrors is chosen to avoid geometric distortions. To illustrate this point, a former postdoctoral research associate in the group ran Zemax simulations

that showed that using a smaller mirror to image a 200 µm Coulomb crystal would cause distortions. The NA of the OAP mirror-based imaging system has been determined as 0.35 [107].

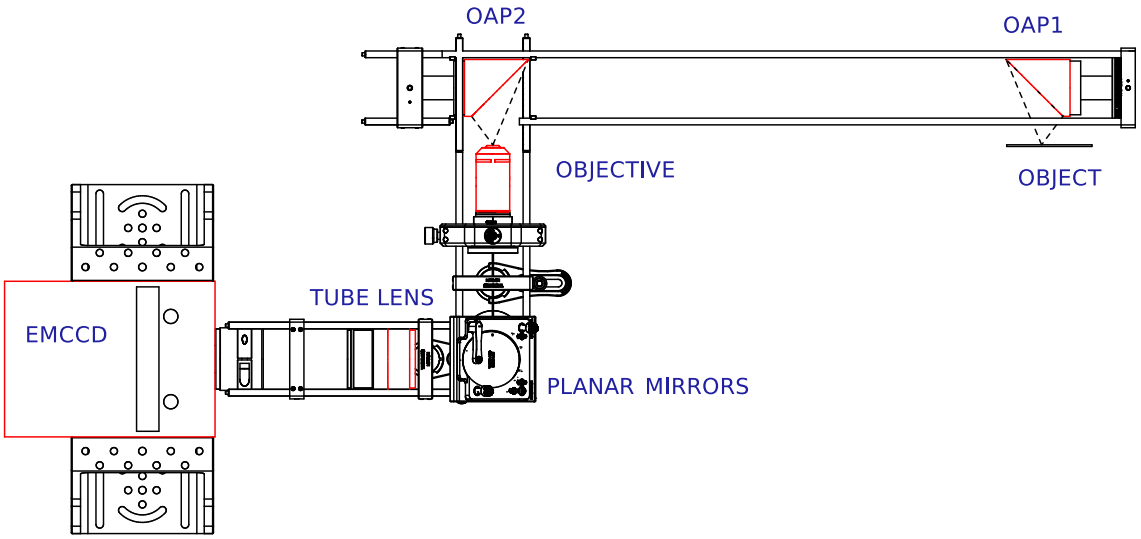

Figure 4.2: Top view of the optical setup. The key components are labeled. The two Off-Axis Parabolic mirrors (OAP1 and OAP2) are shown here in the same plane as the other optical components, i.e. the configuration when the optical system was tested outside of the chamber. In the chamber, both OAP1 and OAP2 components are directed perpendicular to the page. The dimensions and features of the optical accessories are taken from the manufacturer (Thorlabs). Reprinted from M. Hejduk et al., Rev. Sci. Instrum. 90 (12): 123701, (2019) [107], with the permission of AIP Publishing.

The first OAP mirror is situated inside the vacuum chamber with the distance between the center of the OAP mirror and the center of the ion trap corresponding to the effective focal length, i.e. 50.8 mm. A small opening in the shielding provides optical access to the center of the ion trap. The OAP mirror is surrounded by cryogenic shielding to avoid introducing 300 K BBR into the ion trap region.

However, the imaging of Coulomb crystals requires optical access to the trap centre. Therefore, both cryogenic stages have an opening above the mirror. As a concern that the mirror, so close to the ion trap, could direct a large portion of the 300 K BBR spectrum into the center of the ion trap, we integrated nested chimneys above the mirror, screwed to each stage. An additional removable plate sits below the chimney, on top of the first stage, to cover above the ion trap while allowing easy access to the trap center (shown in Figure 3.8).

The OAP mirror is mounted on a copper base by three screws, as this configuration was found to introduce minimal distortions when the OAP mirror is cooled down to 10 K [107]. This base is physically mounted on the shielding. There was a concern about the effect of the cryogenic temperatures on the OAP mirror inside the chamber. In particular, there was a concern over a potential loss of resolution linked to a deformation of the mirror at the lowest temperatures. Simulations were undertaken by the postdoctoral research associate in the group to try and assess (and minimise) the amount of distortion. The material of the mirror, and the selection of a three-screw mounting option with the base integrated into the shielding, achieved the fewest distortions in our simulations (see Figure 4.3).

The second OAP mirror is situated outside of the vacuum chamber, placed above a hole in a breadboard located on top of one of the frames. The rest of the optical relay system is also mounted on the same breadboard. As stated in section 4.2.1, the two mirrors must be near-perfectly aligned. For this reason, the breadboard holding the second OAP mirror, can be adjusted in the x axis and the z (trap)

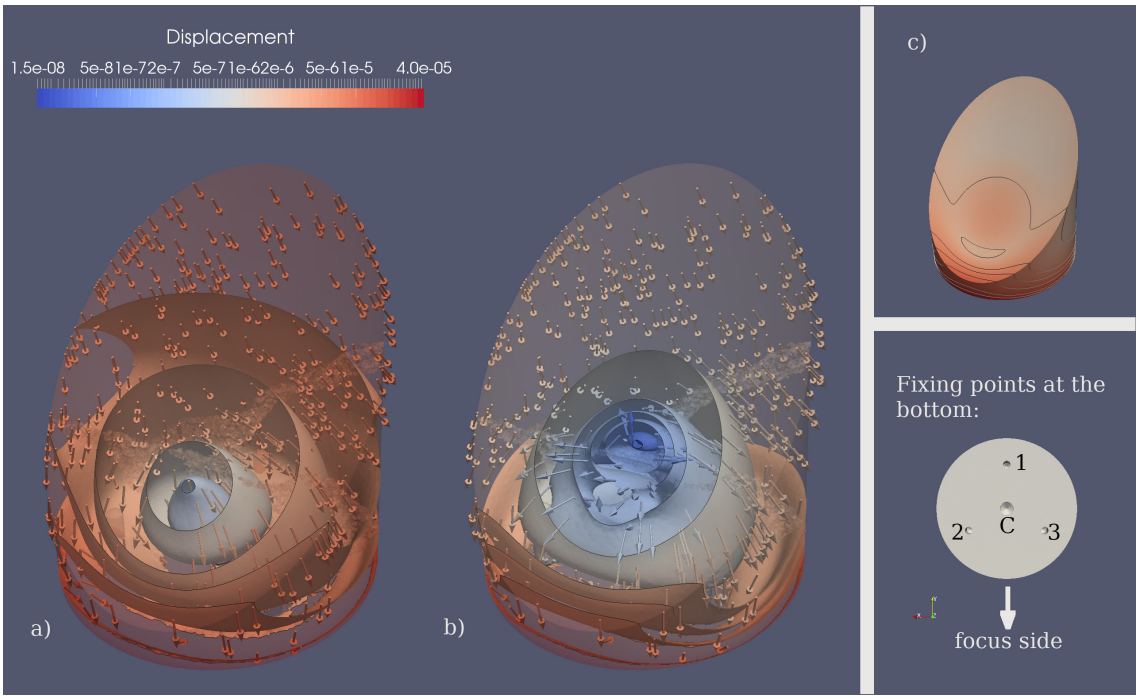

Figure 4.3: Simulation of the thermal deformations of an OAP mirror at 4 K with fixing the OAP to its base unit: a) a central rod, C, fixing the OAP the the base unit; b) three screws fixing the OAP the the base unit, at points 1, 2, and 3; c) when the mirror is not fixed to the base. The direction of deformation is indicated by arrows, and the scale of colours indicates the magnitude of deformation (in m). Reprinted from M. Hejduk et al., Rev. Sci. Instrum. 90 (12): 123701, (2019) [107], with the permission of AIP Publishing.

axis (see Figure 4.4) to better align the two mirrors to one another. After being recomposed by the second OAP mirror, the image is magnified by a microscope objective, mounted on a xyz translation stage and located at the focus point. Lenses of different magnifying power have been purchased to have the possibility of changing the scale of the field of view. Nikon CFI Plan Fluor microscope objectives are used, as they offer a range of magnifications ($\times$4, $\times$20, and $\times$40) with the same focal length. This means that changing lens only requires a very small adjustment

of the alignment system.

After the lens, the image is reflected by a pair of elliptical mirrors, through a 200 mm-effective focal length tube lens, and onto an electron multiplying charge-coupled device (EM-CCD) camera (see Figure 4.2). A cage-based mounting system is used for the optical components located after the pair of OAP mirrors, in order to assist with optical alignment.

4.3 Characterisation studies

4.3.1 Tests outside of the chamber

The OAP mirror relay system was first installed outside of the chamber and tested on the bench (i.e. with no components under vacuum). The two OAP mirrors normally installed along the z axis, perpendicular to the rest of the optical relay, were positioned in the xy plane for practical reasons. A test target was placed close to the first OAP mirror, and back-illuminated by a ultraviolet light emitting diode (UV-LED) at a central wavelength of 395 nm—close to the wavelength of light emitted by fluorescing Ca^+. The difference between the OAP-based optical system and a traditional set-up, using only conventional optics and the microscopic lens, was investigated using a negative 1951 USAF resolution target. Figure 4.5 demonstrates that, although the OAP mirror relay system doesn't achieve the same resolution as the traditional imaging approach with a microscope objective, it can distinguish all features on the target that are separated by more than 2.5 µm [107]. Given the typical inter-ion separation in Coulomb crystals is on the order of 10–20

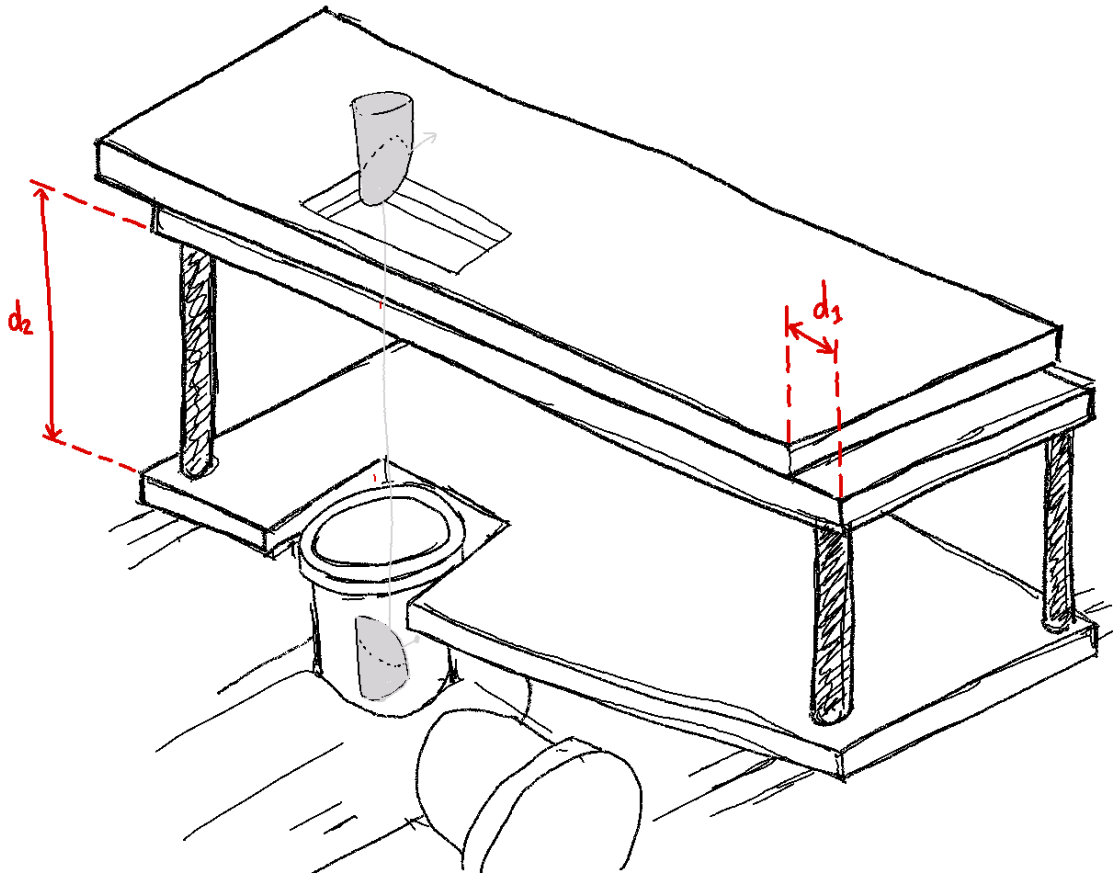

Figure 4.4: Drawing of the breadboard on which the optical system is placed. One OAP mirror is depicted (grey) on the breadboard; the other OAP mirror is shown in the chamber, to show the optical path from the chamber to the breadboard. The red measurements d_1 and d_2 are the possible movements of the breadboard, which modify the position of one OAP mirror with respect to the other.

µm, we confirmed that the OAP-based optical system resolution is sufficient for imaging Coulomb crystals.

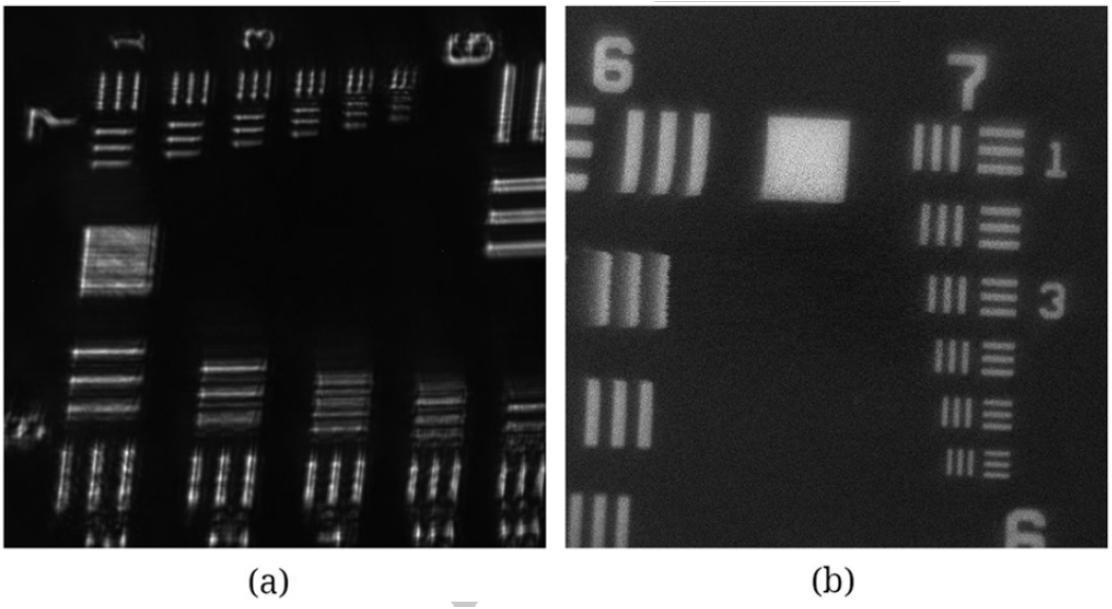

Figure 4.5: Images of the USAF resolution test target back-lit with a UV-LED, acquired outside of the chamber, with and without the OAP mirror relay system, recorded using an EM-CCD camera. a) Image (highest resolution achived) recorded using the OAP mirror relay microscope setup introduced in this chapter. b) The image recorded using a microscope objective without the OAP mirror relay. Reprinted from M. Hejduk et al., Rev. Sci. Instrum. 90 (12): 123701, (2019) [107], with the permission of AIP Publishing.

To examine the performance of the OAP-based imaging system in more depth, another target was tested: a Ronchi ruling of 100 lines per mm. The space between two lines is 10 µm, which is equivalent to the distance between two ions in a Coulomb crystal. As shown in Figure 4.6 of the Ronchi ruling captured by the EM-CCD camera, there are minimal geometric distortions introduced by the imaging and magnification process, establishing that the system is appropriate

for Coulomb crystal imaging. The Ronchi ruling was rotated 90 degrees to test both horizontal and vertical resolution. Adjustment of the alignment of the OAP mirrors also concluded that a shift of one OAP mirror with respect to the other by 0.2 mm resulted in a 2.5-fold decrease in the resolution, reinforcing the importance of aligning the two OAP mirrors carefully.

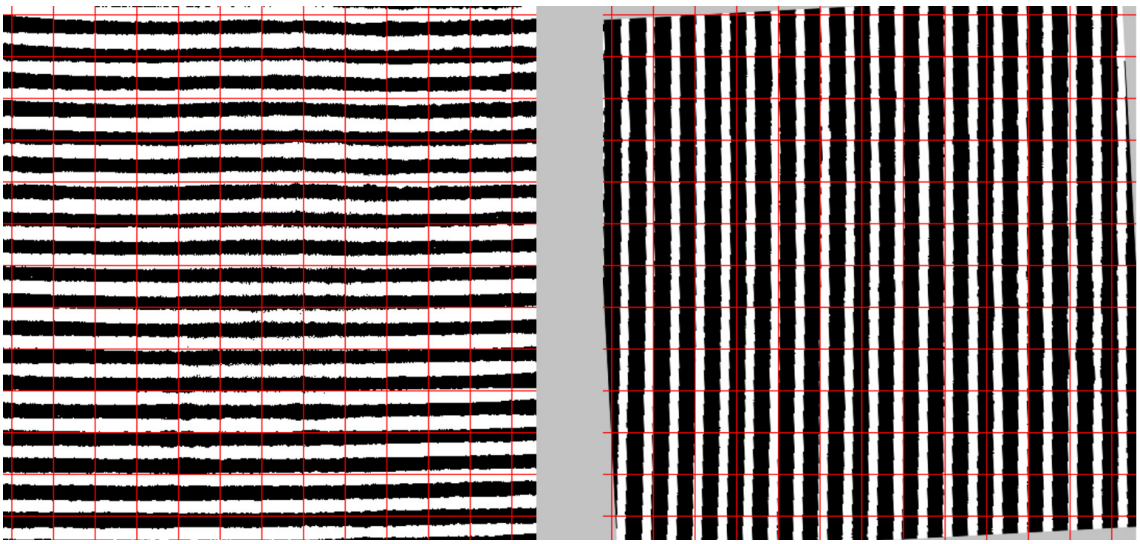

Figure 4.6: Binarized images of a Ronchi ruling with 100 lines per mm features, backlit by a UV-LED, acquired outside of the chamber, after the OAP mirror relay, with an EM-CCD camera. The red grid is to aid the eye to evaluate the performance of the imaging relay. The field of view is approximately 200 µm × 200 µm. Reprinted from M. Hejduk et al., Rev. Sci. Instrum. 90 (12): 123701, (2019) [107], with the permission of AIP Publishing.

4.3.2 Inside the chamber, comparison at room temperature and cryogenic temperatures

Following the successful characterisation of the OAP-based imaging system on the bench, the first OAP mirror was installed inside the vacuum chamber. The second OAP mirror and the rest of the optical system has been installed onto the breadboard. The system was aligned using a He-Ne laser situated in front of the ion trap. The Ronchi ruling was fixed to a blade that can be installed inside the ion trap, to enable the imaging system to be optically aligned. As used for the bench-top tests, a UV LED was installed at the front of the ion trap to illuminate the back of the grid, enabling it to be imaged by the first OAP mirror, reflected to the second OAP mirror, and then relayed by the optical system onto the camera. The performance of the imaging system was characterised at both room temperature and at cryogenic temperatures, to ensure that crystals can be effectively imaged under both sets of conditions.

In this experiment, we used the ×40 microscopic objective so the field of view that we observe is around 200 × 200 µm. We investigated the effects of shifting one OAP mirror with respect to the other along the x axis by using the translational movement of the breadboard, depicted as d_1 in Figure 4.4. Results are shown Figure 4.7. We can see that by translating one OAP mirror with respect to the other in the x direction, there is very noticeable tilting in the image, and distortions are introduced. At both room temperature and at cryogenic temperatures, we can observe that even a 0.5 mm shift induces a tilting of the image. But this also shows that there is no difference in the resolution between

the images taken with the system at cryogenic temperatures and room temperature.

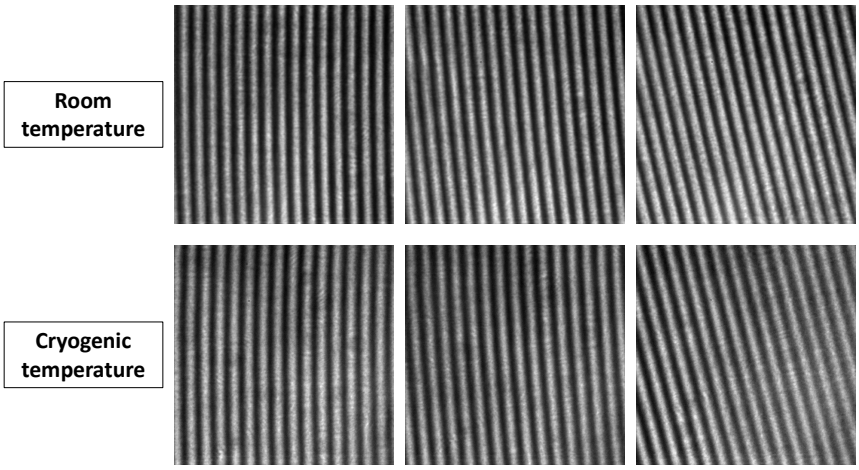

Figure 4.7: Images of the Ronchi ruling taken at room (upper panels) and cryogenic (lower panels) temperatures. On the left-hand column, the two mirrors are perfectly aligned. On the middle column, the two OAP mirrors are shifted by 0.2 mm from one another in the x axis and on the right-hand column, the two OAP mirrors are shifted by 0.8 mm from one another.

We also looked at the effect of modifying the distance between the two OAP mirrors by lowering and raising the breadboard, depicted as d_2 in Figure 4.4. This step doesn't seem to introduce any distortions or any change in the recorded image, at room temperature or at cryogenic temperatures, contrary to what was expected

from previous work [108].

Using the parameters optimised with these results, we looked at the image of the grid, placed both horizontally and vertically, to assess the resolution. The results are shown in Figure 4.8. The difference in the resolution of the grid at room temperature and at cryogenic temperatures is minimal. This shows that the performance of the OAP mirror cooled at cryogenic temperatures is not impaired. It also demonstrates how the steps that we took to limit the coupling of vibrations from the pulse tube cryocooler to the imaging system have proven to be effective. The scale provided on Figure 4.8 gives an idea of the resolution of 50 µm, with the distance between two lines 10 µm, around the same scale as the distance between ions in Coulomb crystals. Excellent resolution is achieved for both cryogenic and room temperature conditions.

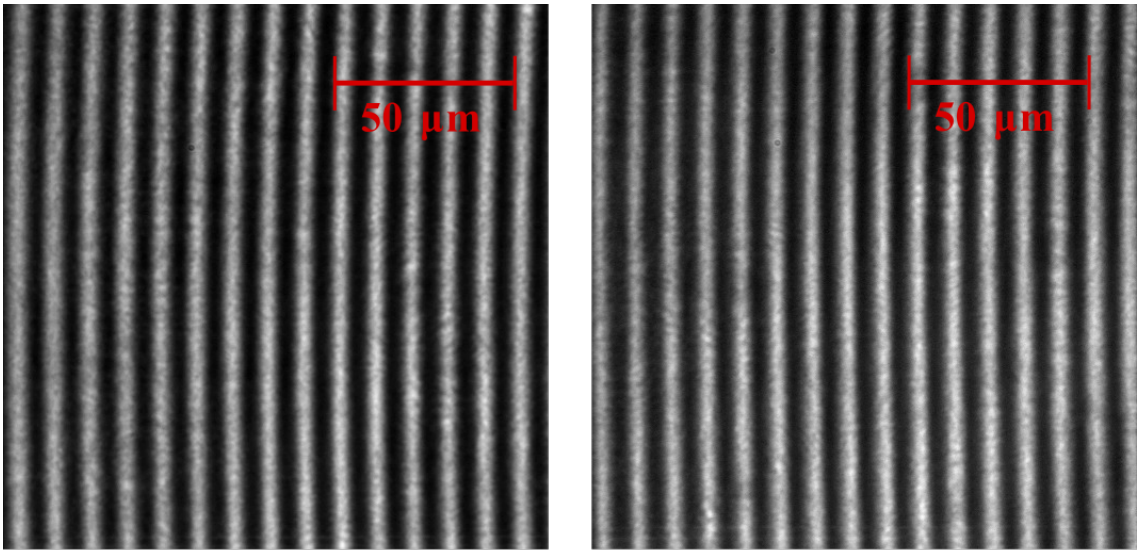

Figure 4.8: Images of a Ronchi ruling (100 lines per mm), positioned at the centre of the ion trap region under ultra-high vacuum, recorded with an EM-CCD camera. The Ronchi ruling is back-lit with a UV LED, with the image relayed by the pair of OAP mirrors to the camera. Left image: recorded with the ion trap region at room temperature (approximately 295 K), with the cryocooler off. Right image: taken with the cryocooler on, with the OAP mirror and ion trap at 9 K. Reproduced from C. Miossec et al., Rev. Sci. Instrum., 93 (3): 033201 (2022) [74].

Chapter 5

Experimental characterisation of the cryogenic ion trap

Parts of this chapter are based on work that has previously been published in a Review of Scientific Instruments article by Miossec et al. (2022) [74].

5.1 Anti-vibration system

Cryogenic conditions are reached through the use of a pulse tube cryocooler, as mentioned in Chapter 3. It has been previously documented that pulse tube cryocoolers generate vibrations—particularly at the pulse tube frequency of 50 Hz, at higher harmonics of this frequency, and at the cold head frequency of 1–2 Hz [109, 110]. The amplitude of the vibrations are reported to be ∼10 µm at each stage of the cryocooler cold head [111]. The stages of the cold head are directly inserted inside the chamber, and are connected to the ion trap to reach the necessary cryogenic temperatures. The valve unit, connected to the cold head by short tubes, also needs to be located in the vicinity, and the valve can act as an additional source of vibration. This raises the question of the impact of such vibrations on the ion trap. As the amplitude of the vibrations at the cold head stages are similar to the inter-ion spac-

ing in Coulomb crystals, the propagation of such vibrations to the ion trap region could impede imaging resolution. In a bid to minimise the transmission of vibration noise to the ion trap region, the main sources of vibration (and ways to minimise these vibrations) have been considered in how the components of the chamber come together. Multiple design choices are part of this anti-vibration system.

5.1.1 Description

As stated above, the challenge is to balance the need for the ion trap to be in close proximity to the cryocooler with minimizing the impact of vibrations on the ion trap. To achieve this goal, the apparatus is made up of two parts, with each of these components sitting on a different frame. The chamber, the cold head of the cryocooler and part of the first stage shielding are supported by one frame; the ion trap, the other part of the first stage shielding, the second stage shielding, the Heim column and a hexapod are supported by a second frame. This is pictured Figure 5.1, with the two frames depicted in different colours. The second frame is nested inside the first frame and mechanically connected to it by a flexible stainless steel bellow. The ion trap and its shielding rest on the Heim column, itself mounted on the lower part of the bellow. While the Heim column serves to isolate the ion trap thermally (from the chamber walls, see section 3.2.4.), the bellow positioned below the Heim column also isolates the ion trap vibrationally from the cold head.

As explained in Chapter 3, the thermal contact between the ion trap and the cold head is achieved by copper braids. They connect the cold head to the second stage cold shield in contact with the ion trap, with a second set of braids

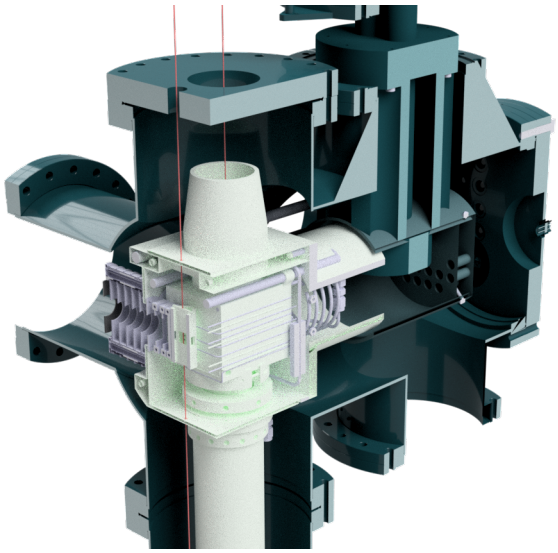

Figure 5.1: Cut view of the cryogenic ion trap to show the dual-frame system. The outside chamber, the cold head and the shielding connected to the cold head, that are all resting on one frame, are shown in green. The ion trap, the shielding that surrounds it, the Heim column, that are all resting on the other frame, are depicted in white. The two parts of the apparatus are connected through a bellow at the bottom of the Heim column (not shown), and through copper braids that connect the shielding surrounding the cold head and the shielding surrounding the ion trap.

connecting the two parts of the first stage shielding—one part surrounding the cold head and the one surrounding the ion trap (see Figure 5.1). The custom-made braids very effectively damp the vibrations, due to their woven and flexible structure.

Finally, the valve unit of the cryocooler that needs to be in close vicinity to the cold head is mounted on a shelf attached to the ceiling. It is not in contact with any of the frames, ensuring that the propagation of vibrations from the valve unit to the ion trap region is minimal.

5.1.2 Characterisation measurements

Experimental method

To make sure that the steps taken to minimise vibrations are effective, with only a negligible impact on the imaging, we characterised the vibrations at different positions on the apparatus. We installed accelerometers on the two frames, on the chamber and on the ion trap itself, to establish both the frequency and the amplitude of vibrations as a function of time, and under different conditions.

Two different piezoelectric accelerometers were selected, with a sensitivity of 1000 and 500 mV/g. By performing a Fourier Transform of the acceleration, we obtain the frequencies recorded by the accelerometer. The displacement of the accelerometer is calculated by double integration of the acceleration over a moving time window of 0.10 ms.

Quantifying the vibrations

One accelerometer (500 mV/g sensitivity) was mounted directly on the ion trap to record the frequencies of the vibrations, with the cryocooler on and off. The results are shown in Figure 5.2. One can observe that, aside from the slightly smaller intensity of the peak at 50 Hz (the frequency at which the cryocooler compressor unit operates) when the cryocooler is turned off, there is very little difference in the amplitude of the frequencies recorded. This implies that most of the vibrations at the ion trap arise from other sources of vibration—and not the cryocooler. This finding was both encouraging, as it confirmed that the cryocooler vibration-damping measures introduced into the design were successful,

and unexpected, as it indicated that vibrations can still be detected at the ion trap.

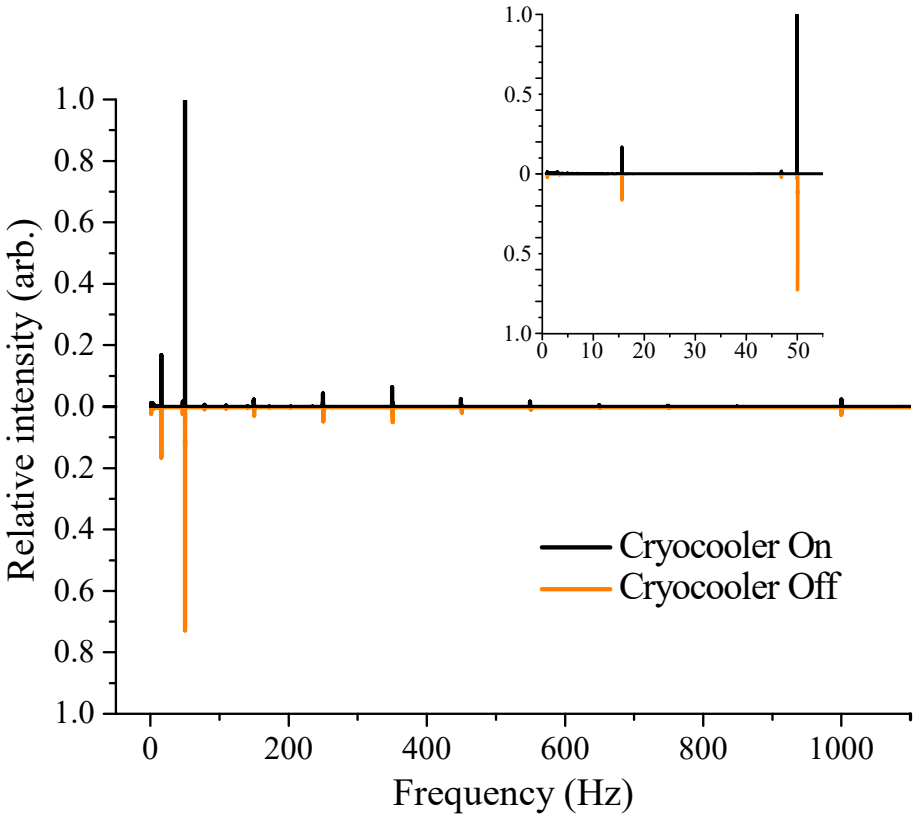

Figure 5.2: The frequencies of vibrations recorded with the accelerometer positioned on the ion trap are plotted, recorded both with (black) and without (yellow) the cryocooler on. Measurements are recorded at a sampling frequency of 10 000 Hz. The main plot displays the frequencies and relative intensities of all vibrations, with the majority of these arising from sources other than the cryocooler. The inset (top right corner) is a zoomed-in plot of the low-frequency region. Reproduced from C. Miossec et al., Rev Sci Instrum, 93 (3): 033201 (2022) [74].

We recorded the vibrations at the same position (with the cryocooler turned off), and compared the plot recorded when all the pumps (scroll pumps and turbo-molecular pumps) are on, and when all of them are turned off. Results are shown in Figure 5.3. We can see that almost all the frequency peaks are absent

when the pumps are turned off, confirming that most of the vibrations observed at the ion trap are not coming from the cryocooler, but from our vacuum pumps. The peak at 1000 Hz can be attributed to the vibrations of the turbo-molecular pump, which operates at this frequency. Very pleasingly, there are no obvious features observed below 10 Hz, despite the drive frequency of vibrations at the two stages of the cold head occurring in this region (at 1-2 Hz; the lower bandwidth detection limit for both accelerometers is 0.5 Hz). Since these data were implemented, we have taken several steps to further suppress the vibration arising from the vacuum pumps. In particular, the connections between the pumps and the chamber have been altered to reduce the transmissions of vibrations, alongside the addition of padding where tubing was in close proximity to the frame.

Finally, the peak at 16 Hz is still present when all our pumps are turned off, suggesting that these vibrations are from another (as yet unidentified source) in our laboratory and cannot easily be diminished.

We had not previously needed to undertake any precautions to minimise the transmission of vibrations from the vacuum pumps to the ion trap region. As such, we sought to ascertain the amplitude of the vibrations at the ion trap; provided the amplitude of the vibrations is less than the minimum distance between neighbouring ions in a Coulomb crystal, i.e. 10 µm, then the presence of small levels of vibration are unlikely to affect the resolution of crystal images.

To test this, the 1000 mV/g sensitivity accelerometer was positioned under the

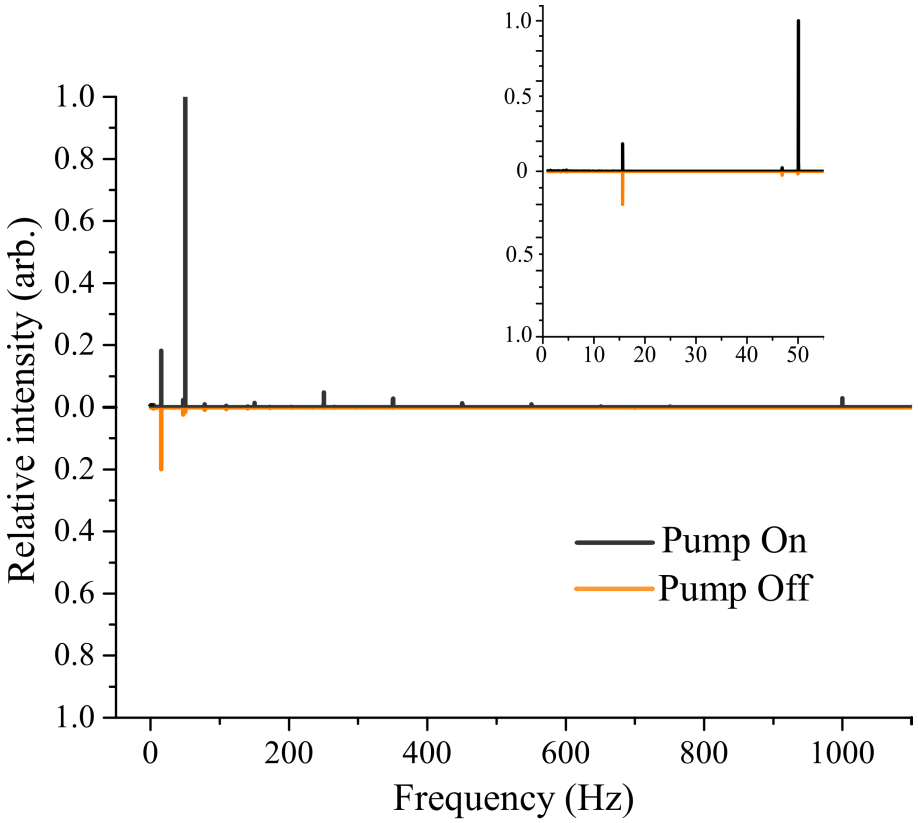

Figure 5.3: Frequencies of vibrations recorded when the cryocooler is off, with the vacuum pumps on (black) and off (yellow). Large differences between the "on" and "off" traces can be seen, especially in the peak at 50 Hz. The inset (right corner) is a zoomed-in plot of the low-frequency region. Reproduced from C. Miossec et al., Rev. Sci. Instrum., 93 (3): 033201 (2022) [74].

bellow, on the frame supporting the ion trap. We plotted in Figure 5.4 the displacement of the accelerometer in the horizontal plane over time, both when the cryocooler is off and on. This way, we have a clear idea of the capacity of the cryogenic ion trap imaging system to operate at cryogenic temperatures. Again, there is very little difference in the displacement observed when the cryocooler is on or off. These measurements demonstrate the positive impact of the anti-vibration measures included in the design. More importantly, in both cases the frame is

displaced by a maximum of approximately 0.5 µm due to vibrations—more than an order of magnitude lower than the amplitude of the vibrations at the cold head quoted by the manufacturer. This is also significantly lower than the distance between two ions in a Coulomb crystal, and should be low enough that it does not impact the imaging of Coulomb crystals.

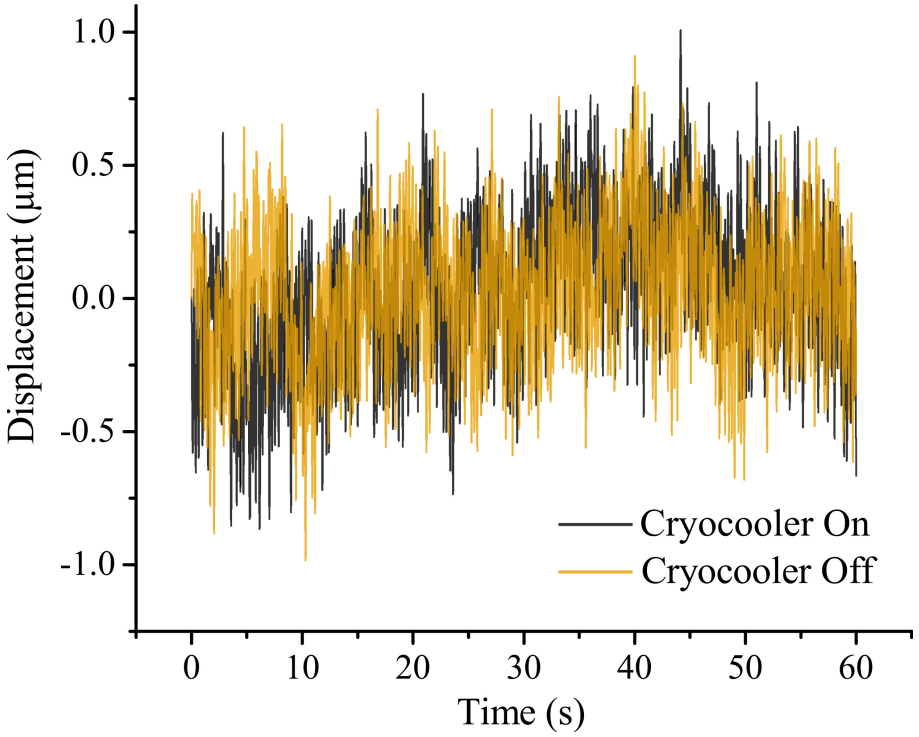

Figure 5.4: Vibrations recorded outside the chamber with an accelerometer situated on the frame supporting the ion trap. The measurements show vibrations in the horizontal plane, recorded with the cryocooler on (black) and off (yellow). Reproduced from C. Miossec et al., Rev. Sci. Instrum., 93 (3): 033201 (2022) [74].

By comparison, the original CryPTEx characterisation studies reported vibrations of magnitude 7–9 µm at the trap centre. While this was considered to be 'low', such vibrations would be too high for our apparatus, due to the novel design of our opti-

cal system. It is notable that reducing these vibrations was explicitly addressed in the next generation CryPTEx designs, as the CryPTEx-PTB included specific anti-vibration systems to limit vibrations from their pulse tube cryocooler [80]. They were able to obtain a displacement below 20 nm in the horizontal plane and below 100 nm in the vertical direction. Building from this successful way to limit vibrations, the CryPTEx-SC incorporated additional design elements to minimise vibrations [81, 111], achieving the lowest vibration level reported for such a closed-cycle system. Such low vibrations, while important for their studies on highly charged ions, are not needed for our experimental set-up, as our main objective is the optical resolution of the images of the Coulomb crystals at the ion trap center.

5.2 Temperature measurements

5.2.1 Recording the temperature at different locations in the apparatus

After characterising the vibrations of our system, we needed to characterise the cryogenic capabilities. The design choices related to the cryogenic system are detailed Chapter 3. The two stages of the cold head have the capacity to reach temperatures as low as 45 K and 4.2 K (at the first and second stage, respectively). These temperatures have been recorded by the manufacturer with the cold head isolated (with no load attached to it) and with up to 10 protective layers surrounding it. In our case, the two stages of the cold head are connected to warmer parts of the apparatus and, although we tried to limit as much as possible the thermal connection between the different components, there will inevitably be a constant

load on the cold head. Therefore, we expected the temperature at the ion trap to be higher than 4.2 K, but wanted to verify the ability of the apparatus to reach temperatures ≤ 10 K in the ion trap region.

To verify if this was possible, we mounted thermosensors at different places on the two cold stages. We used a platinum resistance thermometer and two silicon diodes from Lakeshore for this purpose. The resistance thermometer was placed on the first stage of the cryocooler, as it can only record temperatures up to 14 K—lower than the temperatures achievable at the first stage of the cold head, but higher than the temperatures achievable by the second stage of the cold head. The two thermodiodes—each able to record temperatures as low as 1.4 K—are connected to the second stage cold shield, one under the cold head, and the second directly mounted on the ion trap. The temperatures at all these locations within the chamber can be simultaneously recorded over time.

5.2.2 Results

As can be seen in Figure 5.5, the temperature recorded at the two stages goes down very quickly once the cryocooler is turned on. The temperature recorded at the first stage cold shield plateaus after 12 h at 61 K. It can be seen that the temperature at the ion trap plateaus at 8.89 K, achieving the goal of reaching temperatures below 10 K within 8 h. This confirms that temperatures below 10 K can be attained in the ion trap region, validating the design choices outlined in Chapter 3.

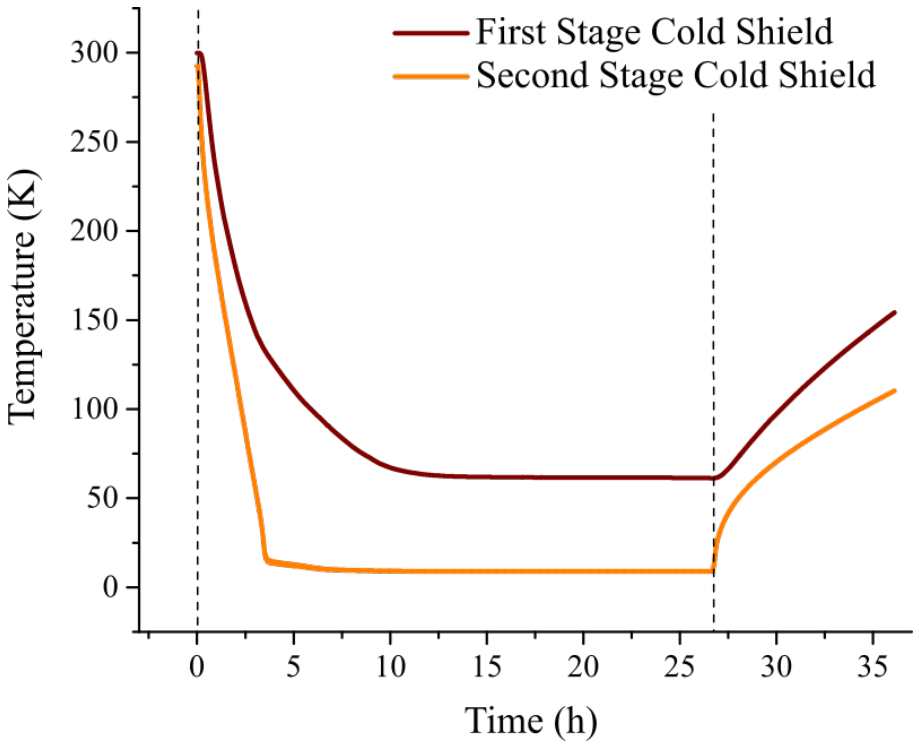

Figure 5.5: Temperatures recorded at the first outer radiation shield (dark red) and second inner radiation shield (orange) stages, plotted as a function of time. The first vertical dashed line indicates when the cryocooler was turned on, and the second dashed line corresponds to when the cryocooler was turned off. Reproduced from C. Miossec et al., Rev. Sci. Instrum., 93 (3): 033201 (2022) [74].

5.3 Time-of-flight Mass Spectrometer detection capability

The cryogenic ion trap apparatus includes an integrated ToF-MS to be able to study not only the kinetics, but also the dynamics of reactions, with its design detailed in Chapter 3. As a brief reminder: the trapped particles are ejected from the ion trap by applying static voltages to the pairs of rods. The ejected ions then pass through focusing electrodes and a ToF tube, towards a MCP detector (see

Figure 5.6). Using the flight length and the voltages applied to the rods (and other electrodes), we can convert the time-of-flight traces into mass spectra and assign what species give rise to the recorded features. In the first instance, no voltages have been applied to the focusing electrodes or the flight tube.

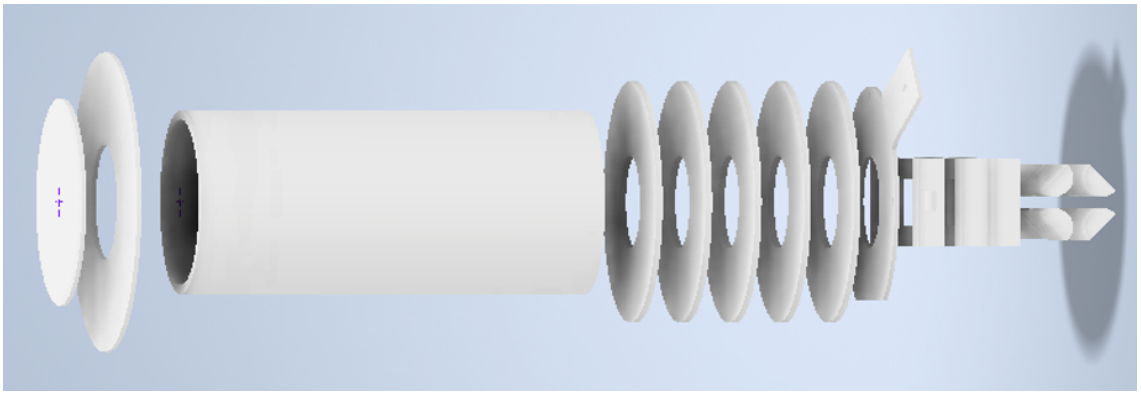

Figure 5.6: Schematic illustration of the ToF-MS setup. The ion trap is depicted on the extreme right, with the following rectangular electrodes being directly attached to the second stage cold shield after the ion trap. Then, there are circular electrodes and time-of-flight tube attached from the chamber flange. Finally, the MCPs front plate is shown on the extreme left. Each component is electronically isolated, and an independent voltage can be applied to it. The distance from the center of the ion trap to the MCPs is 20.78 cm

.

5.3.1 Time-of-flight traces

The ToF-MS was first tested with a continuous voltage applied to the two pairs of ion trap rods, to continuously extract the contents of the trap. This allowed us to perform initial tests with fewer variables. For example, the calcium oven and lasers had to be aligned to the trap centre to form ions, and the detection system had to be tested to ensure the ions were being extracted onto the MCPs. The first ToF

signal obtained with continuous extraction is shown Figure 5.7.

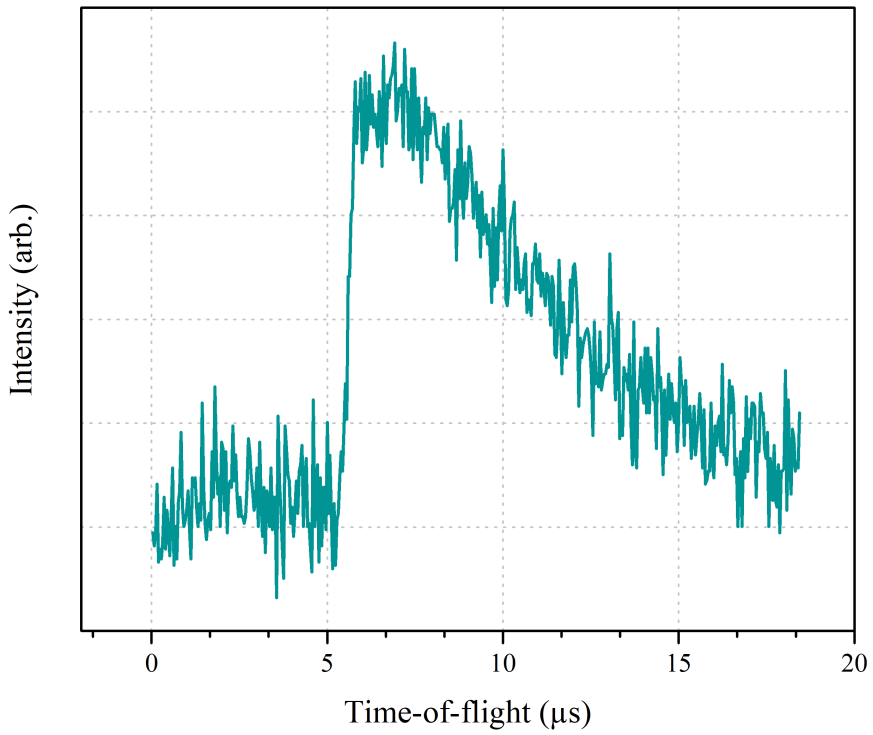

Figure 5.7: Experimental time-of-flight trace obtained from continuously applying a voltage to the repeller-extractor pair, and ejecting Ca^+ ions formed in the ion trap.

Once the signal was optimised with continuous extraction, we tested the ToF signal by initially trapping, then extracting, Ca^+—as would happen in the course of a reaction study (see Figure 5.8). This first experimental TOF-MS trace of ejected Ca^+ was relatively small, and as we zoomed on it, it can appear digitized. The signal from this procedure is higher in magnitude than the peak of continuously extracted ions, as it is possible to build up a more dense sample of Ca^+ when initially

trapping the ions (instead of immediately ejecting them as soon as they are formed).

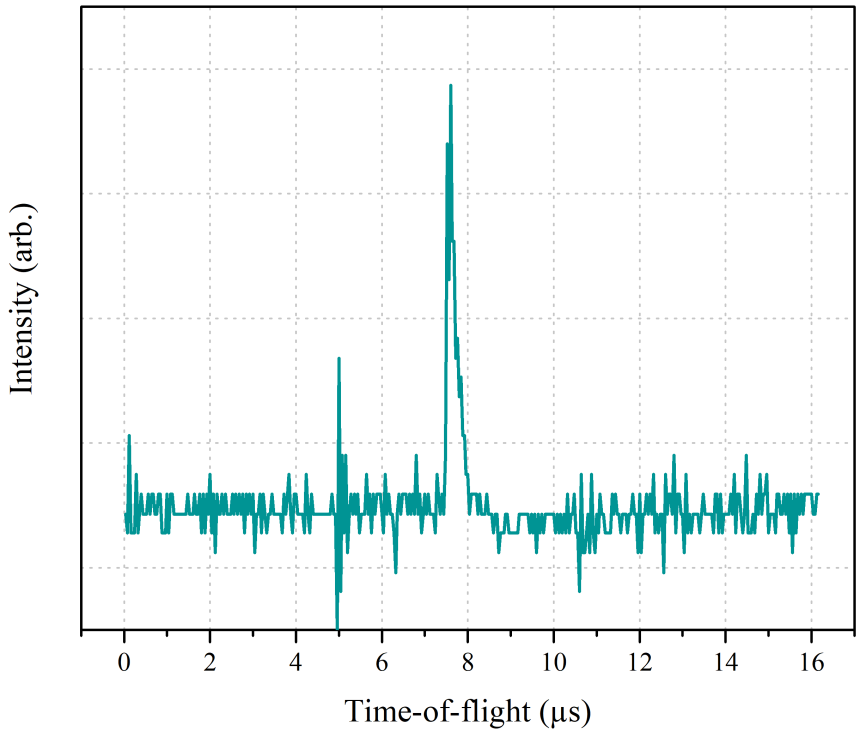

Figure 5.8: Experimental time-of-flight trace, demonstrating that Ca^+ ions can be formed in—and subsequently ejected from—the trap, enabling mass-sensitive analysis of the trap contents. Repeller and extractor voltages are applied to the ion trap rods after trapping the ions for a few minutes, converting the trap into a two-stage Wiley-McLaren style time-of-flight mass spectrometer. (For this characterisation measurement, all other electrodes and the time-of-flight tube are grounded.)

5.3.2 ToF signal of Coulomb crystals

In the absence of laser cooling, ions cannot be confined by the trapping potentials for long times. After 90 s, the ToF signal shows that nearly no Ca^+ remains in the trap. By laser cooling the Ca^+ (see Chapter 6), their kinetic energy is reduced and ions can be confined in the trap for an extended period of time—potentially up to hours, provided the lasers and experimental conditions are stable. In initial characterisation tests with this set-up, laser-cooled Ca^+ ions have been held in the trap for up to 4 h before being ejected and detected. More ToF results are presented alongside images of Coulomb crystals in Chapter 6.

Chapter 6

Fluorescence and Coulomb crystals

6.1 Parameters to set

Our Linear Paul trap is operated using a modified RF Generator from Stahl Electronics, combined with a custom-made DC bias and extraction pulser. As set out in Chapter 2, each of the four trap rods is composed of three segments. The DC bias supply box allows us to control the DC voltages applied to the segments, with the various combinations of offset voltages that can be applied depicted in Figure 6.1. Altering the DC offset voltages applied to one or more trap segments allows us to move a cloud of trapped ions inside the trap, in order to counterbalance the effects that a misalignment of the rods could induce, ensuring that the trapped ions can be located in the trap centre. While modifying the parameters E and F individually would alter the position of the trapped ions along the z-axis, the modification of the offset B, C and D would alter their position in the x- and y-plane. Finally, offset A, corresponding to the segments at each end of all the rods (i.e. the endcaps), can be directly correlated to U_{end}, and will impact the depth of the trapping field along the z axis and therefore shape of the ion cloud.

The extraction pulser achieves the extraction of the ions towards the MCP detector.

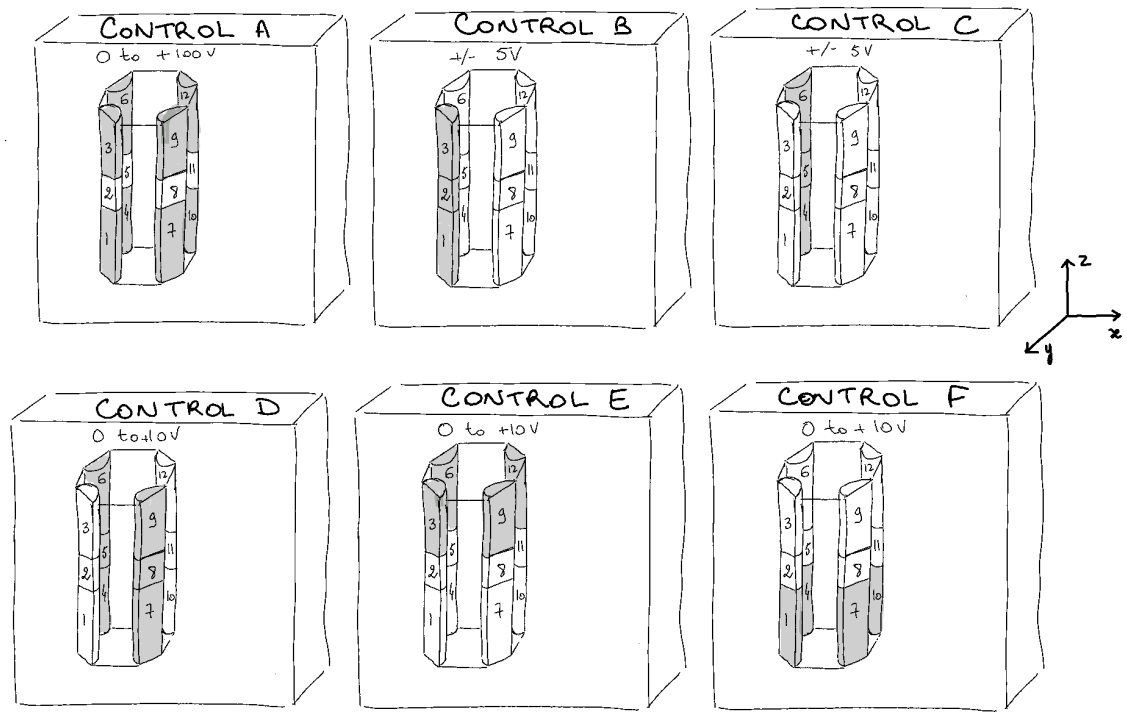

Figure 6.1: Illustration of the different segments of the ion trap, with the six ways that the voltage applied to the various segments can be altered shown in grey. The cube represents the second stage cold shield to which the ion trap is attached.

At the moment of extraction, one presses the extraction button and this turns off the oscillating voltages for a previously configured amount of time. Just after the oscillating voltages are turned off, a continuous voltage is applied to the pairs of rods. One pair (the furthest away from the MCPs) is the repeller pair and the second pair is the extractor pair. By applying a higher voltage on the repeller than on the extractor, the potential difference will direct the trapped ions towards the MCPs.

The extraction voltages are set and applied with the extraction pulser. From there, we can also decide the time the extraction is on and the delay from the moment the

button is pressed to the moment the extraction pulses are applied. These values need to be determined experimentally. If the delay is too big, by the time the extraction pulses are turned on, all the ions that were held by the oscillating voltages may have escaped the trap. In our other ion trap, we know that we can introduce a delay of 1.3 µs without losing any ions, but within a few seconds, many ions will be lost. Similarly, we want to make sure that the width of the extraction pulse is big enough to make sure all ions have been extracted before turning off the extraction voltages.

6.2 Obtaining fluorescing clouds

One of the hardest parts of obtaining fluorescence images is associated with alignment. Both diode lasers must be perfectly aligned with one another, and with the ion cloud, in order for laser cooling to be effective. Finally, the camera must be positioned to collect fluorescence from the ion cloud in the center of the ion trap. The focal point of the camera system can be altered by moving the microscope objective on an x,y translation stage.

In order to assist in the alignment of the lasers with the camera, a fiber has been installed that can be moved to the physical center of the ion trap, where we can make sure that the camera is looking at the fiber and that the diodes are also aligned to hit the fiber. Knowing that these parameters are concordant, we can then move the cloud of ions within the trap by altering the DC offset voltages (as set out above) until fluorescence is detected. From the first sign of fluorescence, through an iterative process, we bring the cloud to the trap center and adapt the diode laser positions and camera focal plane accordingly. Through this whole

process, the 4× microscope lens is used to provide a bigger field of view, giving us more chance of observing this first fluorescence, and to manipulate the cloud with more range. An image of a fluorescent ion cloud obtained in this way is shown in the left image of Figure 6.2.

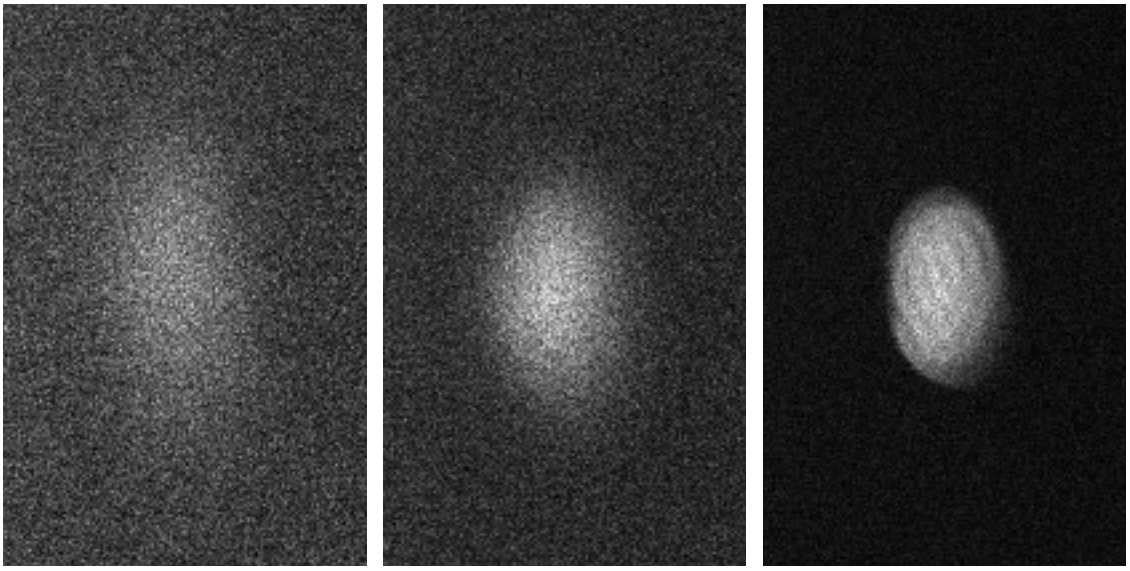

Figure 6.2: Images of the Coulomb crystals obtained in our cryogenic ion trap with the EM-CCD camera. The images show different stages of the crystallisation process. On the left, it is a fluorescence cloud, in the middle, a colder cloud of Ca^+, and on the right, a fully crystallised Coulomb crystal. The series of images were obtained by progressing lowering the wavelength of the blue diode laser from 396.959 215 nm to 396.959 185 nm whilst keeping all other parameters fixed. The $2V_{\mathrm{RF}} = 100\,\mathrm{V}$ and $U_{\mathrm{end}} = 2\,\mathrm{V}$.

6.3 Obtaining Coulomb crystals

Once a cloud of trapped ions has been confined and fluoresces, we modify both the wavelength of the blue diode laser and the V_{RF} amplitude (i.e. the trap

depth) to make the cloud more stable until a phase transition occurs, forming a Coulomb crystal. The phase transition shows a sudden change in the intensity of the fluorescence and a more confined shape of the (previously diffuse) cloud of ions. When it is more stable and the focus has been optimised, we can observe the dots representing the lattice positions of Ca^+ ions within the crystal. The first Coulomb crystal we obtained, prior to optimisation, is shown in Figure 6.3.

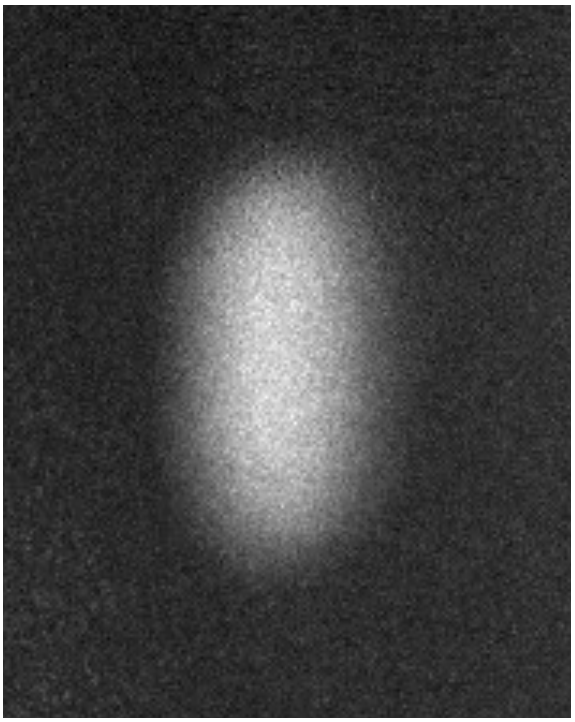

Figure 6.3: Image taken by the EM-CCD camera of the first fluorescence of a (non-optimized) Ca^+ Coulomb crystal.

As mentioned above, by tuning the focus of the microscopic lens, finding the best wavelength of the blue diode laser, ensuring that the Coulomb crystal is at the center of the ion trap, where the potential is minimised and therefore where

the Coulomb crystal is most stable, the crystal was able to be optimised. These steps can still be optimised further, with in-depth characterisation of the trapping, laser cooling and imaging parameters needing to be conducted periodically. For example, by changing to the 20× microscopic lens, we can tune more precisely the parameters as we can see the features of the crystal more clearly. An example of more defined Coulomb crystals, recorded with the 4× and the 20× microscope lenses, are provided in Figure 6.4. We can observe how the field of view changes between the two microscope lenses. Because the parameters are different for the 20× microscope lens than with the 4× magnification one, the image is yet to be fully optimized and is included to illustrate the differences between the two microscope lenses.

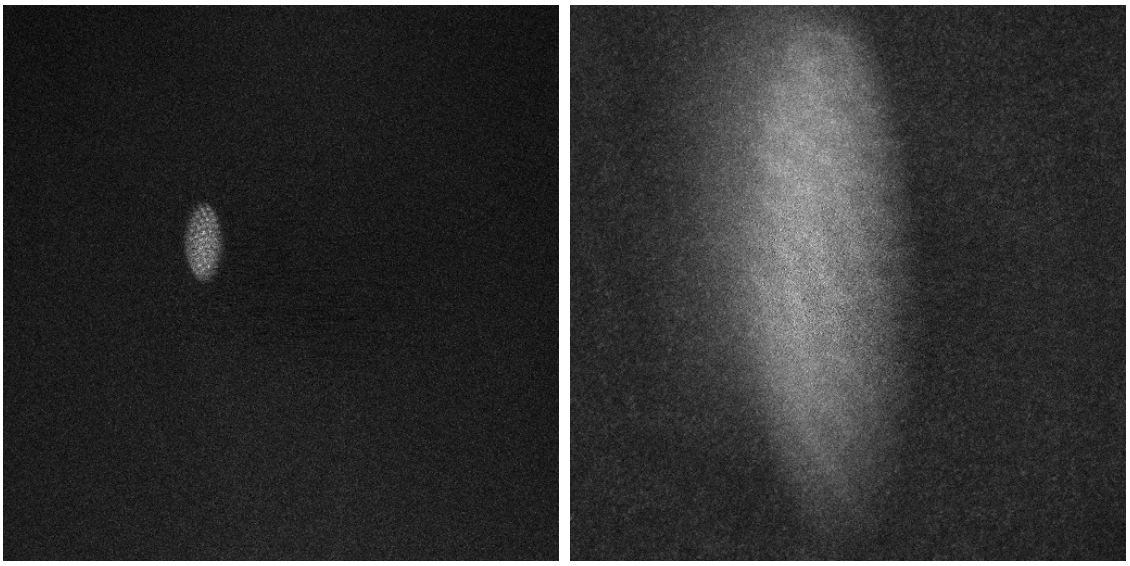

Figure 6.4: Images of the Coulomb crystals obtained in our cryogenic ion trap with the EM-CCD camera, using two different lenses; left: 4× magnification, right: 20× magnification.

We have looked at the impact of different parameters on the Coulomb crystals and have reported this in Figures 6.5, 6.6 and 6.2. In Figure 6.5, we have looked at the images obtained with different sizes of Coulomb crystals, from the smallest to the largest Coulomb crystal. This is obtained by modifying the time the beam of Ca atoms is exposed to the ionization beam, from a few seconds for the crystal on the left, to 45 seconds for the crystal on the right.

In Figure 6.6, we have modified the V_{RF} parameter from 80 to 120 V peak to peak, from the left to the right respectively. What is observable is how the crystal, broader at lower V_{RF}, is more and more confined for higher V_{RF}.

Finally, we recorded images of the fluorescence of Ca^+ in Figure 6.2. The picture on the left shows a fluorescence cloud, where the transition to a Coulomb crystal has not happened yet. The wavelength of the blue diode laser in that case was 396.959 215 nm. By lowering this wavelength to 396.959 200 nm, we lower the temperature of the ions, and we see in the middle image that the fluorescent cloud is more confined and the fluorescence intensity is stronger. By lowering even more the wavelength to 396.959 185 nm, we see the sudden transition in the fluorescence that gives the sharper Coulomb crystal image observed on the right image. This last wavelength has been found to be the more stable wavelength for Coulomb crystals, that allow for the resolution of individual lattice positions. Lowering the wavelength even more, we lose this resolution until the crystal melts past λ =396.959 175 nm. This shows how sensitive the Coulomb crystals are to the wavelength of the blue diode laser wavelength as only altering it a small amount

has a huge effect on the crystal.

We can observe that the fluorescence images of Coulomb crystals are somewhat blurry, and the ions are not perfectly well defined. Multiple test can be done to help obtain better resolution; by removing the microscopic objective and putting the camera directly after the OAP mirror, we can check that blurring has not been induced by the microscopic objective. This could also be coming from the parameters of the ion trap itself that may not be optimal. Finally, if we wanted to confirm if the problem comes from the fluorescing ions or the imaging system, we could use a USAF resolution test target, as was done with the imaging system on the bench.

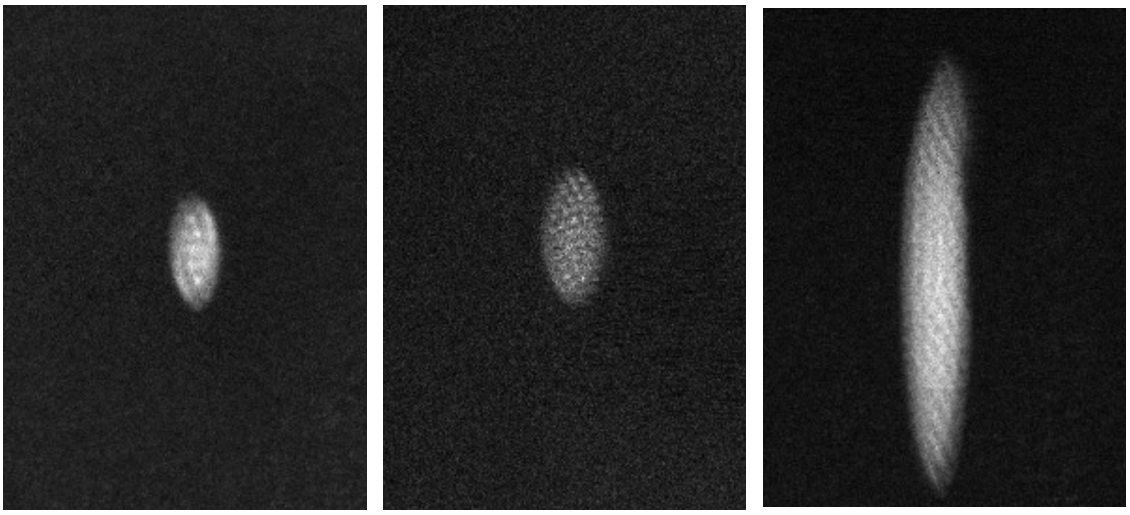

Figure 6.5: Images of the Coulomb crystals obtained in our cryogenic ion trap with the EM-CCD camera. The different size of Coulomb crystals were obtained by altering the time of ionization of Ca. $2V_{\mathrm{RF}} = 100Vpp$ and $U_{\mathrm{end}} = 2V$ except for the image on the left where $U_{\mathrm{end}} = 1.5V$.

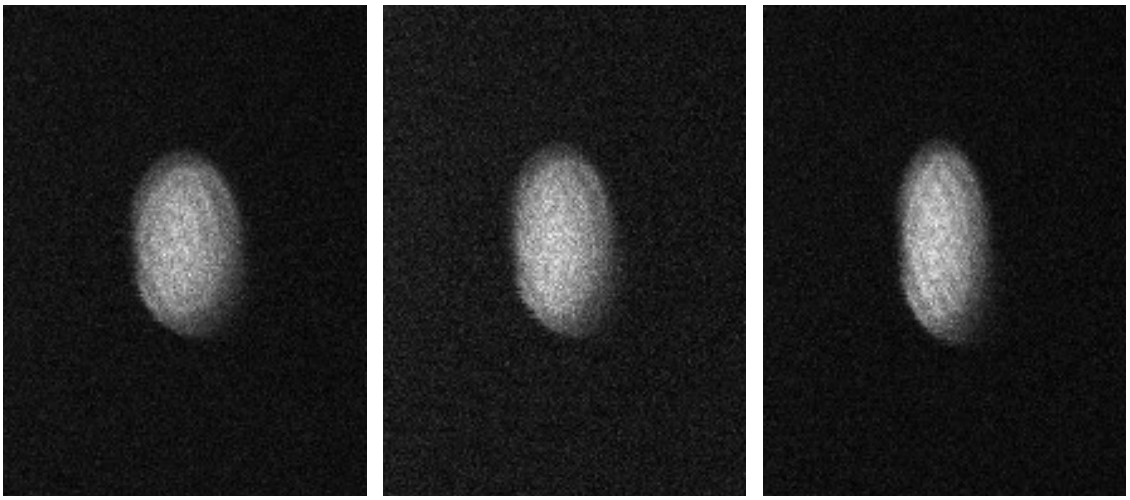

Figure 6.6: Images of the Coulomb crystals obtained in our cryogenic ion trap with the EM-CCD camera. The images show the Coulomb crystals at different values of V_{RF}, with U_{end} fixed at 2 V. Left: $2V_{\mathrm{RF}} = 80\,\mathrm{V}$, middle: $V_{\mathrm{RF}} = 100\,\mathrm{V}$, right: $U_{\mathrm{end}} = 120\,\mathrm{V}$.

Finally, we looked at ejecting the Coulomb crystals to record ToF traces—with the ultimate goal being to use both imaging and ToF detection techniques to monitor reaction processes. We can integrate the ToF signal to gain quantitative measurements of the relative numbers of each ionic species in the trap at a selected time, as seen in previous work [105, 112]. The corresponding image of the Coulomb crystals can be compared with Coulomb Crystal Molecular Dynamics (CCMD) simulations to obtain the number of ions. This will give us a clear benchmark for the correlation between the number of ions and the ToF spectra, which is required for reaction analysis.

Figure 6.7 shows a ToF trace of a Coulomb crystal next to an image of this Coulomb crystal before its ejection towards the MCPs. Although the peak is well defined, its intensity is lower than what we expected. We suspect that we are losing

ions during the ejection towards the MCPs. This can result from the ion cloud not being at the center of the ion trap and therefore not fully aligned with the MCPs, but also from losing ions during the free flight. A detailed analysis is currently being conducted, to ensure that we can reliably record all ions ejected from the crystal.

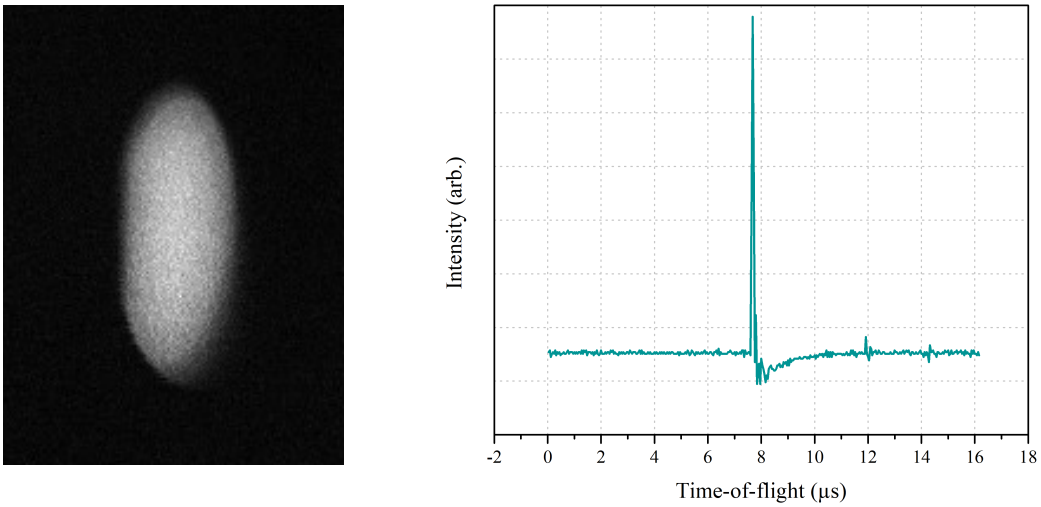

Figure 6.7: Left: Image of a Coulomb crystals obtained in our cryogenic ion trap with the EM-CCD camera at the following parameters: $2V_{\mathrm{RF}} = 100\,\mathrm{V}$ and $U_{\mathrm{end}} = 2\,\mathrm{V}$. Right: ToF trace of the ejected Coulomb crystal as recorded by the MCP detector.

In summary, we have successfully characterised the ToF-MS detection set-up within the cryogenic ion trap. Ca^+ ion signal has been recorded under different sets of experimental conditions; we can observe Ca^+ fluorescence and form Coulomb crystals within the cryogenic ion trap.

For our experiments, we are aiming to obtain sufficient resolution to distinguish between ions that differ in mass by 1 u. To achieve that goal, a new PhD student

and a postdoctoral research associate in our group are working on optimising the potentials applied to the focusing electrodes and ion trap rods, to maximise the detection efficiency and mass resolution of the detector (see an example of a SIMION simulation Figure 6.8 made by Paul Regan).

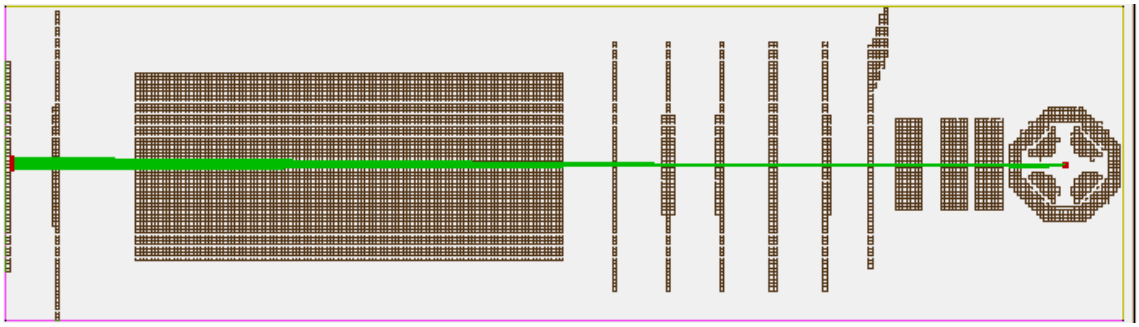

Figure 6.8: Simulation in SIMION of the trajectory of a packet of ions (green lines), ejected from the center of the ion trap (right) towards the MCP detector (extreme left plate). The ions pass though a series of lenses, followed by a flight tube, before reaching the MCP detector. Figure created by Paul Regan.

Chapter 7

Magnetic guide to produce a velocity- and state-selected radical beam

Parts of this chapter are based on work that has previously been published in a Journal of Chemical Physics article by Miossec et al. (2020) [19].

The ultimate goal is for the new cryogenic ion trap (described in the preceding chapters) to be combined with a source of neutral radical species, to study low-temperature ion–radical reaction systems. Our research group has previously developed and characterised a Zeeman decelerator and magnetic guide as a source of state- and velocity-selected radical reactants [113, 114]. This source of radicals has been developed independently of the cryogenic ion trap, with the ion trap apparatus designed so that the existing Zeeman decelerator and guide can be attached to the new chamber. In this chapter, the magnetic guide is operated as a stand-alone radical source. The ability to use the magnetic guide without the Zeeman decelerator will greatly increase the range of ion–radical reaction systems that can be studied with the combined apparatus.

7.1 Operating principle of the magnetic guide

The Zeeman effect, on which the operating principle of the magnetic guide is based, has been detailed in paragraph 1.2.1, along with a description of the Zeeman decelerator. As a reminder, both the Zeeman decelerator and the magnetic guide target only particles in LFS states—that is, particles that exhibit an increase in their Zeeman energy when in a region of high magnetic field. At the end of the Zeeman decelerator, the beam is composed of unwanted species (seed gases, undecelerated H atoms, precursor molecules, and other dissociation fragments) that need to be filtered out before entering the ion trap. That is why the magnetic guide has been built, to filter out the unwanted species from the beam exiting the Zeeman decelerator (see Figure 7.1).

In addition to removing unwanted species, the magnetic guide also plays a role in velocity-filtering the beam. Previous work has demonstrated that the magnetic guide can remove all non-target species from the beam exiting the Zeeman decelerator. Here, we show that the magnetic guide can also be employed as a stand-alone device, transmitting the target particles from the initial distribution (i.e., without the need to first decelerate the beam). This will enable us to study a more diverse range of ion–radical reactions in the cryogenic ion trap; while the Zeeman decelerator has been designed to decelerate H atoms (as few other radicals possess a sufficiently high magnetic moment-to-mass ratio and our decelerator is short), the ability of the guide to operate independently of the decelerator will open up a significantly broader range of potential reaction systems.

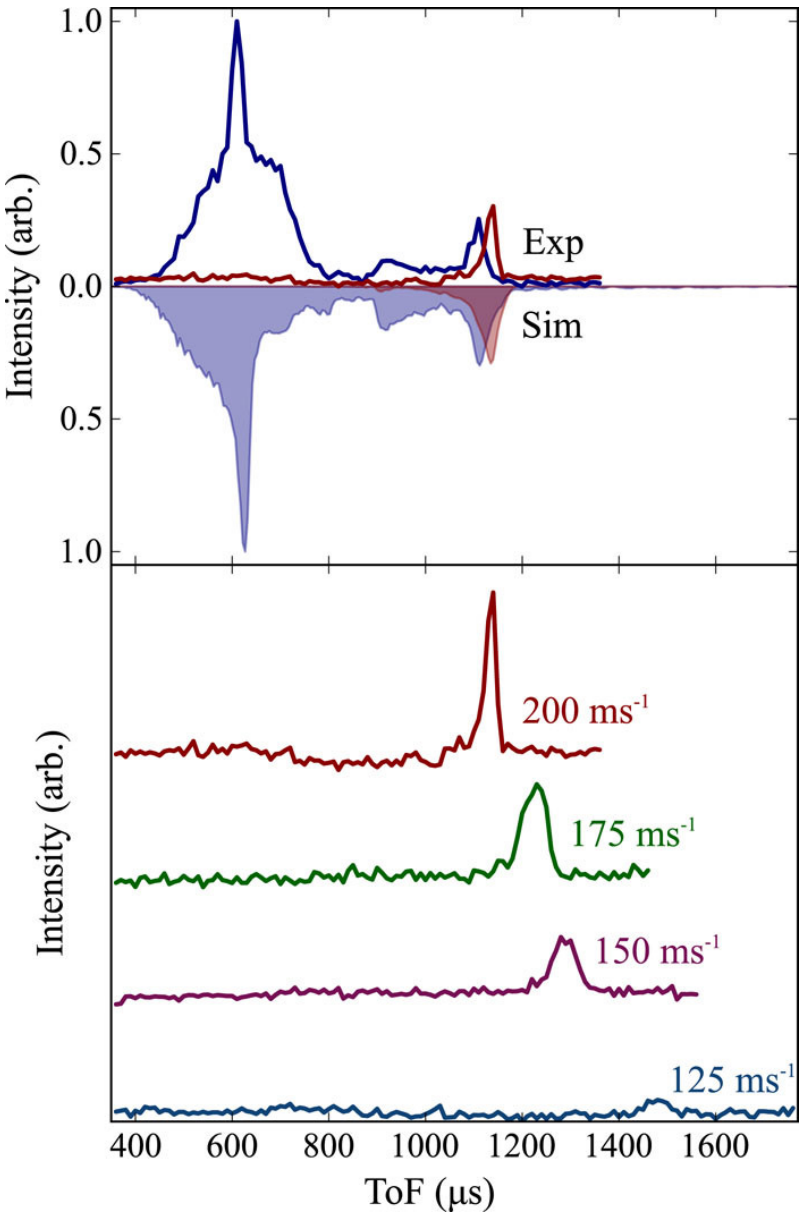

Figure 7.1: Top panel: experimental (lines) and simulated (shaded) ToF traces of H atoms (first decelerated to 200 m s^{-1}) detected after passing through the magnetic guide (red traces) and when no guide is in place (blue traces). When the magnetic guide is in place, only the fully decelerated particles (the peak furthest on the right) are detected. Bottom panel: experimental ToF traces when the magnetic guide parameters are optimised for different target velocities. The undecelerated particles are no longer present at the detector region. Reproduced from J. Toscano et al., J. Chem. Phys. 149, 174201 (2018) [113], with the permission of AIP Publishing.

In summary, the magnetic guide can operate independently of the Zeeman decelerator and can be adapted (for example, by swapping the magnets in the Halbach arrays) to target different radicals and different velocities. The first results from the operation of the magnetic guide as a stand-alone device are provided below.

7.2 Description of the magnetic guide

The design of a magnetic guide is based on an arrangement of permanent multipole magnets that was first set out by Halbach in a theory paper [115]. The construction of a curved guide containing an assembly of multipole magnets was experimentally achieved in 1999 [116, 117]. In these examples, a series of Halbach arrays were positioned so as to "guide" the target radicals around the bend; non-paramagnetic species are not confined by the magnetic fields, and so did not follow the bend and were lost from the beam. In our laboratory, the magnetic guide is designed such that, by amending the height of the guide components using the actuators, a line-of-sight can be achieved through the various elements. This is very helpful for alignment and characterisation purposes.

Our magnetic guide is composed of four hexapole magnets arranged in an Halbach array configuration (see Figure 7.2) and two skimming blades. By looking at the deflection that could be achieved using only one Halbach array, a former PhD student in our group has looked at the difference in the deflection of the beam from shifting or tilting the Halbach array. The principle of this study is shown in Figure 7.3, with the representation of the Halbach array with its center aligned with the center of the beam exiting the Zeeman decelerator in a), with a tilting

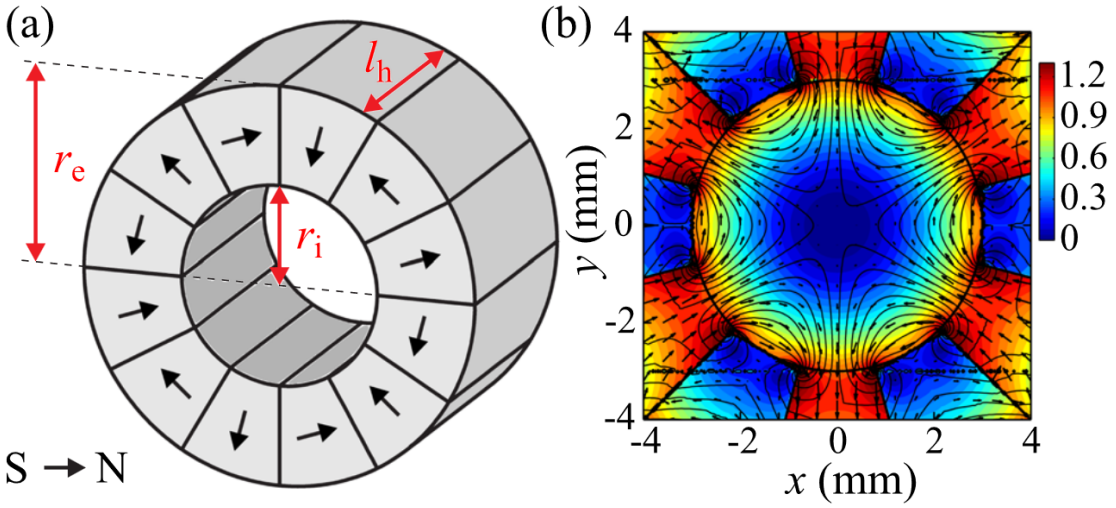

Figure 7.2: a) Schematic illustration of one Halbach array, composed of a series of permanent magnets in a hexapolar configuration. b) Map of the magnetic field magnitude (in Tesla) of an Halbach array in the x–y plane, calculated using Radia. Reprinted from J. Toscano et al., J. Chem. Phys. 149, 174201 (2018) [113], with the permission of AIP Publishing.

of the Halbach array in b) and with the center of the Halbach array shifted up compared with the center of the beam in c). It was found that the maximum displacement of the beam with tilting the Halbach array is lower than what is achievable with shifting it. Additionally, it was experimentally observed that the beam is more dispersed after the titled Halbach array than after the shifted one [118].

Therefore, the Halbach arrays are positioned along the beam axis and shifted off the main axis to displace the beam off this axis. The arrays are arranged in pairs, with a skimming blade positioned after each pair, schematised in Figure 7.4. The blades are put beyond the beam axis to break the direct line-of-sight from the source to the detector [19, 113]. A series of linear actuators allow the variable

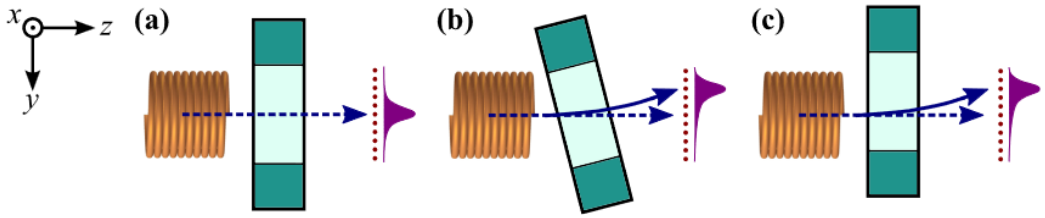

Figure 7.3: Side views of the relative position of only one Halbach array, and the trajectories of the deflected (solid line arrow) and undeflected (dashed line arrow) beams, when it is a) perfectly aligned, b) tilted and c) shifted, with respect to the final decelerator coil (in orange), and a schematic of their respective intensity profiles (purple) obtained. Reprinted from J. Toscano et al., Review of Scientific Instruments 90, 033201 (2019), with the permission of AIP Publishing [118].

parameters—the amount of shift of each pair of arrays and each blade from the main axis, and the separation between pairs of arrays, all shown in Figure 7.6—to be manipulated in real time, while the apparatus is kept under vacuum.

The operating principle of our magnetic guide is to divert a beam of target radicals away from the beam axis, around the first skimming blade, and back to the beam axis with this process then repeated for the second pair of arrays and the second skimming blade. Non-target species are either blocked by the skimming blades (as, when in guiding configuration, there is no line-of-sight through the guide) or are over-focused and deflected away from the main beam axis. This ensures that a state-selected and velocity-selected beam of radicals is produced. A schematic illustration of the magnetic guide is provided in Figure 7.4.

The Zeeman decelerator and magnetic guide in our laboratory have been constructed to guide hydrogen atoms formed by photolysis of supersonically-expanded

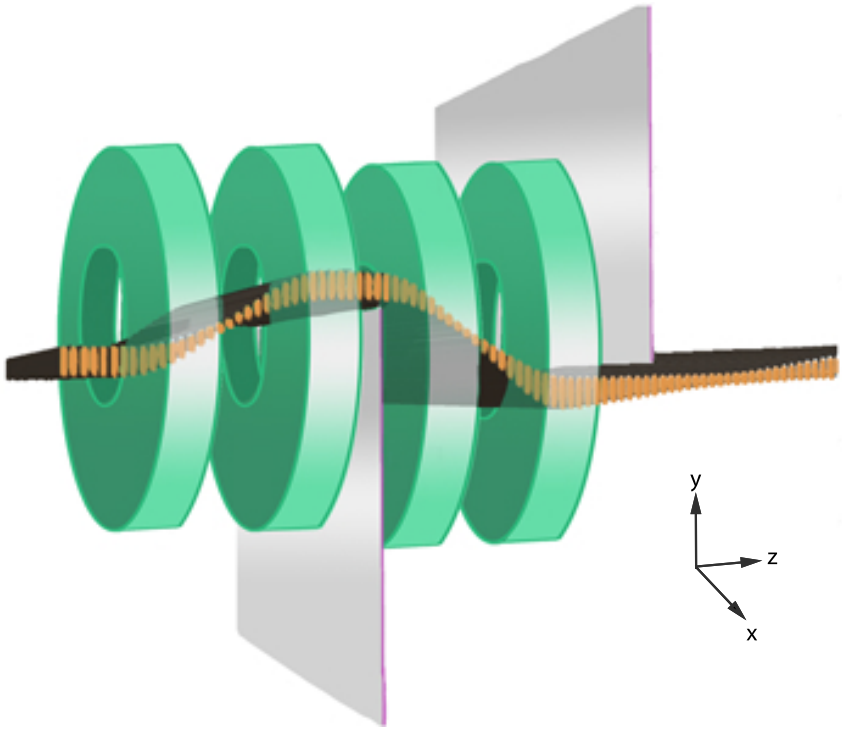

Figure 7.4: Schematic illustration of the magnetic guide. The Halbach arrays are represented by green cylinders, and the skimming blades are indicated in silver. The orange beam represents the typical trajectories of target particles through the guide; target H atoms are deflected and collimated by each pair of arrays, and avoid the skimming blades. Reprinted from C. Miossec et al., J. Chem. Phys. 153, 104202 (2020) [19], with the permission of AIP Publishing.

NH_3 seeded in Kr. The target H atoms are in the 1s $^2S_{1/2}$ ground electronic state. In the presence of an external magnetic field, the energy levels of H atoms are split by the Zeeman effect, giving rise to two LFS states ($F = 1$, $m_F = +1, 0$) and two HFS states ($F = 0; F = 1$, $m_F = -1$), where F is the total angular momentum and m_F is the projection of F onto the external magnetic field axis (see Figure 7.5). The properties of the Halbach arrays (12-segment NdFeB magnets with a remanence $B_0 = 1.4$ T, internal radius $r_i = 3$ mm, external radius $r_e = 7$ mm, and

thickness $l_h = 7$ mm) are appropriate for guiding H atoms with velocities spanning 200 to 355 $\mathrm{m\,s^{-1}}$.

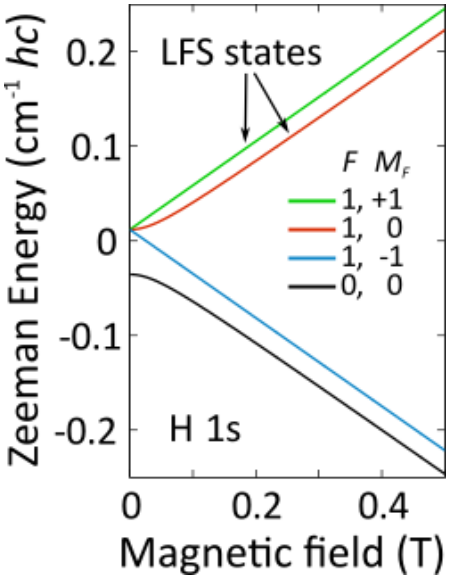

Figure 7.5: Zeeman splitting for $1^2S_{1/2}$ hydrogen atoms, with the LFS states indicated. Reproduced from Jutta Toscano's thesis [32].

We want to determine the optimal configuration of the different elements in the guide so that we can achieve both a narrow velocity distribution in the post-guide beam and a high number of state-selected radicals. The parameters that we are tuning are shown Figure 7.6. The first array from the left deflects the slow particles up, the second collimates the deflected beam, the third brings it back to the beam axis, and the fourth array collimates the beam again. The distance between the midpoints of the first two and that of the second two arrays is twice the focal length, $2f$ [113].

The distance of the pairs of Halbach arrays from the beam axis center is altered (the displacement of the first and second pairs are referred to as s12 and s34, respectively), as well as the distance of the top of the skimming blades from the beam axis (noted b1 and b2), with all of these parameters able to be adjusted using actuators located outside of the chamber. We can see how increasing the extent to which the blades penetrate the beam axis increases the velocity selectivity of the guide, at the expense of the intensity of the transmitted beam. Finally, we can modify the separation of the Halbach arrays within each pair, that corresponds to a distance of $2f$, in order to transmit different velocities. The optimal configuration of all the guide elements for preferentially transmitting the target H atoms is determined using three-dimensional particle trajectory simulations.

The principle of the velocity-filtering by the magnetic guide is shown in Figure 7.7 alongside the simulated trajectories of particles as they travel through the guide. The top panel shows the trajectory of LFS H atoms travelling at a target velocity of $350\,\mathrm{m\,s^{-1}}$. The middle and bottom panels show the trajectories of H atoms travelling at faster and slower velocities, respectively. The grey area on the right-hand side corresponds to the detector position—where the ion trap will be located in our combined set-up—and is set as a circle of 1.3 mm radius in the simulations (to model the laser-based detection method).

A significant proportion of target particles can be seen to successfully traverse the guide, be deflected, collimated, deflected, and collimated again before reaching the detector. Most of the particles travelling at faster velocities can be seen to be

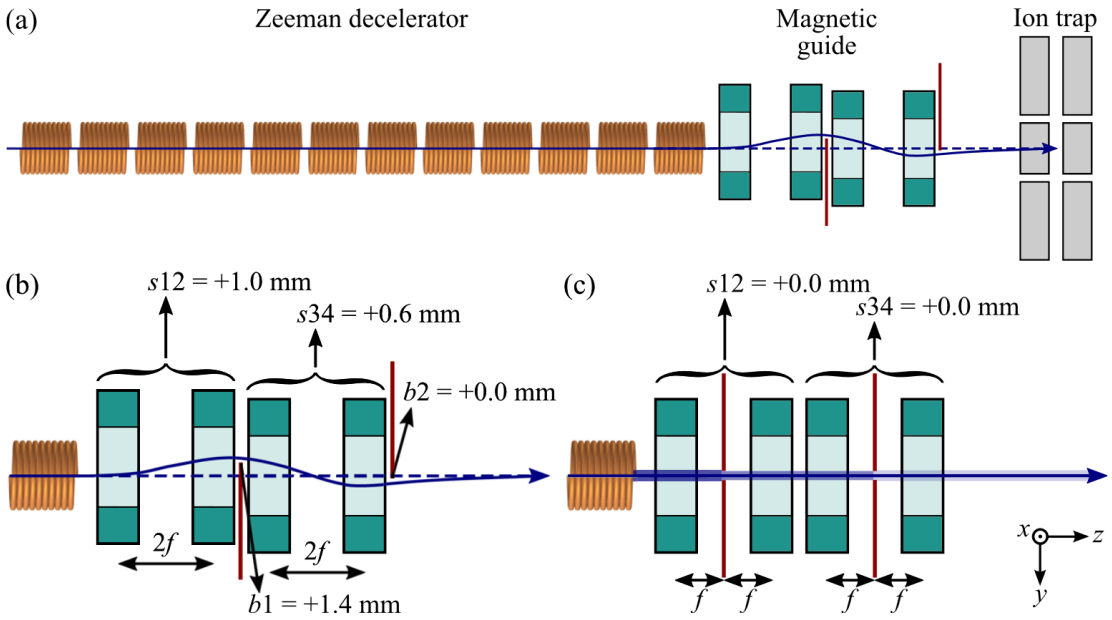

Figure 7.6: a) Schematic illustration of the combined Zeeman decelerator (with the solenoid coils in orange), magnetic guide (with the Halbach array cross section in green, and the skimming blades in red) and the ion trap (grey). The solid blue arrow represents the trajectory of the deflected particles, and the dashed blue line represents the trajectory of the undeflected particles. b) A close up of the magnetic guide in position. The pairs of Halbach arrays are shifted in the vertical axis: s12 = +1.0 = mm offset for the first two Halbach arrays and s34 = +0.6 mm for the second two arrays. b1 and b2 indicate the amount that the end of the first and second skimming blades penetrate the beam axis, respectively. $2f$ is the distance between the midpoint of the two arrays of a pair, where f is the focal length of the Halbach array, for a selected target species and velocity. c) The magnetic guide is shown with all elements aligned with the beam axis. The particles go through the Halbach arrays without being deflected. The red lines represent pinholes. The blue arrow represents the trajectories of all particles whilst the superimposed shaded lines represent the gradual decrease in the number of faster-moving particles. While it is possible to preferentially focus the LFS species of interest through the pinholes other non-target species also travelling along the beam axis are not removed, resulting in a lower beam purity at the end of the guide. Reprinted from J. Toscano et al., J. Chem. Phys. 149, 174201 (2018) [113], with the permission of AIP Publishing.

cut off by the blades, with those that make it past the blades not reaching the detector. Slower particles are deflected away or collide with the blades and the Halbach arrays and do not reach the detector region either. The penetration of the blades through the beam axis removes the line-of-sight through the guide, ensuring that species that are not affected by the magnetic fields (such as seed gases) do not reach the detection region.

We have conducted two sets of experiments with the guide as a stand-alone device, targeting LFS H atoms with target velocities of 300 ± 10 m s^{-1} and 350 ± 10 m s^{-1}. The target H atoms are focused at $f = 12.4$ mm and 9.4 mm, respectively. The other parameters of the two magnetic guide configurations are unchanged, except for a minor (0.1 mm) difference in the vertical offset of the second pair of Halbach arrays. The settings of the magnetic guide with respect to the center beam line are $s12 = 1.5$ mm, $s34 = 0.6$ mm, $b1 = 1.1$ mm, $b2 = -0.2$ mm (see Figure 7.4 for the definition of the parameters).

7.3 Successful magnetic filtering of the beam

H atoms that successfully traverse the guide and reach the detection region can be ionised using a (2+1) REMPI scheme, using the 243 nm output of a frequency-doubled pulsed dye laser. Without the magnetic guide in place, the beam is broad and peaks at around 570 µs (see Figure 7.8).

Figures 7.8 and 7.9 show the experimental ToF traces (top) of H radicals with

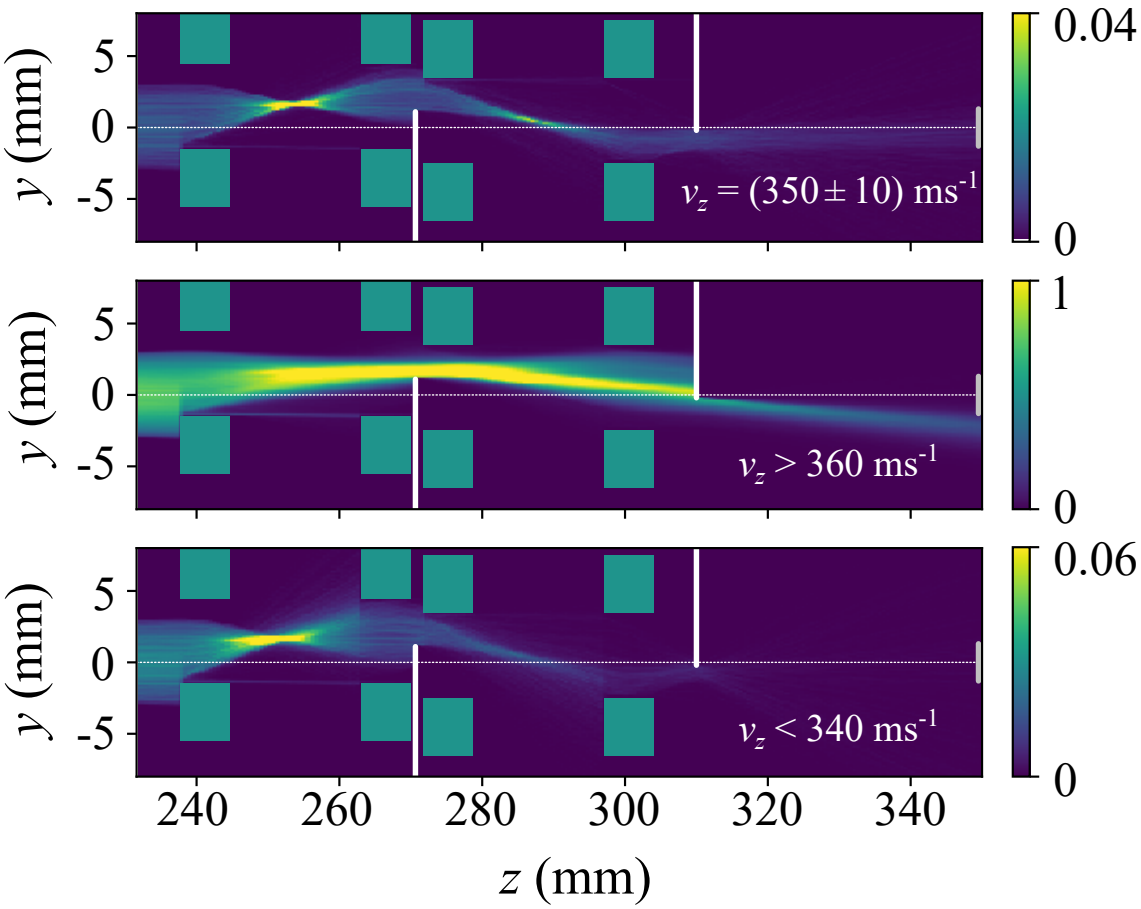

Figure 7.7: Three-dimensional particle trajectory simulations of a beam of state-selected H atoms travelling through the magnetic guide (its cross section represented by the green squares and the white lines). The top panel shows the trajectories of LFS H atoms travelling at the target velocity 350 ± 10 m s^{-1}. The middle and lower panels show the trajectories of H atoms travelling at faster and slower velocities than the target velocity range, respectively. The colour bars indicate the relative intensities of the particles. At $z = 350$ mm, the small grey region indicates the detection region. Reprinted from C. Miossec et al., J. Chem. Phys. 153, 104202 (2020) [19], with the permission of AIP Publishing.

and without the magnetic guide in place, compared with the simulated ToF traces reflected below. In both cases, the experimental and simulated traces are in good agreement. When the guide is in place, the distribution is narrower, and arrives later, centered at around 750 µs instead of the 570 µs when the guide is not in place. The slower arrival time and lower intensity is in line with our expectations; we are filtering a subset of the initial beam, targeting only LFS particles travelling at a particular velocity. We can also see a decrease in the intensity of the peaks between the trace targeting particles travelling at $350\,\mathrm{m\,s^{-1}}$ and those travelling at $300\,\mathrm{m\,s^{-1}}$, with the later being less intense. This last point comes from the fact that there are fewer particles in the initial beam travelling at the lower velocity, therefore the peak will be less intense.

The efficiency of the guide in transmitting the target species—and removing faster and slower H atoms—can be ascertained from simulations. The trajectories of species travelling through the guide set to target H atoms with a velocity of $300\,\mathrm{m\,s^{-1}}$ have been analysed, with the findings presented in Table 7.1. Note that LFS H atoms travelling with a velocity of $300 \pm 10\ \mathrm{m\,s^{-1}}$ are classified as target particles. Faster particles travel at velocity $\geq 310\,\mathrm{m\,s^{-1}}$ and slower particles are particles travelling at $\leq 290\,\mathrm{m\,s^{-1}}$.

What is immediately striking is that the faster particles account for 98 % of the total number of particles in the unguided beam reaching the detector, with the target and slower particles only accounting for 1 % each. When the guide is in place, the vast majority of faster and slower particles are removed: 99% of faster

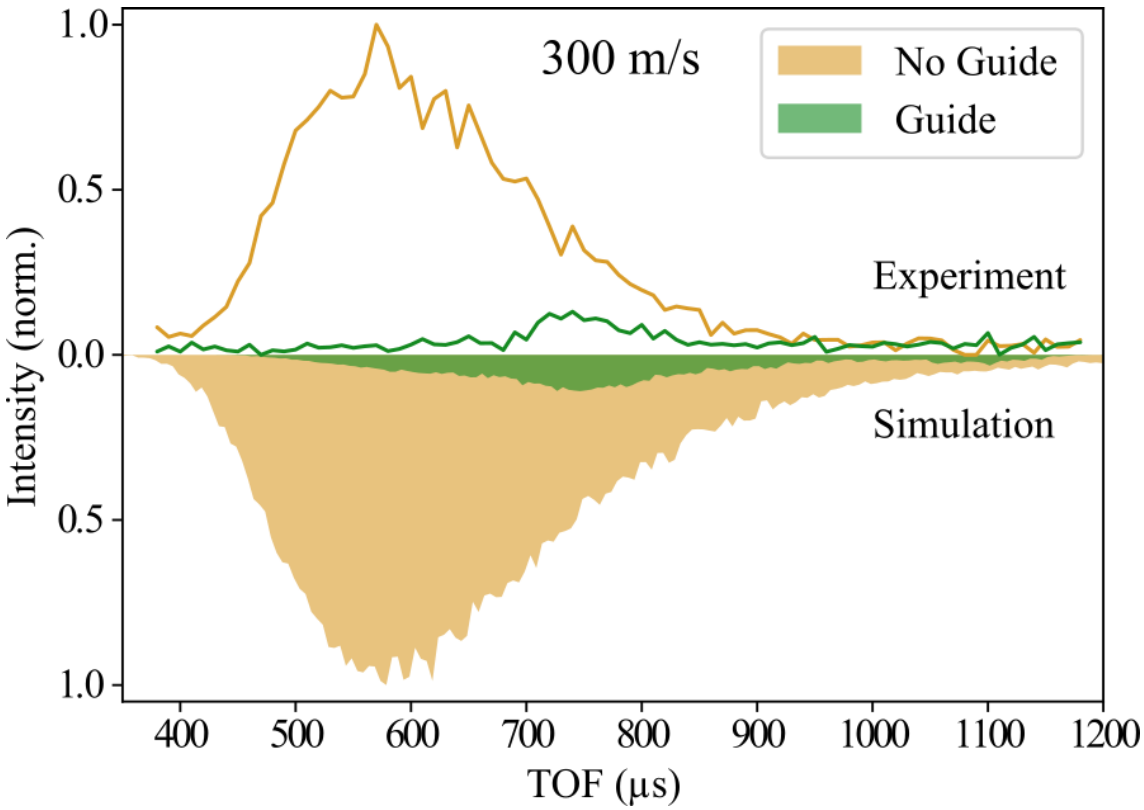

Figure 7.8: Experimental and simulated ToF traces for the H atoms that successfully reach the detection region. It depicts the ToF profile recorded without the magnetic guide ("No Guide") and with the magnetic guide in place ("Guide"), for a target velocity of 300 m s^{-1}. Reprinted from C. Miossec et al., J. Chem. Phys. 153, 104202 (2020) [19], with the permission of AIP Publishing.

particles and 96% of slower particles are filtered out of the beam by the guide. There are still some non-target species in the final beam, as can be seen from Table 7.1 (a). Indeed, with these simulation parameters, faster-than-target particles make up 57% of transmitted H atoms; slower particles make up only 2% of the beam. This is due to the narrow definition of "target" species (arbitrarily chosen to be 300 ± 10 m s^{-1}) and the choice of guide parameters. Higher beam purity can be achieved, but this comes at the expense of particle numbers. This explains why the

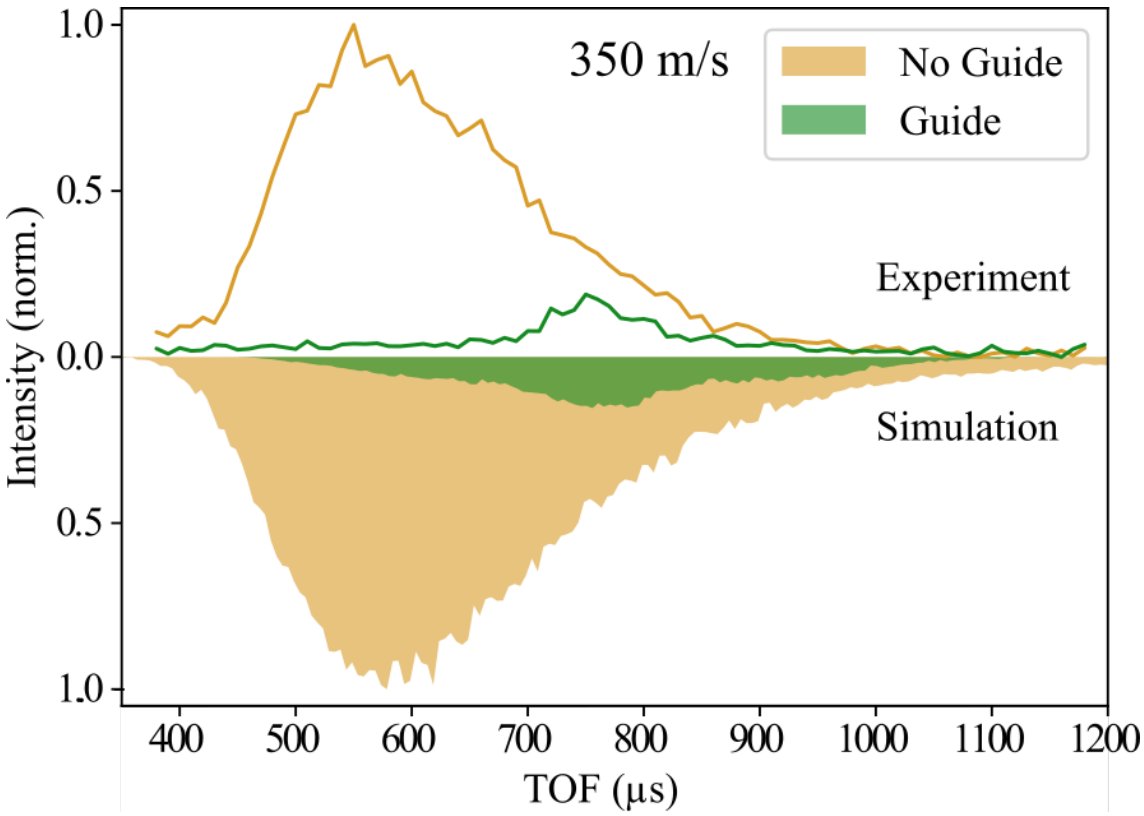

Figure 7.9: Experimental and simulated ToF traces for the H atoms that successfully reach the detection region. It depicts the ToF profile recorded without the magnetic guide ("No Guide") and with the magnetic guide in place ("Guide"), for a target velocity of 350 m s^{-1}. Reprinted from C. Miossec et al., J. Chem. Phys. 153, 104202 (2020) [19], with the permission of AIP Publishing.

average velocity of the beam is 394 ± 43 and 350 ± 55 m s^{-1} respectively for target velocities of 350 m s^{-1} and 300 m s^{-1}.

Looking at the distribution of the target and non-target H atoms on the detector, shown in Figure 7.10, we can clearly see that, when the guide is not in place, there is a symmetric distribution for the target, slower and faster particles; with the magnetic guide in place, only target particles have a symmetric distribution. It can

Table 7.1: The relative amounts of target ($300 \pm 10\,\mathrm{m\,s^{-1}}$), slower ($< 290\,\mathrm{m\,s^{-1}}$) and faster ($> 310\,\mathrm{m\,s^{-1}}$) H atoms that reach the detection region with and without the magnetic guide in place is shown. Reprinted from C. Miossec et al., J. Chem. Phys. 153, 104202 (2020) [19], with the permission of AIP Publishing.

% of H atoms	Target	Slower	Faster
In transmitted beam (no guide)	1%	1%	98%
In transmitted beam (with guide)	40%	3%	57%
Removed from the beam (with guide)	10%	96%	99%

be seen that the faster particles are directed towards the lower part of the detector, as shown in Figure 7.7 on the middle panel, and the slower particles are directed to the higher part of the detector. This indicates that amendments could be made to future guide designs, to achieve even higher beam purity in the future.

In summary, the results and simulations clearly illustrate that the magnetic guide can preferentially transmit target particles, removing the majority of non-target species from the beam, even when operated as a stand-alone device. The purity of the beam can be increased by, for example, increasing the overlap of the skimming blades, thereby removing more of the faster species from the beam. This comes at the expense of beam density, with some target particles also removed from the beam. The versatility of the device is also very important; by tuning the distance between the two Halbach arrays, it has been demonstrated that H atoms travelling at different velocities can be targeted, enabling the role of collision energy to be studied in ion–radical reactions once the magnetic guide is combined with the ion trap apparatus.

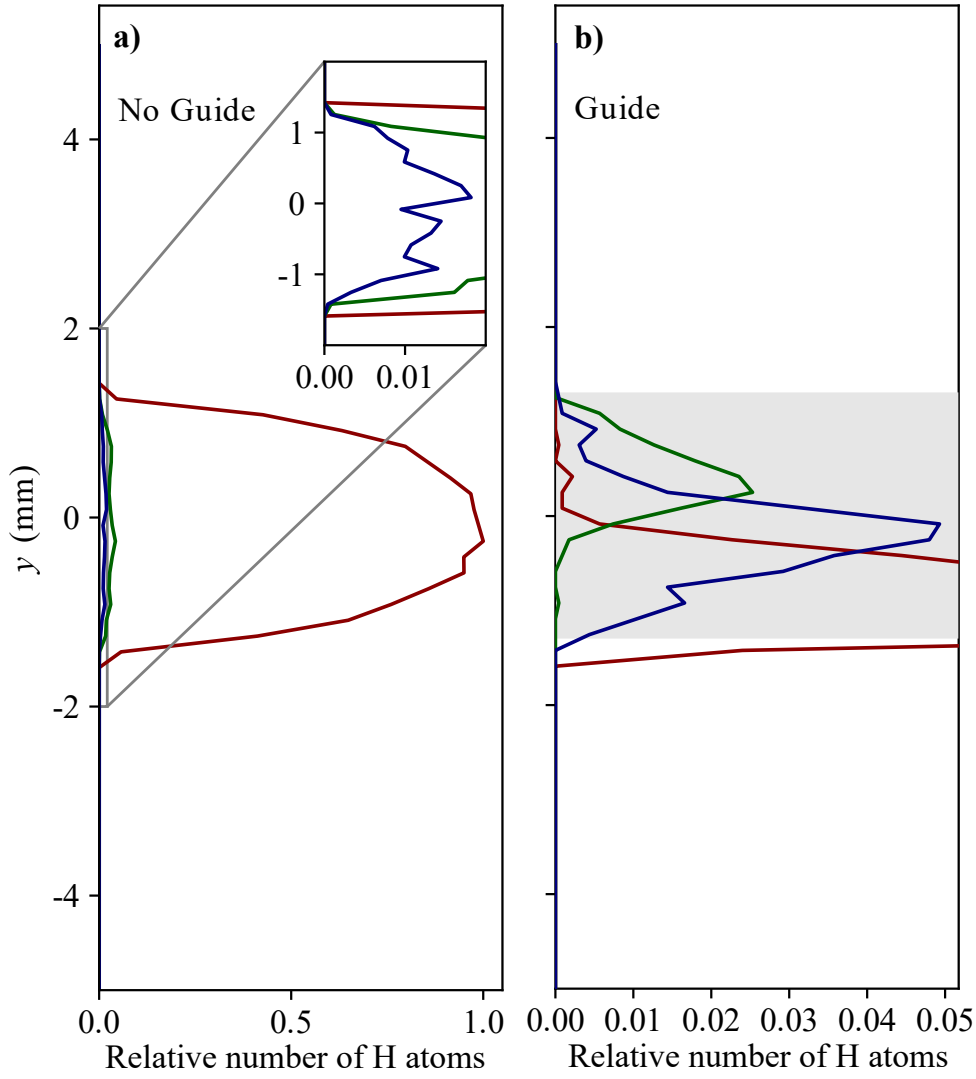

Figure 7.10: Simulated distribution of the H atom beam at the detection region, plotted along the vertical y–axis, a) without and b) with the magnetic guide in place. The initial beam of H atoms is centred at $y = 0\,\text{mm}$. The vast majority of particles in the non-guided beam are travelling faster than the target velocity, as depicted by the dark red trace. The blue traces represent the distribution of the target species (with a velocity of $350 \pm 10\,\text{m}\,\text{s}^{-1}$). Particles travelling with a velocity below the target range are shown in green. The detection region (defined to match the acceptance of the ion trap) is simulated as a circle with radius 1.3 mm, indicated by the shaded region in plot b). Reprinted from C. Miossec et al., J. Chem. Phys. 153, 104202 (2020) [19], with the permission of AIP Publishing.

7.4 Limits of magnetic guide and perspective

It has been experimentally demonstrated that a magnetic guide can filter the state-selected H atoms of interest from all other components of a beam. No other species——H atoms in non-guided states, or other contaminant species present in the initial beam——are transmitted through to the detection region. The magnetic guide also preferentially transmits H atoms travelling at a selected target velocity.

This last point can be ameliorated: even though the guide removes some 99% of H atoms in LFS states travelling faster than the target species, these faster radicals represent the vast majority of H atoms in the initial distribution. As such, the 1% of faster LFS hydrogen atoms that make it to the target region affect the final velocity distribution. Straightforward amendments could be made to a second-generation magnetic guide. For example, an additional focusing element could be introduced before the guide; the length of the guide could be extended (so that the same amount of deflection achieves a larger separation of velocities); an additional element such as an iris could be placed in front of the detection region.

While one of the main drawbacks of the magnetic guide is the small number of particles that arrive at the detector, this does not necessarily pose a problem for our experiment. Our ionic reactant is trapped and the reaction takes place over an extended period of time, which means that we do not require a high-density beam to observe and study reactions. This makes the magnetic guide ideal to combine to a stationary target—here an ion trap—to examine gas-phase reactions including radicals.

The experimental results are supported by particle trajectory simulations, enabling the properties of the filtered beam to be evaluated. This work presents the first experimental evidence that the magnetic guide can operate as a stand-alone radical beam filter.

Our calculations indicate that the magnetic guide could be utilised to generate state-selected low-velocity beams of a range of other radical species, such as OH molecules, by including Halbach arrays with different properties. Currently, a PhD student in our group has designed and is testing a second-generation magnetic guide (specifically designed to operate as a stand-alone device). This new generation guide will target O and OH radicals and is composed of 8 Halbach arrays (arranged in 4 pairs), increasing the transmissibility of radicals with a less favourable magnetic-moment-to-mass ratio than H.

Chapter 8

Conclusion and future work

This thesis reports the design, construction, and characterisation of a cryogenic linear Paul ion trap chamber. Temperatures below 10 K are achieved in the innermost (ion trap) region of the chamber. The apparatus has been designed to accommodate optical access for lasers and for imaging of the crystals. Vibrations have been minimised, thanks to the creation of a dual-frame structure and the inclusion of a Heim column. A new OAP mirror-based imaging relay has been shown to successfully image Coulomb crystals under cryogenic conditions. Complementing the imaging analysis of the crystals, time-of-flight measurements have been successfully recorded to quantitatively establish the contents of the ion trap at selected ejection times. This apparatus is the first cryogenic ion trap designed for the study of reactions in Coulomb crystals, with in-built imaging and ToF detection capabilities.

By having a cryogenic ion trap that can achieve temperatures of less than 10 K, we can trap and keep molecular ions in selected quantum states. This is due to the reduction of 300 K BBR at the ion trap region, limiting BBR-induced population redistribution in molecular ions and enabling quantum state selectivity to be preserved for the duration of reaction studies. While we have demonstrated how the design

choices were adequate to obtain temperatures $< 10\,\mathrm{K}$ in the ion trap region, we still need to experimentally confirm that the state selectivity of trapped molecular ions can be maintained. By using a REMPD scheme, one could probe the state selectivity of molecular ions, such as NH_3^+, and monitor their population distribution over time. Similar measurements have already been undertaken for MgH^+ in the original CryPTEx apparatus, with the rotational state distribution characterised by temperatures as low as 7.6 K [79]. Performing REMPD measurements of molecular ions in the cryogenic ion trap is one of the next steps that will be taken with the set-up. Determining a REMPD scheme for NH_3^+ is work that is currently underway.

Alongside the cryogenic ion trap for confining of quantum state-selected molecular ions, a source of radicals has also been described. We have shown how a magnetic guide can produce not only a state selected, but also a velocity-selected beam of radicals. The magnetic guide described here can be used with a Zeeman decelerator to obtain an even narrower velocity range.

After this successfully study, another magnetic guide is in the process of being developed by a PhD student in our group. This second generation magnetic guide has four pairs of magnets, enabling O, O_2, and OH radicals to be targeted (see Figure 8.1). The magnetic guide is a versatile radical beam filter, and, when combined with the cryogenic ion trap, will enable a range of reaction systems to be studied under cold and controlled conditions. Having so much control over both the ionic and the radical reactants will enable us to obtain important information both on the kinetics and the dynamics of reactions.

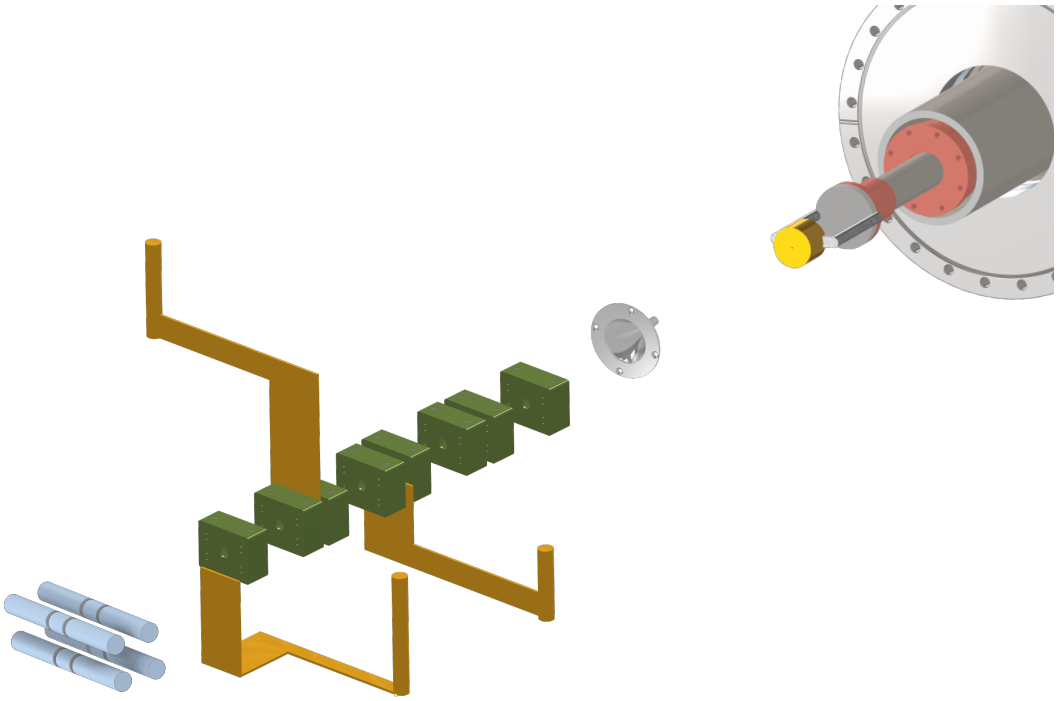

Figure 8.1: Schematic illustration of the second generation magnetic guide being tested in our laboratory. The Halbach arrays are depicted in dark green, with the four pairs visible (the distance between two arrays in a pair is bigger than the distance between two pairs), and the skimming blades are depicted in brown. The beam of O_2 is produced by the Even-Lavie valve (visible on the right-hand side), before passing through the skimmer (silver), and then through the magnetic guide before reaching the ion trap (in light blue on the left-hand side). The ion trap depicted here is the room-temperature ion trap to which the new generation magnetic guide is going to be combined with in the first instance. Figure created by L.Y. Wu.

Previous work, carried out by our group, and by other research groups in the field, has demonstrated that reaction kinetics and dynamics measurements can be undertaken using Coulomb crystals. The imaging of the crystals in the cryogenic ion trap has been made possible thanks to the new imaging system that has been

described in this work. We have tested vibrations at the ion trap and overcome the challenges that the vibrations coming from the cryocooler were posing, so that they did not have an impact on the level of resolution we required to record Coulomb crystals. We have observed Coulomb crystals with resolution that can distinguish individual ion lattice positions.

Complementing our ability to observe reactions by imaging the Ca^+ fluorescence, we are also able to study the dynamics of ion–radical reactions with the help of the ToF-MS. This important part of our apparatus makes it a unique machine to study state-selected ion–radical reactions both dynamically and kinetically. By using the ToF-MS to quantitatively detect reaction products at a range of reaction times, one can look at branching ratios of products over time in addition to complementing the kinetics measurements that can be conducted by imaging. The aim of distinguishing between isotopes, i.e. obtaining a resolution of 1 m/z on the ToF traces, has been tested. While we can distinguish the different isotopes of Ca^+ with the current set-up, we believe that it should be possible to achieve an even better resolution. For that, we need to find a combination of voltages that can be applied to the ion optics in order to optimise the signal reaching the detector. This is ongoing work being carried out by a PhD student in our group.

Following the final characterisation measurements described above, we will study the test reaction $NH_3^+ + NH_3 \rightarrow NH_2 + NH_4^+$ in the new cryogenic ion trap. This reaction will enable us to test the optical system, and also the resolution of the ToF-MS. As both NH_3^+ and NH_4^+ are lighter than Ca^+, we cannot monitor

the reaction by imaging alone. Both NH_3^+ and NH_4^+ (that is, both the reactant and product ions) will be located in the dark core of the crystal, prohibiting us from monitoring the reaction by observing the change in the fluorescence pattern throughout the reaction. This is why the time-of-flight approach is so important. The difference of 1 m/z ratio between NH_3^+ and NH_4^+ will be a stringent test of our current resolution and provide a way to test approaches to improve this resolution further.

In order to extract rate coefficients for this test reaction, we are planning to determine the beam density of our NH_3 beam, a measurement that is known to be complicated. We shall determine it using ionisation yields in non-resonant strong-field ionisation, following the same procedure as explained in Kilaj et al. [119].

In addition to providing a stringent test for out ToF-MS detection capabilities, the reaction $NH_3^+ + NH_3 \rightarrow NH_2 + NH_4^+$ offers other benefits. For example, we will be able to test the accuracy of capture theory models in describing the process. We can alter where energy is located in this system, by generating internally cold and internally 300 K molecular ions (i.e., studying them under both cryogenic and room temperature conditions). We also have methods for manipulating the collision energy and internal state distribution of the polar molecules, by modifying the properties of the molecular beam. Capture theories treat the ionic species as a point charge, whereas we know that there are several vibrational modes in NH_3^+ that may play a role in the reaction. As such, the reaction should enable us to test both our apparatus and to challenge the validity of existing theories of reactivity.

Finally, one or both of the reactants could be deuterated, allowing us to explore isotope effects in the reaction system.

Beyond this test study, the objective is then to look at ion–radical reactions. One such system we can look at is the reaction of $N_2^+ + H$. H is the most abundant species in the universe, and both N_2^+ and the adduct ion, N_2H^+, have been detected in the ISM, making this reaction astronomically relevant [120]. This would also be a test study, as N_2^+ is a diatomic ion—therefore does not have a dipole moment—that will not be impacted by the BBR spectrum. The first reaction that we want to study to use the cryogenic capabilities of the ion trap is $CO_2^+ + H$. The CO_2^+ ions would be impacted by BBR and therefore preserved from thermalization in the cryogenic ion trap. This will allow us to study state selected CO_2^+ throughout the reaction time, with state and velocity-selected H radicals.

Both reactions of N_2^+ and CO_2^+ with H atoms (and with D atoms) have been studied experimentally before. There have been at least eight experimental studies of N_2^+ with H and D atoms, all conducted at room temperature, with these studies reporting either very low reaction rate coefficients ($< 1.00 \times 10^{-11}$) or no reaction [121,122,123]. The $CO_2^+ + H$ reaction has also been studied experimentally at room temperature [122,123,124,125,126], but results diverge regarding both the branching ratios and the reaction rates. A more recent study employed a 22-pole ion trap to investigate the reaction between CO_2^+ and H at ion temperatures ranging from 15 to 300 K [127]. However, the measured rate coefficient obtained using

the $AB - 22PT$ set-up exhibits significant uncertainties. In particular, despite integrating multiple differential pumping stages in this set-up, the insufficient removal of contaminant precursor molecules (H_2) results in a competing process, as they react faster with $CO_2{}^+$. Therefore, additional experimental measurements at low temperatures are needed.

The cryogenic ion trap apparatus presented in this work is a truly unique apparatus. It will enable us to study a larger range of state-selected molecular ions, which, through reactions with velocity- and state-selected radicals from the magnetic guide, can lead to new knowledge on fundamental reaction dynamics and kinetics.

Bibliography

[1] Lok Yiu Wu, Chloé Miossec, and Brianna R. Heazlewood. Low-temperature reaction dynamics of paramagnetic species in the gas phase. *Chemical Communications*, 58(20):3240–3254, March 2022.

[2] Brianna R. Heazlewood and Timothy P. Softley. Low-Temperature Kinetics and Dynamics with Coulomb Crystals. *Annual Review of Physical Chemistry*, 66(1):475–495, April 2015.

[3] Martin T. Bell and Timothy P. Softley. Ultracold molecules and ultracold chemistry. *Molecular Physics*, 107(2):99–132, January 2009.

[4] Xin Xu, Jun Chen, Xiaoxiao Lu, Wei Fang, Shu Liu, and Dong H. Zhang. Strong non-Arrhenius behavior at low temperatures in the OH + HCl $\rightarrow$ H_2O + Cl reaction due to resonance induced quantum tunneling. *Chemical Science*, 13(26):7955–7961, 2022.

[5] M. Fournier, S. D. Le Picard, and I. R. Sims. CHAPTER 1:Low-temperature Chemistry in Uniform Supersonic Flows. In *Cold Chemistry*, pages 1–45. Royal Society of Chemistry, December 2017.

[6] Ian R. Sims. Tunnelling in space. *Nature Chemistry*, 5(9):734–736, September 2013.

[7] Robin J. Shannon, Mark A. Blitz, Andrew Goddard, and Dwayne E. Heard. Accelerated chemistry in the reaction between the hydroxyl radical and methanol at interstellar temperatures facilitated by tunnelling. *Nature Chemistry*, 5(9):745–749, September 2013.

[8] Tiangang Yang, Long Huang, Chunlei Xiao, Jun Chen, Tao Wang, Dongxu Dai, Francois Lique, Millard H. Alexander, Zhigang Sun, Dong H. Zhang, Xueming Yang, and Daniel M. Neumark. Enhanced reactivity of fluorine with para-hydrogen in cold interstellar clouds by resonance-induced quantum tunnelling. *Nature Chemistry*, 11(8):744–749, August 2019.

[9] Brianna R. Heazlewood and Timothy P. Softley. Towards chemistry at absolute zero. *Nature Reviews Chemistry*, 5(2):125–140, January 2021.

[10] Dongdong Zhang and Stefan Willitsch. Cold Ion Chemistry. In *Cold Chemistry: Molecular Scattering and Reactivity Near Absolute Zero*. The Royal Society of Chemistry, 12 2017.

[11] S. K. Dhaka and Vinay Kumar. Chapter 1 - Composition and thermal structure of the earth's atmosphere. In Abhay Kumar Singh and Shani Tiwari, editors, *Atmospheric Remote Sensing*, Earth Observation, pages 1–18. Elsevier, January 2023.

[12] Ian W. M. Smith and Peter W. Barnes. Advances in low temperature gas-phase kinetics. *Annual Reports Section "C" (Physical Chemistry)*, 109(0):140–166, 2013.

[13] Eric Herbst and Tom J. Millar. The Chemistry of Cold Interstellar Cloud Cores. In *Low Temperatures and Cold Molecules*, pages 1–54. Imperial College Press, September 2008.

[14] Brett A. McGuire. 2021 Census of Interstellar, Circumstellar, Extragalactic, Protoplanetary Disk, and Exoplanetary Molecules. *The Astrophysical Journal Supplement Series*, 259(2):30, March 2022.

[15] molecules [CDMS classic documentation].

[16] P. Swings and L. Rosenfeld. Considerations Regarding Interstellar Molecules. *The Astrophysical Journal*, 86:483–486, November 1937.

[17] A. E. Douglas and G. Herzberg. Note on CH in Interstellar Space and in the Laboratory. *The Astrophysical Journal*, 94:381, September 1941.

[18] Nabanita Deb, Brianna R. Heazlewood, Christopher J. Rennick, and Timothy P. Softley. Laser induced rovibrational cooling of the linear polyatomic ion $C_2H_2^+$. *The Journal of Chemical Physics*, 140(16):164314, April 2014.

[19] Chloé Miossec, Lok Yiu Wu, Paul Bertier, Michal Hejduk, Jutta Toscano, and Brianna R. Heazlewood. A stand-alone magnetic guide for producing tuneable radical beams. *The Journal of Chemical Physics*, 153(10):104202, September 2020.

[20] V. Wakelam, E. Herbst, J.-C. Loison, I. W. M. Smith, V. Chandrasekaran, B. Pavone, N. G. Adams, M.-C. Bacchus-Montabonel, A. Bergeat, K. Béroff, V. M. Bierbaum, M. Chabot, A. Dalgarno, E. F. van Dishoeck, A. Faure, W. D. Geppert, D. Gerlich, D. Galli, E. Hébrard, F. Hersant, K. M. Hickson,

P. Honvault, S. J. Klippenstein, S. Le Picard, G. Nyman, P. Pernot, S. Schlemmer, F. Selsis, I. R. Sims, D. Talbi, J. Tennyson, J. Troe, R. Wester, and L. Wiesenfeld. A KINETIC DATABASE FOR ASTROCHEMISTRY (KIDA). *The Astrophysical Journal Supplement Series*, 199(1):21, March 2012.

[21] D. McElroy, C. Walsh, A. J. Markwick, M. A. Cordiner, K. Smith, and T. J. Millar. The UMIST database for astrochemistry 2012. *Astronomy & Astrophysics*, 550:A36, February 2013.

[22] Brianna R. Heazlewood. Cold ion chemistry within Coulomb crystals. *Molecular Physics*, 117(14):1934–1941, July 2019.

[23] Alexander David Gingell. *Applications of Coulomb crystals in cold chemistry*. PhD thesis, Oxford University, UK, 2010.

[24] J. Slevin and W. Stirling. Radio frequency atomic hydrogen beam source. *Review of Scientific Instruments*, 52(11):1780–1782, November 1981.

[25] Lida Ghassemzadeh, Timothy J. Peckham, Thomas Weissbach, Xiaoyan Luo, and Steven Holdcroft. Selective Formation of Hydrogen and Hydroxyl Radicals by Electron Beam Irradiation and Their Reactivity with Perfluorosulfonated Acid Ionomer. *Journal of the American Chemical Society*, 135(42):15923–15932, October 2013.

[26] Jérôme Thiebaud, Alina Aluculesei, and Christa Fittschen. Formation of HO_2 radicals from the photodissociation of H_2O_2 at 248nm. *The Journal of Chemical Physics*, 126(18):186101, May 2007.

[27] Tomislav Damjanović, Stefan Willitsch, Nicolas Vanhaecke, Henrik Haak, Gerard Meijer, Jean-Paul Cromiéres, and Dongdong Zhang. A new design for a traveling-wave Zeeman decelerator: I. Theory. *New Journal of Physics*, 23(10):105006, October 2021.

[28] Nicolas Vanhaecke, Urban Meier, Markus Andrist, Beat H. Meier, and Frédéric Merkt. Multistage Zeeman deceleration of hydrogen atoms. *Physical Review A*, 75(3):031402, March 2007.

[29] E. Narevicius, C. G. Parthey, A. Libson, M. F. Riedel, U. Even, and M. G. Raizen. Towards magnetic slowing of atoms and molecules. *New Journal of Physics*, 9(4):96, April 2007.

[30] Brianna R. Heazlewood. Quantum-State Control and Manipulation of Paramagnetic Molecules with Magnetic Fields. *Annual Review of Physical Chemistry*, 72(1):353–373, April 2021.

[31] Edvardas Narevicius, Adam Libson, Christian G. Parthey, Isaac Chavez, Julia Narevicius, Uzi Even, and Mark G. Raizen. Stopping supersonic oxygen with a series of pulsed electromagnetic coils: A molecular coilgun. *Physical Review A*, 77(5):051401, May 2008.

[32] Jutta Toscano and Merton College. *Cold state-selected radicals for the study of low temperature chemistry.* PhD thesis, University of Oxford, 2018.

[33] Jutta Toscano, Atreju Tauschinsky, Katrin Dulitz, Christopher J Rennick, Brianna R Heazlewood, and Timothy P Softley. Zeeman deceleration beyond periodic phase space stability. *New Journal of Physics*, 19(8):083016, August 2017.

[34] Katrin Dulitz, Atreju Tauschinsky, and Timothy P Softley. Zeeman deceleration of electron-impact-excited metastable helium atoms. *New Journal of Physics*, 17(3):035005, March 2015.

[35] Stefan Willitsch. Coulomb-crystallised molecular ions in traps: methods, applications, prospects. *International Reviews in Physical Chemistry*, 31(2):175–199, April 2012.

[36] Alexey Potapov, André Canosa, Elena Jiménez, and Bertrand Rowe. Uniform Supersonic Chemical Reactors: 30 Years of Astrochemical History and Future Challenges. *Angewandte Chemie International Edition*, 56(30):8618–8640, 2017.

[37] Takamasa Momose, Yang Liu, Sida Zhou, Pavle Djuricanin, and David Carty. Manipulation of translational motion of methyl radicals by pulsed magnetic fields. *Physical Chemistry Chemical Physics*, 15(6):1772–1777, January 2013.

[38] Michael Motsch, Paul Jansen, Josef A. Agner, Hansjürg Schmutz, and Frédéric Merkt. Slow and velocity-tunable beams of metastable He_2 by multistage Zeeman deceleration. *Physical Review A*, 89(4):043420, April 2014.

[39] Vikram Plomp, Zhi Gao, Theo Cremers, and Sebastiaan Y. T. van de Meerakker. Multistage Zeeman deceleration of NH X $^3\Sigma^+$ radicals. *Physical Review A*, 99(3):033417, March 2019.

[40] Vikram Plomp, Zhi Gao, Theo Cremers, Matthieu Besemer, and Sebastiaan Y. T. van de Meerakker. High-resolution imaging of molecular collisions using a Zeeman decelerator. *The Journal of Chemical Physics*, 152(9):091103, March 2020.

[41] Tomislav Damjanović, Stefan Willitsch, Nicolas Vanhaecke, Henrik Haak, Gerard Meijer, JeanPaul Cromiéres, and Dongdong Zhang. A new design for a traveling-wave Zeeman decelerator: II. Experiment. *New Journal of Physics*, 23(10):105007, November 2021.

[42] Benjamin L. Augenbraun, Alexander Frenett, Hiromitsu Sawaoka, Christian Hallas, Nathaniel B. Vilas, Abdullah Nasir, Zack D. Lasner, and John M. Doyle. Zeeman-Sisyphus Deceleration of Molecular Beams. *Physical Review Letters*, 127(26):263002, December 2021.

[43] Yair Segev, Martin Pitzer, Michael Karpov, Nitzan Akerman, Julia Narevicius, and Edvardas Narevicius. Collisions between cold molecules in a superconducting magnetic trap. *Nature*, 572(7768):189–193, August 2019.

[44] Michael Karpov, Martin Pitzer, Yair Segev, Julia Narevicius, and Edvardas Narevicius. Low-energy collisions between carbon atoms and oxygen molecules in a magnetic trap. *New Journal of Physics*, 22(10):103055, October 2020.

[45] Pascal Weckesser, Fabian Thielemann, Dariusz Wiater, Agata Wojciechowska, Leon Karpa, Krzysztof Jachymski, Michał Tomza, Thomas Walker, and Tobias Schaetz. Observation of Feshbach resonances between a single ion and ultracold atoms. *Nature*, 600(7889):429–433, December 2021.

[46] Elia Perego, Lucia Duca, and Carlo Sias. Electro-Optical Ion Trap for Experiments with Atom-Ion Quantum Hybrid Systems. *Applied Sciences*, 10(7):2222, January 2020.

[47] Felix H.J. Hall, Pascal Eberle, Gregor Hegi, Maurice Raoult, Mireille Aymar, Olivier Dulieu, and Stefan Willitsch. Ion-neutral chemistry at ultralow en-

ergies: dynamics of reactive collisions between laser-cooled Ca^+ ions and Rb atoms in an ion-atom hybrid trap. *Molecular Physics*, 111(14-15):2020–2032, August 2013.

[48] Leon Karpa. Interactions of Ions and Ultracold Neutral Atom Ensembles in Composite Optical Dipole Traps: Developments and Perspectives. *Atoms*, 9(3):39, September 2021.

[49] G. Dupeyrat, J. B. Marquette, and B. R. Rowe. Design and testing of axisymmetric nozzles for ion-molecule reaction studies. *The Physics of Fluids*, 28(5):1273–1279, May 1985.

[50] B. R. Rowe, G. Dupeyrat, J. B. Marquette, and P. Gaucherel. Study of the reactions $N_2^+ + 2\,N_2 \rightarrow N_4^+ + N_2$ and $O_2^+ + 2\,O_2 \rightarrow O_4^+ + O_2$ from 20 to 160 K by the CRESU technique. *The Journal of Chemical Physics*, 80(10):4915–4921, May 1984.

[51] Ilsa R. Cooke, Divita Gupta, Joseph P. Messinger, and Ian R. Sims. Benzonitrile as a Proxy for Benzene in the Cold ISM: Low-temperature Rate Coefficients for $CN + C_6H_6$. *The Astrophysical Journal Letters*, 891(2):L41, March 2020.

[52] A. Tsikritea, K. Park, P. Bertier, J. Loreau, T. P. Softley, and B. R. Heazlewood. Inverse kinetic isotope effects in the charge transfer reactions of ammonia with rare gas ions. *Chemical Science*, 12(29):10005–10013, July 2021.

[53] Xin Tong, Tibor Nagy, Juvenal Yosa Reyes, Matthias Germann, Markus Meuwly, and Stefan Willitsch. State-selected ion–molecule reactions with

Coulomb-crystallized molecular ions in traps. *Chemical Physics Letters*, 547:1–8, September 2012.

[54] Jutta Toscano, H. J. Lewandowski, and Brianna R. Heazlewood. Cold and controlled chemical reaction dynamics. *Physical Chemistry Chemical Physics*, 22(17):9180–9194, May 2020.

[55] Michael Hawley and Mark A. Smith. The gas phase reaction of $C_2H_2^+$ with H_2 below 3 K: The reopening of the bimolecular $C_2H_3^+$ channel at low energy. *The Journal of Chemical Physics*, 96(2):1121–1127, January 1992.

[56] Xin Tong, Dieter Wild, and Stefan Willitsch. Collisional and radiative effects in the state-selective preparation of translationally cold molecular ions in ion traps. *Physical Review A*, 83(2):023415, February 2011.

[57] Xin Tong, Alexander H. Winney, and Stefan Willitsch. Sympathetic Cooling of Molecular Ions in Selected Rotational and Vibrational States Produced by Threshold Photoionization. *Physical Review Letters*, 105(14):143001, September 2010.

[58] Amy Gardner, Timothy Softley, and Matthias Keller. Multi-photon ionisation spectroscopy for rotational state preparation of N_2^+. *Scientific Reports*, 9(1):506, January 2019.

[59] Wade G. Rellergert, Scott T. Sullivan, Steven J. Schowalter, Svetlana Kotochigova, Kuang Chen, and Eric R. Hudson. Evidence for sympathetic vibrational cooling of translationally cold molecules. *Nature*, 495(7442):490–494, 2013.

[60] T. Schneider, B. Roth, H. Duncker, I. Ernsting, and S. Schiller. All-optical preparation of molecular ions in the rovibrational ground state. *Nature Physics*, 6(4):275–278, April 2010.

[61] K Højbjerre, A K Hansen, P S Skyt, P F Staanum, and M Drewsen. Rotational state resolved photodissociation spectroscopy of translationally and vibrationally cold MgH^+ ions: toward rotational cooling of molecular ions. *New Journal of Physics*, 11(5):055026, May 2009.

[62] Peter F. Staanum, Klaus Højbjerre, Peter S. Skyt, Anders K. Hansen, and Michael Drewsen. Rotational laser cooling of vibrationally and translationally cold molecular ions. *Nature Physics*, 6(4):271–274, April 2010.

[63] Michael Niedermayr, Kirill Lakhmanskiy, Muir Kumph, Stefan Partel, Jonannes Edlinger, Michael Brownnutt, and Rainer Blatt. Cryogenic surface ion trap based on intrinsic silicon. *New Journal of Physics*, 16(11):113068, November 2014.

[64] Jaroslaw Labaziewicz, Yufei Ge, Paul Antohi, David Leibrandt, Kenneth R. Brown, and Isaac L. Chuang. Suppression of Heating Rates in Cryogenic Surface-Electrode Ion Traps. *Physical Review Letters*, 100(1):013001, January 2008.

[65] P. B. Antohi, D. Schuster, G. M. Akselrod, J. Labaziewicz, Y. Ge, Z. Lin, W. S. Bakr, and I. L. Chuang. Cryogenic ion trapping systems with surface-electrode traps. *Review of Scientific Instruments*, 80(1):013103, January 2009.

[66] Shannon X. Wang, Yufei Ge, Jaroslaw Labaziewicz, Eric Dauler, Karl Berggren, and Isaac L. Chuang. Superconducting microfabricated ion traps. *Applied Physics Letters*, 97(24):244102, December 2010.

[67] T. Dubielzig, S. Halama, H. Hahn, G. Zarantonello, M. Niemann, A. Bautista-Salvador, and C. Ospelkaus. Ultra-low-vibration closed-cycle cryogenic surface-electrode ion trap apparatus. *Review of Scientific Instruments*, 92(4):043201, April 2021.

[68] Da An, Clemens Matthiesen, Ahmed Abdelrahman, Maya Berlin-Udi, Dylan Gorman, Sönke Möller, Erik Urban, and Hartmut Häffner. Surface trap with dc-tunable ion-electrode distance. *Review of Scientific Instruments*, 89(9):093102, September 2018.

[69] I. M. Georgescu and S. Willitsch. Theoretical characterization of laser- and sympathetically-cooled ions in surface-electrode ion traps. *Phys. Chem. Chem. Phys.*, 13:18852–18858, 2011.

[70] Dieter Gerlich. Ion-neutral collisions in a 22-pole trap at very low energies. *Physica Scripta*, 1995:256, January 2007.

[71] Michal Hejduk. *Reactions of Hydrogen Molecules with Ions and Recombination of H_3^+ Ions with Electrons at Cryogenic Temperatures*. PhD thesis, Charles University in Prague, 2013.

[72] Dieter Gerlich, Gheorge Borodi, Alfonz Luca, Cesar Mogo, and Mark A. Smith. Reactions between Cold CHx^+ and Slow H and H_2. *Zeitschrift für Physikalische Chemie*, 225(5):475–492, May 2011.

[73] Serhiy Rednyk, Štěpán Roučka, Petr Dohnal, Michal Hejduk, Juraj Glosík, and Radek Plašil. Reaction of carbon dication C_2^+ with O_2 , N_2 , CO, and HD at low temperatures: Experimental study using a 22-pole ion trap. *Physical Review A*, 104(6):062803, December 2021.

[74] Chloé Miossec, Michal Hejduk, Rahul Pandey, Neville J. A. Coughlan, and Brianna R. Heazlewood. Design and characterization of a cryogenic linear Paul ion trap for ion–neutral reaction studies. *Review of Scientific Instruments*, 93(3):033201, March 2022.

[75] R. J. Rafac, B. C. Young, J. A. Beall, W. M. Itano, D. J. Wineland, and J. C. Bergquist. Sub-dekahertz Ultraviolet Spectroscopy of $^{199}Hg^+$. *Physical Review Letters*, 85(12):2462–2465, September 2000.

[76] M. Schwarz, O. O. Versolato, A. Windberger, F. R. Brunner, T. Ballance, S. N. Eberle, J. Ullrich, P. O. Schmidt, A. K. Hansen, A. D. Gingell, M. Drewsen, and J. R. Crespo López-Urrutia. Cryogenic linear Paul trap for cold highly charged ion experiments. *Review of Scientific Instruments*, 83(8):083115, August 2012.

[77] A. Windberger, M. Schwarz, O. O. Versolato, T. Baumann, H. Bekker, L. Schmöger, A. K. Hansen, A. D. Gingell, L. Klosowski, S. Kristensen, P. O. Schmidt, J. Ullrich, M. Drewsen, and J. R. Crespo López-Urrutia. Coulomb crystals in a cryogenic Paul trap for sympathetic cooling of molecular ions and highly charged ions. *AIP Conference Proceedings*, 1521(1):250, March 2013.

[78] O. O. Versolato, M. Schwarz, A. K. Hansen, A. D. Gingell, A. Windberger, Ł. Kłosowski, J. Ullrich, F. Jensen, J. R. Crespo López-Urrutia, and M. Drewsen.

Decay Rate Measurement of the First Vibrationally Excited State of MgH^+ in a Cryogenic Paul Trap. *Physical Review Letters*, 111(5):053002, July 2013.

[79] A. K. Hansen, O. O. Versolato, Ł Kłosowski, S. B. Kristensen, A. Gingell, M. Schwarz, A. Windberger, J. Ullrich, J. R. Crespo López-Urrutia, and M. Drewsen. Efficient rotational cooling of Coulomb-crystallized molecular ions by a helium buffer gas. *Nature*, 508(7494):76–79, April 2014.

[80] T. Leopold, S. A. King, P. Micke, A. Bautista-Salvador, J. C. Heip, C. Ospelkaus, J. R. Crespo López-Urrutia, and P. O. Schmidt. A cryogenic radio-frequency ion trap for quantum logic spectroscopy of highly charged ions. *Review of Scientific Instruments*, 90(7):073201, July 2019.

[81] J. Stark, C. Warnecke, S. Bogen, S. Chen, E. A. Dijck, S. Kühn, M. K. Rosner, A. Graf, J. Nauta, J.-H. Oelmann, L. Schmöger, M. Schwarz, D. Liebert, L. J. Spieß, S. A. King, T. Leopold, P. Micke, P. O. Schmidt, T. Pfeifer, and J. R. Crespo López-Urrutia. An ultralow-noise superconducting radio-frequency ion trap for frequency metrology with highly charged ions. *Review of Scientific Instruments*, 92(8):083203, August 2021.

[82] R C Thompson, S Donnellan, D R Crick, and D M Segal. Applications of laser cooled ions in a Penning trap. *Journal of Physics B: Atomic, Molecular and Optical Physics*, 42(15):154003, August 2009.

[83] T. B. Mitchell, J. J. Bollinger, D. H. E. Dubin, X. Huang, W. M. Itano, and R. H. Baughman. Direct observations of structural phase transitions in planar crystallized ion plasmas. *Science (New York, N.Y.)*, 282(5392):1290–1293, November 1998.

[84] Wolfgang Paul. Electromagnetic traps for charged and neutral particles. *Reviews of Modern Physics*, 62(3):531–540, July 1990.

[85] Güther Werth, Viorica N. Gheorghe, and Fouad G. Major. Summary of Trap Properties. In Günther Werth, Viorica N. Gheorghe, and Fouad G. Major, editors, *Charged Particle Traps II: Applications*, Springer Series on Atomic, Optical, and Plasma Physics, pages 3–34. Springer, Berlin, Heidelberg, 2009.

[86] Noriaki Horiuchi. Surface ion trap. *Nature Photonics*, 16(1):13–13, January 2022.

[87] Martina Knoop. Radiofrequency traps. In *Trapped Charged Particles*, Advanced Textbooks in Physics, pages 35–53. World Scientific (Europe), September 2015.

[88] Roland Wester. Radiofrequency multipole traps: tools for spectroscopy and dynamics of cold molecular ions. *Journal of Physics B: Atomic, Molecular and Optical Physics*, 42(15):154001, August 2009.

[89] D. Gerlich and G. Borodi. Buffer gas cooling of polyatomic ions in rf multielectrode traps. *Faraday Discussions*, 142:57–72; discussion 93–111, 2009.

[90] J. Mikosch, R. Otto, S. Trippel, C. Eichhorn, M. Weidemüller, and R. Wester. Inverse temperature dependent lifetimes of transient $S_N{}^2$ ion-dipole complexes. *The Journal of Physical Chemistry. A*, 112(42):10448–10452, October 2008.

[91] J. Deiglmayr, A. Göritz, T. Best, M. Weidemüller, and R. Wester. Reactive collisions of trapped anions with ultracold atoms. *Physical Review A*, 86(4):043438, October 2012.

[92] Katharina Geistlinger, Moritz Fischer, Steffen Spieler, Lena Remmers, Felix Duensing, Franziska Dahlmann, Eric Endres, and Roland Wester. A sub-4 Kelvin radio frequency linear multipole wire trap. *Review of Scientific Instruments*, 92(2):023204, February 2021.

[93] Nabanita Deb. *Towards Cold State-Selected Ion-Molecule Reactions*. PhD thesis, University of Oxford, 2014.

[94] Émile Mathieu. Mémoire sur le mouvement vibratoire d'une membrane de forme elliptique. *Journal de Mathématiques Pures et Appliquées*, 13:137–203, 1868.

[95] M. Drewsen and A. Brøner. Harmonic linear Paul trap: Stability diagram and effective potentials. *Physical Review A*, 62(4):045401, September 2000.

[96] Dieter Gerlich. Inhomogeneous RF Fields: A Versatile Tool for the Study of Processes with Slow Ions. In *Advances in Chemical Physics*, pages 1–176. John Wiley & Sons, Ltd, 1992.

[97] Andriana Tsikritea. *Charge transfer reactions between rare gas ions and polar molecules*. PhD thesis, University of Oxford, 2021.

[98] G. Ritter, S.-M. Bae, and U. Eichmann. All-diode-laser cooling of single Ca^+ ions. *Applied Physics B*, 66(5):609–612, May 1998.

[99] Stefan Willitsch, Martin T. Bell, Alexander D. Gingell, and Timothy P. Softley. Chemical applications of laser- and sympathetically-cooled ions in ion traps. *Physical Chemistry Chemical Physics*, 10(48):7200–7210, 2008.

[100] Michael Drewsen. Ion coulomb crystals and their applications. In *Trapped Charged Particles*, Advanced Textbooks in Physics, pages 299–319. World Scientific (Europe), September 2015.

[101] Andriana Tsikritea, Jake A. Diprose, Jérôme Loreau, and Brianna R. Heazlewood. Charge Transfer Reactions between Water Isotopologues and Kr^+ ions. *ACS Physical Chemistry Au*, 2(3):199–205, May 2022.

[102] L. S. Petralia, A. Tsikritea, J. Loreau, T. P. Softley, and B. R. Heazlewood. Strong inverse kinetic isotope effect observed in ammonia charge exchange reactions. *Nature Communications*, 11(1):173, January 2020.

[103] Olivia A. Krohn, Katherine J. Catani, James Greenberg, Srivathsan P. Sundar, Gabriel da Silva, and Heather J. Lewandowski. Isotope-specific reactions of acetonitrile (CH_3CN) with trapped, translationally cold CCl^+. *The Journal of Chemical Physics*, 154(7):074305, February 2021.

[104] J. R. Heim. A low heat leak temperature stabilized column type support. *Cryogenics*, 12(6):444–450, December 1972.

[105] K. A. E. Meyer, L. L. Pollum, L. S. Petralia, A. Tauschinsky, C. J. Rennick, T. P. Softley, and B. R. Heazlewood. Ejection of Coulomb Crystals from a Linear Paul Ion Trap for Ion–Molecule Reaction Studies. *The Journal of Physical Chemistry A*, 119(50):12449–12456, December 2015.

[106] Metal Vapour Sources | » AlfaVakuo e.U.

[107] Michal Hejduk and Brianna R. Heazlewood. Off-axis parabolic mirror relay microscope for experiments with ultra-cold matter. *Review of Scientific Instruments*, 90(12):123701, December 2019.

[108] Robert M. Malone, Steven A. Becker, Daniel H. Dolan, Richard G. Hacking, Randy J. Hickman, Morris I. Kaufman, Gerald D. Stevens, and William D. Turley. Design of a thermal imaging diagnostic using 90-degree off-axis parabolic mirrors, August 2006.

[109] A. Tsuchiya, X. Lin, H. Takayama, M. Saito, and M. Xu. Development of 1.5 W 4 K Two-Stage Pulse Tube Cryocoolers with a Remote Valve Unit, 2014.

[110] T. Tomaru, T. Suzuki, T. Haruyama, T. Shintomi, N. Sato, A. Yamamoto, Y. Ikushima, R. Li, T. Akutsu, T. Uchiyama, and S. Miyoki. Vibration-Free Pulse Tube Cryocooler System for Gravitational Wave Detectors, Part I: Vibration-Reduction Method and Measurement. In Ronald G. Ross, editor, *Cryocoolers 13*, pages 695–702, Boston, MA, 2005. Springer US.

[111] P. Micke, J. Stark, S. A. King, T. Leopold, T. Pfeifer, L. Schmöger, M. Schwarz, L. J. Spieß, P. O. Schmidt, and J. R. Crespo López-Urrutia. Closed-cycle, low-vibration 4 K cryostat for ion traps and other applications. *Review of Scientific Instruments*, 90(6):065104, June 2019.

[112] Nabanita Deb, Laura L. Pollum, Alexander D. Smith, Matthias Keller, Christopher J. Rennick, Brianna R. Heazlewood, and Timothy P. Softley. Coulomb crystal mass spectrometry in a digital ion trap. *Phys. Rev. A*, 91:033408, Mar 2015.

[113] Jutta Toscano, Christopher J. Rennick, Timothy P. Softley, and Brianna R. Heazlewood. A magnetic guide to purify radical beams. *The Journal of Chemical Physics*, 149(17):174201, November 2018.

[114] Katrin Dulitz, Michael Motsch, Nicolas Vanhaecke, and Timothy P. Softley. Getting a grip on the transverse motion in a Zeeman decelerator. *The Journal of Chemical Physics*, 140(10):104201, March 2014.

[115] K. Halbach. Design of permanent multipole magnets with oriented rare earth cobalt material. *Nuclear Instruments and Methods*, 169(1):1–10, February 1980.

[116] B. Ghaffari, J. M. Gerton, W. I. McAlexander, K. E. Strecker, D. M. Homan, and R. G. Hulet. Laser-free slow atom source. *Physical Review A*, 60(5):3878–3881, November 1999.

[117] A. Goepfert, F. Lison, R. Schütze, R. Wynands, D. Haubrich, and D. Meschede. Efficient magnetic guiding and deflection of atomic beams with moderate velocities. *Applied Physics B: Lasers and Optics*, 69(3):217–222, September 1999.

[118] Jutta Toscano, Michal Hejduk, Henry G. McGhee, and Brianna R. Heazlewood. Manipulating hydrogen atoms using permanent magnets: Characterisation of a velocity-filtering guide. *Review of Scientific Instruments*, 90(3):033201, March 2019.

[119] Ardita Kilaj, Jia Wang, Patrik Straňák, Max Schwilk, Uxía Rivero, Lei Xu, O. Anatole von Lilienfeld, Jochen Küpper, and Stefan Willitsch. Conformer-

specific polar cycloaddition of dibromobutadiene with trapped propene ions. *Nature Communications*, 12(1):6047, October 2021.

[120] David C. Knauth, B-G Andersson, Stephan R. McCandliss, and H. Warren Moos. The interstellar N2 abundance towards HD 124314 from far-ultraviolet observations. *Nature*, 429(6992):636–638, June 2004.

[121] M. Schwarzer, A. Hansel, W. Freysinger, N. Oberhofer, W. Lindinger, and E. E. Ferguson. Thermal energy reactions of N_2^+ (ν=1) with SF_6, H_2, D_2, H, and D. *The Journal of Chemical Physics*, 95(10):7344–7347, November 1991.

[122] Vincent G. Anicich. Evaluated Bimolecular Ion-Molecule Gas Phase Kinetics of Positive Ions for Use in Modeling Planetary Atmospheres, Cometary Comae, and Interstellar Clouds. *Journal of Physical and Chemical Reference Data*, 22(6):1469–1569, November 1993.

[123] Z. Karpas, V. Anicich, and W. T. Huntress, Jr. An ion cyclotron resonance study of reactions of ions with hydrogen atoms. *The Journal of Chemical Physics*, 70(6):2877–2881, July 2008.

[124] P. Tosi, S. Iannotta, D. Bassi, H. Villinger, W. Dobler, and W. Lindinger. The reaction of CO_2^+ with atomic hydrogen. *The Journal of Chemical Physics*, 80(5):1905–1906, March 1984.

[125] F. C. Fehsenfeld and E. E. Ferguson. Rate constants for the reactions of CO_2^+ + H and H^+ + CO_2. *Journal of Geophysical Research (1896-1977)*, 76(34):8453–8454, 1971. _eprint: https://onlinelibrary.wiley.com/doi/pdf/10.1029/JA076i034p08453.

[126] Graham B. Scott, David A. Fairley, Colin G. Freeman, Murray J. McEwan, Patrik Spanel, and David Smith. Gas phase reactions of some positive ions with atomic and molecular hydrogen at 300 K. *The Journal of Chemical Physics*, 106(10):3982–3987, March 1997.

[127] G. Borodi, A. Luca, and D. Gerlich. Reactions of CO_2^+ with H, H_2 and deuterated analogues. *International Journal of Mass Spectrometry*, 280(1):218–225, February 2009.